FAR EASTERN FEDERAL UNIVERSITY

As a manuscript

Balanov Mikhail Ivanovich

STRUCTURAL, ELECTRONIC AND OPTICAL PROPERTIES OF HYBRID COMPOUNDS BASED ON LEAD HALIDES AND A HOMOLOGOUS SERIES OF DIAMINES OF THE FORM $[H_3N\text{-}(CH_2)_n\text{-}NH_3]PbX_4$ (n=4-8, X=Cl, Br, I)

Scientific Specialty 1.3.8. Condensed Matter Physics

Thesis for the degree candidate of Physical and Mathematical Sciences

Translation from Russian

Scientific supervisor:
Doctor of Physical and Mathematical Sciences
Shtarev Dmitry Sergeevich

Vladivostok
2024

TABLE OF CONTENTS

INTRODUCTION 4

Chapter 1. OPTICAL, STRUCTURAL AND ELECTRONIC PROPERTIES OF HYBRID PEROVSKITES BASED ON ALKANEDIAMINES: LITERARY REVIEW 11

1.1 Completely inorganic perovskites 11

1.2 Hybrid perovskites 12

1.3 Low-dimensional hybrid perovskites of the diamine series 12

Conclusions on the 1 chapter 23

Chapter 2. MATERIALS AND METHODS 24

2.1 Materials 24

2.2 Synthesis methods 25

2.3 Measurement methods 28

2.4 Methods of numerical calculations and computer modeling 30

Conclusions on the 2 chapter 30

Chapter 3. EXPERIMENTAL RESULTS 31

3.1 Crystal structure of hybrid compounds based on lead halides and homologous series of limiting diamines of the form $[H_3N\text{-}(CH_2)_n\text{-}NH_3]PbX_4$ (n=4-8, X=Cl, Br, I) 31

3.1.1 Powder XRD 31

3.1.2 Single crystal XRD 40

3.1.3 Analysis of the dependence of the structure of hybrid compounds based on lead halides and the homologous series of limiting diamines of the form $[H_3N\text{-}(CH_2)_n\text{-}NH_3]PbX_4$ on the length of the organic chain and the halogen 46

3.2 Quantum chemical calculations of hybrid compounds based on lead halides and homologous series of diamines of the form $[H_3N\text{-}(CH_2)_n\text{-}NH_3]PbX_4$ (n=4-8, X=Cl, Br, I) 56

3.3 Optical properties of hybrid compounds based on lead halides and a homologous series of diamines of the form $[H_3N\text{-}(CH_2)_n\text{-}NH_3]PbX_4$ (n=4-8, X=Cl, Br, I) 62

3.3.1 Diffuse reflection spectroscopy 62

3.3.2 Luminescent properties 67

3.4 X-ray photoelectron spectroscopy of hybrid compounds based on lead halides and a homologous series of limiting diamines of the form $[H_3N-(CH_2)_n-NH_3]PbX_4$ (n=4-8, X=Cl, Br, I) 77

3.4.1 Investigation of the chemical environment of the main elements..... 77

3.4.2 Determination of the output operation and the potential of the valence band ceiling..... 79

3.5 Electronic band structures of hybrid compounds based on lead halides and a homologous series of diamines of the form $[H_3N-(CH_2)_n-NH_3]PbX_4$ (n=4-8, X=Cl, Br, I) 82

3.6 Phase transitions in hybrid compounds based on lead halides and a homologous series of diamines of the form $[H_3N-(CH_2)_n-NH_3]PbX_4$ (n=4-8, X=Cl, Br, I) 83

3.6.1 Differential scanning calorimetry..... 83

3.6.2 Investigation of phase transitions by X-ray diffraction methods..... 89

3.6.3 Investigation of phase transitions by luminescent methods..... 96

Conclusions on the 3 chapter 99

CONCLUSION..... 102

ACKNOWLEDGMENTS 105

REFERENCES..... 106

INTRODUCTION

Relevance of the work

In general, the electronic structure, optical properties, photoexcitation processes, charge/energy transfer and relaxation of excited states in solids are determined by their chemical composition and type of crystal structure. A distinctive feature of hybrid organic-inorganic materials is the presence of two subsystems, organic and inorganic, which form the crystal structure of such materials and may or may not interact with each other in terms of the processes of photoexcitation and relaxation of their electronic states. In case of realization of interaction between electronic states of organic and inorganic subsystems, such interaction can have both local character, affecting only the near-order structure of materials, and delocalized character, determined by the presence of the long-range order in hybrid materials. The nature of interaction determines the efficiency of photoexcitation processes, the type of excited states, the possibility of excitation transfer and the efficiency of relaxation of various excited states, including radiative relaxation, i.e., luminescence of hybrid materials. Thus, a targeted change in the structure of hybrid materials, their near and far orders, will allow to change the nature of the processes of photoexcitation and excitation relaxation, thereby increasing the efficiency of the functional characteristics of hybrid materials.

A distinctive feature of low-dimensional halide hybrid crystals is the presence of organic cations with amine groups of large size in the composition of such compounds, thus violating the tolerance factor for the perovskite lattice and performing the structural role of "scissors", cutting the bonds between the structural elements of the inorganic subsystem of hybrid halide crystals - octahedrons formed by Pb2+ cation and halide anions, which makes it possible to obtain quasi-low-dimensional inorganic systems of 2D, 1D and 0D types, depending on the structural features of the organic cation. At the same time, the use of saturated amine cations, as a rule, excludes electronic interaction between organic and inorganic subsystems of such materials

during their photoexcitation, while the use of aromatic cations creates conditions for overlapping of electronic states of π-system of organic cations with electronic states of inorganic subsystem in low-dimensional hybrid halide perovskites. Changing the type of organic cation can lead to changes in the electronic interactions in both the near- and far-order structure of such materials, which, by definition, can significantly alter the optical and luminescence characteristics of hybrid crystals.

Another important distinguishing feature of low-dimensional hybrid materials is their structural anisotropy. Thus, in 2D structures, the layers of the inorganic component of the material are separated by layers of organic cations, which leads to a periodic change in dielectric constant, phonon states, anisotropy in charge transfer and can lead to a significant change in absorption when the polarization of the excitation light changes and different polarization of luminescence when relaxing through organic and inorganic states. This opens up the possibility of controlling excitation, charge transfer and radiative relaxation through the targeted formation of low-dimensional hybrid perovskite materials of a given structure, thus making such materials promising for practical applications in various fields of optoelectronics and photonics.

Thus, based on all the above, the following aims and objectives of the present study can be formulated.

The purpose of the dissertation is to establish the influence of the structure of an organic cation and the type of anion on the structural, electronic and optical properties of hybrid compounds based on lead halides and a homological series of limiting diamines of the type $[H_3N\text{-}(CH_2)_n\text{-}NH_3]PbX_4$ (n=4-8, X=Cl, Br, I).

In accordance with the formulated aim, there are **the following main objectives** of the research:

- to develop methods of preparation of hybrid compounds on the basis of lead halides and homologous series of diamines of the form $[H_3N\text{-}(CH_2)_n\text{-}NH_3]PbX_4$ (n=4-8, X=Cl, Br, I) in the form of polycrystals and monocrystals;
- to establish the structural, electronic and optical properties of hybrid compounds;

- to investigate the patterns of changes in the structural, electronic and optical properties of hybrid compounds depending on the size of the hydrocarbon chain of the organic cation and the type of anion in their structure.

The objects of research in this work are polycrystals and single crystals of hybrid compounds based on lead halides and a homologous series of diamines of the form $[H_3N\text{-}(CH_2)_n\text{-}NH_3]PbX_4$ (n=4-8, X=Cl, Br, I).

The scientific novelty of the work lies in the fact that:

- the structures of new hybrid crystals based on lead chloride and pentanediamine-1,5, heptanediamine-1,7, octanediamine-1,8, as well as lead bromide and pentanediamine-1,5, heptanediamine-1,7 were synthesized and described for the first time;
- for the first time, the patterns of luminescent properties of hybrid crystals based on lead halides and a homologous series of diamines of the form $[H_3N\text{-}(CH_2)_n\text{-}NH_3]PbX_4$ (n=4-8, X=Cl, Br, I) depending on their anionic and cationic composition are described and analyzed;
- phase transitions in hybrid crystals based on lead halides and a homologous series of diamines of the form $[H_3N\text{-}(CH_2)_n\text{-}NH_3]PbX_4$ (n=4-8, X=Cl, Br, I) are described for the first time.

The practical significance of the work lies in the fact that the revealed patterns between the molecular structure of the organic cation and the structure and properties of hybrid crystals obtained on their basis can be used to create new hybrid crystals with specified structural and optical properties.

Research methodology and methods

The methods of experimental and theoretical research used in this study are relevant and correspond to the world level of development of scientific thought in this field of knowledge. Thus, to establish and study the crystal structure of hybrid poly- and single crystals, the methods of Powder X-ray Diffraction (Powder XRD) and Single crystal X-ray Diffraction (Single crystal XRD) were used, respectively. The optical properties of all synthesized hybrid crystals were studied by diffuse reflection spectroscopy (DRS), as well as by Fluorescence Spectroscopy. The potential of the ceiling of the valence bands of hybrid crystals, as well as the features of the chemical environment in them, was determined using the method of X-ray photoelectron spectroscopy (XPS). The presence of phase transitions in hybrid crystals was determined by differential scanning calorimetry. Quantum chemical calculations were performed by the method of the Density functional theory.

The reliability of the results obtained

The reliability of the results is ensured by the use of modern experimental techniques and equipment, the numerous repeatability of experimental results, and the use of methods of statistical analysis of the data obtained. The results of the dissertation work do not contradict modern ideas in the field of condensed matter physics of hybrid crystals.

Approbation

The results of this work were presented at the Regional Scientific and Practical Conference of Students, Postgraduates and Young Scientists in Natural Sciences (Russia, Vladivostok, 2024).

The structure and scope of the dissertation:

The dissertation consists of an introduction, 3 chapters, a conclusion, acknowledgments and a references. The work contains 113 pages, including 10 tables and 78 figures. The references contain 60 titles.

Personal contribution

Obtaining the objects of research and the experimental part of the work was performed by the author independently at the Far Eastern Federal University. Part of the work on the characterization of the structural and optical properties of research objects was carried out by the author in the laboratory "Photoactive Nanocomposite Materials" of St Petersburg University and the Shenzhen MSU-BIT University. The author took an active part in setting research objectives, analyzing, and writing publications.

The main scientific results

1) The crystal structure of new hybrid crystals based on lead chloride and pentanediamine-1,5, heptanediamine-1,7 and octanediamine-1,8, as well as lead bromide and pentanediamine-1,5, heptanediamine-1,7 was described for the first time [50, pp. 264-265], [59]. The scientific results were obtained as a result of the author's joint work with other researchers.
2) For the first time, the manifestation of the parity effect of the carbon skeleton of an organic cation represented by saturated alkanediamines in hybrid crystals was discovered and analyzed. For chloride and bromide crystals, the parity effect is manifested as follows: an even carbon skeleton in the structure of an organic cation promotes the formation of two-dimensional hybrid crystals with layers of inorganic octahedra located on top of each other, without displacement, whereas an odd carbon skeleton promotes the formation of two-dimensional hybrid crystals with layers of inorganic octahedra offset relative to each other by half the width octahedra. For iodide crystals, the parity effect manifests itself differently: an even carbon skeleton in the structure of an organic cation contributes to the formation of two-dimensional hybrid crystals, whereas an odd carbon skeleton contributes to the formation of one-dimensional and zero-dimensional structures [59]. The scientific results were obtained personally by the author.

3) It has been established that two-dimensional hybrid crystals (all chloride and bromide, as well as iodide with an even carbon skeleton in the structure of an organic cation) are straight-band semiconductors, transitions from the valence band to the conduction band in which mainly occur at the point Γ of the Brillouin band. It is shown that iodide hybrid crystals with an odd carbon skeleton in the structure of an organic cation, forming one-dimensional structures, are non-bandgap semiconductors [50, pp. 267-268], [56, pp. 6393-6395], [59]. The scientific results were obtained as a result of the author's joint work with other researchers.
4) It is shown that during the formation of hybrid crystals based on alkanediamines, two competing processes of disordering the inorganic sublattice are observed: internal, characterized by distortion of the shape of each octahedron or displacement of lead atoms in octahedra from a central position, and external, characterized by the preservation of the relative perfection of the octahedra themselves, but manifested in the inclination of the octahedra relative to each other when they are combined into network [50, pp. 264], [56, pp. 6390], [59]. The scientific results were obtained personally by the author.
5) It is shown that all two-dimensional hybrid crystals based on lead halides and alkanediamines have luminescent properties. Typical luminescence of hybrid crystals based on lead halides and alkanediamines may include narrow-band luminescence of self-trapped excitons, broadband luminescence of defect-trapped excitons, or both of these bands, which is determined by the cationic and anionic composition of the hybrid crystal: chloride hybrid crystals are characterized by the presence of only broadband luminescence of defect-trapped excitons; bromide and iodide crystals are characterized by the presence of both luminescence bands; for bromide crystals, the ratio of luminescence intensities of self-trapped excitons and defect-trapped excitons depends on the size of the organic cation and decreases as it grows. The free excitons energy of self-trapping for bromide hybrid crystals lies in the range from 20 to 31 meV, for iodide crystals – from 11 to 31 meV [50, pp. 269-272], [59]. The scientific results were obtained personally by the author.

6) Phase transitions have been established in hybrid crystals based on lead halides and a homologous series of diamines of the form $[H_3N\text{-}(CH_2)_n\text{-}NH_3]PbX_4$ (n=4-8, X=Cl, Br, I) [56, pp. 6395], [59]. The scientific results were obtained personally by the author.

Statements put forward for defense:

1. A method for obtaining polycrystals and single crystals of hybrid crystals based on lead halides and a homologous series of diamines of the form $[H_3N\text{-}(CH_2)_n\text{-}NH_3]PbX_4$ (n=4-8, X=Cl, Br, I).
2. The manifestation of the parity effect of the carbon skeleton of an organic cation in the structure of hybrid crystals based on lead halides and a homologous series of diamines of the form $[H_3N\text{-}(CH_2)_n\text{-}NH_3]PbX_4$ (n=4-8, X=Cl, Br, I).
3. Manifestation of the parity effect of the carbon skeleton of an organic cation in luminescent properties of hybrid crystals based on lead halides and a homologous series of diamines of the form $[H_3N\text{-}(CH_2)_n\text{-}NH_3]PbX_4$ (n=4-8, X=Cl, Br, I).
4. The effect of the anion on the ratio of luminescence intensities corresponding to self-trapped excitons and defect-trapped excitons in hybrid crystals based on lead halides and a homologous series of diamines of the form $[H_3N\text{-}(CH_2)_n\text{-}NH_3]PbX_4$ (n=4-8, X=Cl, Br, I).
5. The effect of the size of an organic cation on the ratio of luminescence intensities corresponding to self-trapped excitons and defect-trapped excitons in hybrid crystals based on lead halides and a homologous series of diamines of the form $[H_3N\text{-}(CH_2)_n\text{-}NH_3]PbX_4$ (n=4-8, X=Cl, Br, I).

Chapter 1. OPTICAL, STRUCTURAL AND ELECTRONIC PROPERTIES OF HYBRID PEROVSKITES BASED ON ALKANEDIAMINES: LITERARY REVIEW

1.1 Completely inorganic perovskites

The ever-increasing demand for energy experienced by modern human society has led to intensive research in the field of electricity generation. Due to environmental problems, special attention is being paid today to environmentally friendly and renewable energy sources. Among them, solar energy, which is practically unlimited, plays a unique role. A number of materials are known that can efficiently convert sunlight into electricity. Halide perovskites are particularly promising in this regard, due to the inexpensive method of synthesis and the high efficiency of converting sunlight into electricity, reaching ~25.2 % [1]. However, now the areas of practical and promising application of such structures already go beyond energy generation and include highly efficient light-emitting laser diodes or white light diodes [2-4], lasers [5], photo [6] and X-ray detectors [7] and other areas. At the same time, significant interest in Perovskite research is not limited only to applied and implementation tasks. Perovskites demonstrate a number of physico-chemical phenomena, the understanding of which is of fundamental importance for studies of the interaction of photoactive media with electromagnetic radiation.

1.2 Hybrid perovskites

From the composition point of view, halide perovskites comprise the all-inorganic and organometal subfamilies. In addition to conventional 3D crystalline materials organometal halide perovskites are known to form low-dimensional pseudo 1D and 2D structures. From electronic structure prospective, organometal halide perovskites are similar to all-inorganic ones. That is their valence band (VB) and conduction band (CB) are formed from occupied p-orbitals of halide anions and vacant p-orbitals of metal cations, respectively. Noteworthy, CBs of some organometal halide perovskites containing unsaturated organic cyclic cations may be composed of unoccupied p-orbitals of the ring atoms [8-12]. The number of synthesized low-dimensional organometal halide perovskites is constantly growing. Despite rather limited applicability as photovoltaic materials some low-dimensional organometal halide perovskites can be used, for instance, as a source of white light.

It has been shown that the inorganic part of the structures mainly determines the charge mobility, band gap tunability and the optical and magnetic properties [13]. The organic cation determines the luminescence and the electronic properties of the material [14].

1.3 Low-dimensional hybrid perovskites of the diamine series

To successfully form 2D perovskite structure an organic cation must fulfill certain conditions. For instance, the formation of hydrogen bonds between the cation and

anion(s) is highly desirable [15]. A linear fragment in the structure of organic cation seems important as well. Properties of hybrid 2D perovskites containing organic cations which fulfill the above conditions were studied earlier [25-34].

In [12] the main object of research is "hollow" three-dimensional hybrid perovskites based on methylamine and formamidium. They are called "hollow" because part of the organic cations in them is replaced by short dications of ethylenediamine without changing the dimension of the structure. The paper investigates how the replacement of up to 44% of methylamine and formamidium with ethylenediamine affects the optical and structural properties of perovskites. Thus, the inclusion of ethylenediamine in the three-dimensional structure of perovskite is accompanied by the appearance of a large number of vacancies in it in the positions of the inorganic cation (M) and anion (X), which determines the use of the term "hollow". The obtained materials are semiconductors with a significant blue shift of the direct band gap from 1.25 (for unsubstituted perovskites) to 1.51 (for maximally substituted "hollow" structures) eV for Sn-based perovskites and from 1.53 to 2.1 eV for Pb-based perovskites. Based on calculations of density functional theory (DFT), the connection between the blue shift of the band gap width was proved and experimental trends are confirmed and suggest that the observed expansion of the band gap is associated with massive vacancies M and X, which create a less connected three-dimensional hollow structure.

Works [17,18] are devoted to the study of the stabilizing properties of two-dimensional hybrid perovskite based on lead iodide and ethylenediamine (EDAPbI4), which it exerts on completely inorganic perovskite CsPbI3. It is known that α-CsPbI3 has the most suitable band gap for use in tandem solar cells. However, it exhibits phase instability and can transition to β-CsPbI3 or even to a non-perovskite δ-phase. The authors of [17] showed that the introduction of a small amount (2.5%) of EDAPbI4 into the structure of CsPbI3 stabilizes its α-phase.At the same time, the stabilizing effect is manifested both on CsPbI3 films, which maintained phase stability at room temperature for months and at 100 °C for more than 150 hours, but also in perovskite solar cells, which showed an efficiency of 11.8%, which was (at the time of publication

of the article) a record for completely inorganic perovskite solar cells based on lead halides. Thus, the use of ethylenediamine represents a promising new strategy for improving the efficiency, stability and reliability of completely inorganic perovskite solar cells based on lead halides.

It was shown in [18] that the addition of ethylenediamine at the stage of synthesis of hybrid perovskite based on formamidium improves its photovoltaic properties and stability. Using various experimental techniques, the authors showed that EDA reacts with formamidium ions to form imidazolinium cations. It is its presence during the crystallization of hybrid perovskites that ensures the improvement of its operational characteristics.

If the studies reported in [12-18] are devoted to how the addition of ethylenediamine or hybrid perovskites based on it affects the properties of other perovskites, then in [19] the main attention is paid to the study of photoconductivity of the hybrid perovskite itself based on ethylenediamine and lead iodide. More specifically, in this paper, the authors investigated how the disorder of the organic subsystem affects the photovoltaic properties of hybrid perovskite. Control of the degree of disorder of the organic sublattice. The results of structural studies show that when ethylenediamine is used as an organic cation of hybrid perovskite, a low-dimensional perovskite is formed, the dimension of which can be defined as 0.5. Such a fractional dimension means the following: The octahedra of PbI6 have common faces and form three-octahedral segments; these segments line up in a chain along the hexagonal axis c; while the three-octahedral segments themselves are spaced relative to each other by a distance of about 8.2 Å between Pb atoms along the chain and about 8.4 Å between the chains. During thermal activation of these crystals at temperatures up to 150 0C, the authors of the study observed an increase in the degree of disorder of the organic subsystem, while the 0.5D structure of the inorganic subsystem did not change. At the same time, the authors observed a significant – up to 40% - increase in the photoconductivity of hybrid perovskite samples in high-temperature form.

The work [20] is to some extent a development of previous work. It also asks how modification of the EDAPbI4 structure affects its optical and structural properties. At

the same time, if in [19] the structure of perovskite was modified by temperature treatment and its transfer to a high-temperature form, then in [20] the modification was achieved by introducing chlorine ions into its structure. When chlorine ions are introduced into the perovskite structure (hereafter we will designate it as $[EDAPbI_4]Cl_2$) , its dimension radically changes, leading to the formation of a classical 2D structure: octahedra $[PbI_6]$ touching faces with each other form planes separated by a complex organic cation consisting of ethylenediamine and two chlorine ions.

It is interesting and important to consider the explanation given by the authors of the study [20] for the observed phenomenon of such a change in dimension with the introduction of chlorine ions. In the classical two-dimensional hybrid perovskite, in which the organic cation is represented by diamine, the layers of the inorganic subsystem are separated by layers of an organic cation having a specific orientation. The molecules of the organic cation are oriented by their amine groups along the axis so that the resulting hydrogen bonds N-H···Hal bind adjacent layers $[PbHal_6]$. In the case of ethylenediamine, such a molecule turns out to be too short to perform the described functions. As a result, not a two-dimensional hybrid perovskite is formed, but a structure of a lower dimension, as shown in [19].

When chlorine ions are introduced into the structure, the situation changes. Now, between the two layers of inorganic octahedra there is a structure consisting of two layers of organic cation separated by a layer of chlorine ions. In such a structure, one amine group of ethylenediamine forms hydrogen bonds of N-H···Hal with octahedra $[PbHal_6]$, and the second is the hydrogen bonds of N-H···Cl with additionally introduced chlorine ions. Due to this more complex organization, the formation of a classical two-dimensional hybrid perovskite is achieved using sufficiently short ethylenediamine molecules.

The optical properties of hybrid perovskites studied in [20] also strongly depend on their dimension. If one-dimensional perovskite $EDAPbI_4$ demonstrates a band gap of 2.72 eV, then the band gap of two-dimensional $[EDAPbI_4]Cl_2$ is significantly reduced and amounts to 2.3 eV.

In [21] the stability of hybrid perovskites based on 1,3-propanediamine (hereinafter $PDAPbI_4$), its optical properties, as well as the efficiency of solar panels based on it are investigated. It is shown that such perovskites can effectively absorb radiation with a wavelength up to 950 nm, from which the width of their band gap was determined as 1.31 eV. At the same time, the optical properties remain practically unchanged when storing samples for 3 months at a humidity of 30%. The efficiency of solar panels based on $PDAPbI_4$ turned out to be quite low and amounted to 0.141%, which the authors attribute to the engineering imperfection of the battery they designed.

Work [22] is devoted to the study of the structural, temperature and electronic properties of various hybrid perovskites based on lead halides, in which 2-methylpentane-1,5-diamine ($2meptH_2$) and 1,3-diaminopropane (pnH_2) are represented as an organic cation. It was found that, depending on the type of organic cation and the ratio of components, crystals of three different types are formed: one-dimensional $(2meptH_2)[Pb_{1.5}I_5]$, ribbon-shaped (1.5D) $(pnH_2)_2[Pb_{1.5}Br_7] \cdot H_2O$ and two-dimensional perovskite-like structures $(pnH_2)[PbCl_4]$ и $(2meptH_2)[PbX_4]$ (X = Cl, Br). Thus, by changing the ratio between organic and inorganic components, it is possible to control the dimension of hybrid perovskites.

In [23] the question of how the structure of an asymmetric organic cation affects the structural, electronic and optoelectronic properties of hybrid perovskites with a Dion-Jacobsen structure is theoretically studied. 1,3-diaminopropane (PDA), N-methylpropane-1,3-diamine (N-MPDA) and 3-(dimethylamino)-1-propylamonium (DMPD) were studied as organic cations, the structure of which is shown in Figure 1.

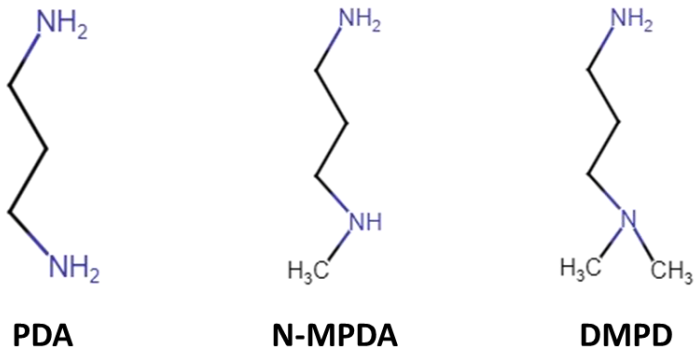

Figure 1. Organic cations: 1,3-diaminopropane (PDA), N-methylpropane-1,3-diamine (N-MODE) and 3-(dimethylamino)-1-propylammonium (DMPD).

The effect of the asymmetry of the organic ligand on perovskite is mainly manifested in changes in the Pb–I bond lengths in the PbI_6 octahedra and the Pb–I–Pb valence angle between the octahedra. As the asymmetry of the ligand increases, the distortion of the octahedra gradually increases. The paper suggests that $DMPDPbI_4$ should have good stability, have a lower energy of formation and therefore be easier to synthesize compared to perovskites with a symmetrical ligand. In addition, perovskites with asymmetric organic ligands have better absorption in the visible region than perovskite with a symmetrical ligand.

In [24] the effect of the addition of 1,3-diaminopropane to MAPI on the stability and photovoltaic properties of such a hybrid perovskite with a mixed composition of organic cations is investigated. It is shown that with such addition of diamine, the formation of a perovskite with a dimension of 2.5D occurs: the three-dimensional MAPI structure is separated by separate layers of diamine. At the same time, the use of such a short co-ligand as 1,3-diaminopropane facilitates the transport of electrons through it from one MAPI region to another. As a result, this approach can increase both the stability of hybrid perovskites and the efficiency of photovoltaic conversion for solar panels made on their basis.

The effect of organic cation length on the optical properties of low-dimensional perovskites was studied previously [25]. The study focused on perovskites with the cations $[(CH_3)_2NH(CH_2)_nNH_3]^{2+}$ (n=2-4) depicted in Figure 2. The 2D perovskites can be seen as 3D structures whose inorganic lattice is sliced along various crystallographic planes. Thus, they are distinguished as either (100)-oriented, (110)-oriented, or (111)-oriented. Depending on a particular location of corrugation within the perovskite layers these structures can be defined as 2×2, 3×3, 4×4, etc. If the size of organic cation is small and comparable to the size of inorganic octahedra then a corrugated (110)-oriented 2D perovskite is going to be formed instead of a layered (100)-oriented structure. In the case of 2-(dimethylamino)-1-ethylamine a corrugated 3x3 (110)-oriented perovskite was synthesized. Lengthier organic cations give rise to low-dimensional 2D perovskites whose layers consist of the corner-sharing $PbBr_6$ octahedra located along the bc cystallographic plane. It has been reported earlier that the

perovskite bandgaps decrease as the angles Pb-X-Pb increase [26, 27]. For instance, $(DMAPA)PbBr_4$ possessing an average angle Pb-Br-Pb of 163.9° features bandgap of 2.88 eV, while $(DMABA)PbBr_4$ with an average angle Pb-Br-Pb of 168.6° shows bandgap of 2.85 eV [25]. All the three perovskites are luminescent in a wide spectral range that is due to self-trapped excitons. The width of the luminescence spectra is linearly dependent on a degree of the $PbBr_6$ octahedra distortion.

Low-dimensional perovskite design strategies outlined in [25], were successfully employed for the synthesis of the luminescent 2D hybrids containing 5-methyl-1,5-diaminopentate cation [28]. The studied materials can be used to manufacture white light-emitting diodes.

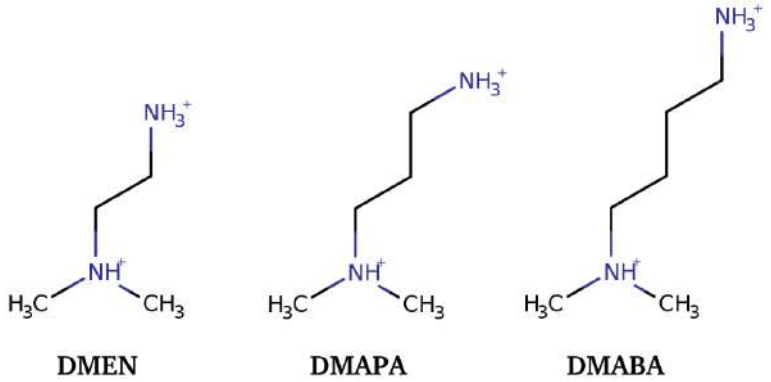

Figure 2. Organic cations: 2-(Dimethylamino)-1-ethylamine (DMEN), 3-(Dimethylamino)-1-propylamine (DMAPA), 4-(Dimethylamino)-1-butylamine (DMABA).

Crystal structures of manganese chloride-based perovskites with 1,5-diaminopentane and 1,6-diaminohexane cations were investigated in [30]. According to the study, the diaminohexane chains possess all-trans conformation whereas the diaminopentanes occurs in mixed cis/trans conformations.

The phenomena of reverse thermochromism and ferromagnetism as well as the temperature-dependent electric conductance were studied in the 2D hybrid hexamethylenediamine copper chloride perovskite [31]. The performed structural analysis revealed that the organic cations are oriented such as to form strong hydrogen bonds with chlorines of the $CuCl_6$ octahedra. The authors showed that the presence of the hydrogen bonds reduces effective charges of the chlorines thereby diminishing the inter-octahedra repulsion. The latter leads to an overall structure stabilization and

affects the orientation and conformation of the organic cations. However, details of the organic cation conformation were not reported. Optical properties of perovskites were studied by analyzing transmission spectra of their thin films. The transmission spectra were transformed into absorption spectra which demonstrated peaks at 313 nm and 385 nm. According to the authors, they are due to the ligand-to-metal charge transfer. Optical bandgap determined using the Tauc method amounted to 2.78 eV.

Structural, optical, and electronic properties of $(NH_3C_3H_6NH_3)CuBr_4$ featuring rather short carbon chain – 1,3-diaminopropane – was studied in [32]. Optical bandgap determined by the authors utilizing the Tauc method was equal to 1.71 eV. In contrast to other reports, in this study the authors used XPS technique in order to estimate the potential of a valence band top. Additionally, the feasibility of perovskite practical applications was assessed by demonstrating its superior temperature, humidity, and UV irradiation resistance. Besides, the Seebeck coefficient of 13.8 μV/K and power factor of 1.70 $\mu W/mK^2$ measured at room temperature make this perovskite a potential n-type thermoelectric material.

A large set of hybrid 2D perovskites $[NH_3\text{-}(CH_2)_n\text{-}NH_3]MX_4$, (M=Cd, Mn, Pb, Cu, Pd, and X=Cl, Br) with n varying in the range (n=1-12) was investigated in [33]. Among other issues the work focuses on conformational changes in the organic cations and the corresponding phase transitions. The authors used several experimental techniques including single crystal and powder XRD, differential scanning calorimetry, and IR spectroscopy. For instance, it was showed that diaminobutane cation may occur in different molecular conformations (ttt, ttg, gtg'), while diaminohexanes (M=Pb, Pd) coexist in two different molecular conformations. Unfortunately, the authors have focused only on the structure of the perovskites elucidating neither their electronic nor optical properties.

The structure and optical properties of low-dimenstional hybrid diaminohexane-based lead halogenides were studied in [34]. Therein, only the bromide and iodide crystals were sufficiently large in size. Since the bromide quality was rather poor the only data that we found reliable is that of the iodide. The conducted XRD studies on the iodide showed that it is in fact a 2D material whose PbI6 octahedra are separated

by diaminohexane layers. Notably, within its structure diaminohexane cations occur in «extended form» i.e. they bond neighboring inorganic layers through hydrogen bonds between -NH_3 groups and iodide anions. The second part of the work deals with the perovskite optical properties. Optical absorption spectra of the perovskite thin films reveal excitonic absorption peaks at 482 nm (2.57 eV), 390 nm (3.18 eV), and 332 nm (3.73 eV) for the iodide, bromide, and chloride, respectively. Knowing the perovskite bandgaps (I: Eg=~2.726 eV; Br: Eg=~3.346 eV; Cl: 3.940 eV) and assuming that they are energetically close to the excitonic absorption bands the exciton binding energies Eb can be estimated as Eb=Eg-E(exc. peak) resulting in Eb=~153.3 meV, Eb=~166.4 meV, and Eb=~205.4 meV for the iodide, bromide, and chloride, respectively. Thus, there is a clear correlation between Eg and the type of the perovskite anion.

In [35] the structures of several low-dimensional hybrid diamine perovskites with the general formula $[H_3N\text{-}(CH_2)_n\text{-}NH_3]PbX_4$ are studied, namely: bromide perovskites (X=Br) with 2, 4 and 10 carbon atoms (n=2, 4, 10), as well as iodide perovskites (X=I) with n=4, 7, 8, 12. It was found that even alkyl chains with ammonium groups at both ends (n=4, 8, 10, 12) form layered (two-dimensional) hybrid perovskite structures, regardless of the anion (X=Br, I). In this case, hydrogen atoms at both ends of organic cations form hydrogen bonds with halides of inorganic layers. If the organic cation consists of a short even carbon chain (n=2), the authors [35] also predict the formation of a two-dimensional perovskite, although they admit that in practice they observe one-dimensional ribbons consisting of $PbBr_6$ octahedra with common angles that are structurally closely related to each other. That is, there is a kind of transitional case between the 2-D and 1-D structure. Odd alkyl chains behave differently. In [35] these include only the compound $NH_3\text{-}(CH_2)_7\text{-}NH_3PbI_4$, which forms a zero-dimensional (0-D) perovskite from isolated octahedra of lead iodide PbI_6 surrounded by $NH_3\text{-}(CH_2)_7\text{-}NH_3$ cations. The same team in a brief report [36] showed that when using a five-membered alkyl chain with ammonium groups at both ends - $NH_3\text{-}(CH_2)_5\text{-}NH_3$ as an organic cation, a one-dimensional perovskite is formed in which the chains of PbI_6 octahedra are oriented in the direction [111]. Thus, combining the results presented in [33-37] it can be assumed that there is a relationship between the structure of the

organic cation (in particular, the parity and length of the alkyl chain with ammonium groups at both ends) and the dimension of the perovskite formed on their basis. However, due to the fragmentary nature of the results presented in [33-37] such a dependence has not been clearly formulated to date.

In [37] the structure and phase transitions of another representative of hybrid perovskites are studied, in which the organic cation is represented by an even alkyl chain with ammonium groups at both ends – the composition NH_3-$(CH_2)_4$-NH_3PbCl_4. This crystal has a two–dimensional structure (in full accordance with the data [35]) with the traditional orientation of organic and inorganic subsystems - the inorganic layers of $PbCl_6$ octahedra with common angles are separated by layers of organic cation; In this case, the organic cation is oriented in such a way that the hydrogen of the ammonium groups form hydrogen bonds with chlorine.

A distinctive feature of this work is that in it the authors studied in detail and explained the phase transition in this hybrid perovskite, observed at 323.8 K. In the low-temperature phase (at room temperature) $PbCl_6$ octahedra are deformed, lead is displaced from the center, and the NH_3-$(CH_2)_4$-NH_3 organic chain is not centrosymmetric and has a left-sided conformation at one end. The high-temperature phase is characterized by a decrease in the unit cell parameter c from 1.9761 to 1.1011 nm and an increase in the angle β = 94.840 to 102.220. These changes are attributed by the authors [37] to the fact that with increasing temperature the organic cation becomes symmetrical.

Another important work for the subject area under study is devoted to the study of the nature of broadband luminescence and its relationship to structure using the example of a wide range of hybrid perovskites with structurally different organic cations [42]. In the current discourse, this article is important because it describes two hybrid bromide perovskites, in which the organic cation is represented by a four- and eight-membered alkyl chain with two amine groups at the ends. In addition to describing the unit cell of these perovskites, their luminescent properties are described for the first time in [42] In particular, the paper makes an interesting assumption about how the wide- and narrow-band luminescence of hybrid perovskites is related to the

degree of disorganization of inorganic octahedra in their structure. However, the analysis in this work was carried out on a fairly large sample of organic molecules, but heterogeneous in structure.

Table 1 below summarizes the known data on various hybrid perovskites in which the organic cation is represented by an alkyl chain with ammonium groups at both ends.

Table 1. Known data on various hybrid perovskites of the type $(C_n)DAPbX_4$ (n=2-10; X=Cl, Br, I)

The composition of perovskite	X=Cl	X=Br	X=I
$(C_3)DAPbX_4$	[22]: the parameters of the unit cell and the atomic positions in it are determined	[22]: the parameters of the unit cell and the atomic positions in it are determined	[21]: Band gap is determined
$(C_4)DAPbX_4$	[37]: the parameters of the unit cell and atomic positions in it are determined, and a phase transition is detected	[35, 42]: the parameters of the unit cell and the atomic positions in it are determined [28]: the presence of wide- and narrow-band luminescence is shown	[35]: the parameters of the unit cell and the atomic positions in it are determined
$(C_5)DAPbX_4$	-	-	[36]: the parameters of the unit cell and the atomic positions in it are determined
$(C_6)DAPbX_4$	[34]: the parameters of the unit cell are determined, as well as the optical width of the band gap	[34]: the parameters of the unit cell and the atomic positions in it, as well as the optical width of the band gap, are determined	[34]: the parameters of the unit cell and the atomic positions in it, as well as the optical width of the band gap, are determined
$(C_7)DAPbX_4$	-	-	[35]: the parameters of the unit cell and the atomic positions in it are determined
$(C_8)DAPbX_4$	-	[42]: the parameters of the unit cell and atomic positions in it are determined, the presence of wide- and narrow-band luminescence is shown	[35]: the parameters of the unit cell and the atomic positions in it are determined

It can be seen from the above table that the outlined circle of hybrid crystals has been studied extremely fragmentally. For most of the studied compositions, only the

parameters of the unit cell have been determined, only for three of them there is data on the width of the forbidden zone. The presence of a phase transition has been established for only one.

Conclusions on the 1 chapter

1) There is no systematic data in open sources on the study of the properties of hybrid compounds based on lead halides and a homological series of diamines of the form $[H_3N\text{-}(CH_2)_n\text{-}NH_3]PbX_4$ (n=4-8, X=Cl, Br, I). Crystal structure data are missing for some compounds from this set.
2) Since there is no systematic data, it is impossible to analyze the effect of organic cation and halide anion on the structural, electronic and optical properties of hybrid compounds.

Chapter 2. MATERIALS AND METHODS

2.1 Materials

Lead bromide ($PbBr_2$, purity 99%, Macklin), lead iodide (PbI_2, purity 98%, Macklin), Lead chloride ($PbCl_2$, purity 98%, Macklin), hydrochloric acid (HI, 57% aqueous solution, Macklin), hydrobromic acid (HBr, 48% aqueous solution, Aladdin), hydrochloric acid (HCl, 36% aqueous solution, chemically pure, ECOS-1), hypophosphoric acid (H_3PO_2, 50% aqueous solution, Macklin), butanediamine-1,4 ($C_4H_{12}N_2$, purity 99%, Macklin), pentanediamine-1,5 ($C_5H_{14}N_2$, purity 98%, Macklin), hexanediamine-1,6 ($C_6H_{16}N_2$, purity 99%, Macklin), heptanediamine-1,7 ($C_7H_{18}N_2$, purity 98%, Macklin), octanediamine-1,8 ($C_8H_{20}N_2$, 98% purity, Macklin), acetone (C_3H_6O, 99,8% purity, chemically pure, ECOS-1). All reagents were used without additional purification.

The structure of organic molecules acting as cations in the hybrid crystals under study is shown in Figure 3.

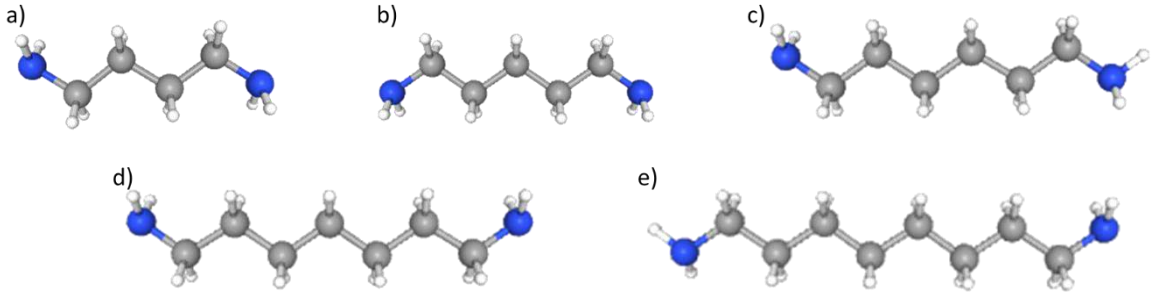

Figure 3. The structure of organic molecules acting as cations in the studied hybrid crystals**:** a) butanediamine-1,4 (C_4DA), b) pentanediamine-1,5 (C_5DA), c) hexanediamine-1,6 (C_6DA), d) heptanediamine-1,7 (C_7DA), and e) octanediamine-1,8 (C_8DA).

2.2 Synthesis methods

Synthesis **1** $[H_3N(CH_2)_4NH_3]PbI_4$: lead iodide PbI_2 (2,00 g; 4,34 mmol) was dissolved in 9 ml of hydrochloric acid, separately butanediamine-1,4 (0,38 g; 4,34 mmol) was dissolved in 9 ml of hydrochloric acid. Then the resulting solutions were mixed, after which a yellow-orange precipitate fell out within a few minutes. Next, 2 drops of hypophosphoric acid were added to the reaction mixture (for reduction iodide impurities to the iodide ion and prevent further oxidation of the iodide ion) and heated until the precipitate completely dissolved, after which it was left to cool to room temperature, followed by the formation of a crystalline precipitate for several hours. The resulting crystalline precipitate was filtered on a porous glass filter, washed once with 2 ml of cooled (2-4°C) hydrochloric acid, then washed three times with acetone (5 ml at a time) and finally dried in a vacuum drying cabinet at 50°C/10 mbar.

Synthesis **2** $[H_3N(CH_2)_4NH_3]PbBr_4$: lead bromide $PbBr_2$ (2,00 g; 5,45 mmol) was dissolved in 9 ml of hydrobromic acid, separately butanediamine-1,4 (0,48 g; 5,45 mmol) was dissolved in 9 ml of hydrobromic acid. Then the resulting solutions were mixed, after which a white precipitate fell out within a few minutes. Next, the reaction mixture was heated until the precipitate was completely dissolved, after which it was left to cool to room temperature, followed by the formation of a crystalline precipitate for several hours. The resulting crystalline precipitate was filtered on a porous glass filter, washed once with 2 ml of cooled (2-4°C) hydrobromic acid, then washed three times with acetone (5 ml at a time) and finally dried in a vacuum drying cabinet at 50°C/10 mbar.

Synthesis **3** $[H_3N(CH_2)_4NH_3]PbCl_4$: $PbCl_2$ lead chloride (2,00 g; 7,19 mmol) was placed in a 75 ml thick-walled glass vessel with a screw-down Teflon stopper and a Teflon magnetic anchor, 47 ml of hydrochloric acid was added, then a separately obtained solution of butanediamine-1,4 (0,63 g; 7,19 mmol) was added to 9 ml of hydrochloric acid. The vessel with the reaction mixture was closed with a screw-down

Teflon stopper equipped with an O-ring, placed in a water bath with a magnetic stirrer and stirred at a temperature of about 95°C until lead chloride was completely dissolved. The resulting transparent solution, cooled to room temperature, was poured into a 100 ml glass and left to stand in a fume hood in order to slowly evaporate the solvent, after which transparent crystals formed for several days. The resulting crystals were filtered on a porous glass filter, washed once with 2 ml of cooled (2-4°C) hydrochloric acid, then washed three times with acetone (5 ml at a time) and finally dried in a vacuum drying cabinet at 50°C/10 mbar.

Synthesis **4** $[H_3N(CH_2)_5NH_3]PbI_4$: lead iodide PbI_2 (2,00 g; 4,34 mmol) was dissolved in 9 ml of hydrochloric acid, separately pentanediamine-1,5 (0,44 g; 4,34 mmol) was dissolved in 9 ml of hydrochloric acid. Then the resulting solutions were mixed, after which a yellow-orange precipitate fell out within a few minutes. Further actions are similar to those described in synthesis **1**.

Synthesis **5** $[H_3N(CH_2)_5NH_3]PbBr_4$: lead bromide $PbBr_2$ (2,00 g; 5,45 mmol) was dissolved in 9 ml of hydrobromic acid, separately pentanediamine-1,5 (0,56 g; 5,45 mmol) was dissolved in 9 ml of hydrobromic acid. Then the resulting solutions were mixed, after which a white precipitate fell out within a few minutes. Further actions are similar to those described in synthesis **2**.

Synthesis **6** $[H_3N(CH_2)_5NH_3]PbCl_4$: the synthesis procedure is similar to that described in synthesis **3**, while pentanediamine-1,5 (0,73 g; 7,19 mmol) was used instead of butanediamine-1,4.

Synthesis **7** $[H_3N(CH_2)_6NH_3]PbI_4$: lead iodide PbI_2 (2,00 g; 4,34 mmol) was dissolved in 9 ml of hydrochloric acid, separately hexanediamine-1,6 (0,50 g; 4,34 mmol) was dissolved in 9 ml of hydrochloric acid. Then the resulting solutions were mixed, after which a yellow-orange precipitate fell out within a few minutes. Further actions are similar to those described in synthesis **1**.

Synthesis **8** $[H_3N(CH_2)_6NH_3]PbBr_4$: lead bromide $PbBr_2$ (2,00 g; 5,45 mmol) was dissolved in 9 ml of hydrobromic acid, separately hexanediamine-1,6 (0,63 g; 5,45 mmol) was dissolved in 9 ml of hydrobromic acid. Then the resulting solutions were

mixed, after which a white precipitate fell out within a few minutes. Further actions are similar to those described in synthesis **2**.

Synthesis **9** $[H_3N(CH_2)_6NH_3]PbCl_4$: the synthesis procedure is similar to that described in synthesis **3**, while hexanediamine-1,6 (0,83 g; 7,19 mmol) was used instead of butanediamine-1,4.

Synthesis **10** $[H_3N(CH_2)_7NH_3]PbI_4$: lead iodide PbI_2 (2,00 g; 4,34 mmol) was dissolved in 9 ml of hydrochloric acid, separately heptanediamine-1,7 (0,56 g; 4,34 mmol) was dissolved in 9 ml of hydrochloric acid. Then the resulting solutions were mixed, after which a yellow-orange precipitate fell out within a few minutes. Further actions are similar to those described in synthesis **1**.

Synthesis **11** $[H_3N(CH_2)_7NH_3]PbBr_4$: lead bromide $PbBr_2$ (2,00 g; 5,45 mmol) was dissolved in 9 ml of hydrobromic acid, separately heptanediamine-1,7 (0,71 g; 5,45 mmol) was dissolved in 9 ml of hydrobromic acid. Then the resulting solutions were mixed, after which a white precipitate fell out within a few minutes. Further actions are similar to those described in synthesis **2**.

Synthesis **12** $[H_3N(CH_2)_7NH_3]PbCl_4$: the synthesis procedure is similar to that described in synthesis **3**, while heptanediamine-1,7 (0,94 g; 7,19 mmol) was used instead of butanediamine-1,4.

Synthesis **13** $[H_3N(CH_2)_8NH_3]PbI_4$: lead iodide PbI_2 (2,00 g; 4,34 mmol) was dissolved in 9 ml of hydrochloric acid, separately octandiamine-1,8 (0,62 g; 4,34 mmol) was dissolved in 9 ml of hydrochloric acid. Then the resulting solutions were mixed, after which a yellow-orange precipitate fell out within a few minutes. Further actions are similar to those described in synthesis **1**.

Synthesis **14** $[H_3N(CH_2)_8NH_3]PbBr_4$: lead bromide $PbBr_2$ (2,00 g; 5,45 mmol) was dissolved in 9 ml of hydrobromic acid, separately octandiamine-1,8 (0,78 g; 5,45 mmol) was dissolved in 9 ml of hydrobromic acid. Then the resulting solutions were mixed, after which a white precipitate fell out within a few minutes. Further actions are similar to those described in synthesis **2**.

Synthesis **15** $[H_3N(CH_2)_8NH_3]PbCl_4$: $PbCl_2$ lead chloride (2,00 g; 7,19 mmol) was placed in a 75 ml thick-walled glass vessel with a screw-down Teflon stopper and a

Teflon magnetic anchor, 47 ml of hydrochloric acid was added, then a separately obtained solution of octandiamine-1,8 (1,04 g; 7,19 mmol) was added to 9 ml of hydrochloric acid. The vessel with the reaction mixture was closed with a screw-down Teflon stopper equipped with an O-ring, placed in a water bath with a magnetic stirrer and stirred at a temperature of about 95°C until lead chloride was completely dissolved. The resulting transparent solution was cooled to room temperature. During the cooling process, an "airy" fine crystalline precipitate was formed. The resulting precipitate was filtered on a porous glass filter, washed once with 2 ml of cooled (2-4°C) hydrochloric acid, then washed three times with acetone (5 ml at a time) and finally dried in a vacuum drying cabinet at 50°C/10 mbar.

2.3 Measurement methods

For some of the objects of study (see Table 1), data on the crystal lattice were obtained earlier by other research groups. Therefore, the Powder XRD method was used to confirm the phase composition of these hybrid perovskites. Patterns XRD were recorded on a Colibri diffractometer (Burevestnik, Russia). The study was carried out using a copper X-ray tube with a current strength of 10 mA and a voltage of 40 kV (CuK_α radiation of 1,5406 Å) paired with a detector in the Bragg-Brentano geometry (2θ) in an optical circuit without a monochromator with a goniometer radius of 150 mm. A Ni-filter was used to exclude the profiles of the K_β line. Reflected radiation was detected by the Mythen2 linear detector. The shooting was carried out in the range of angles 2° from 5° to 80°.The shooting step was 0,01875°, the accumulation time was 78 seconds per step. The refinement of the phases was carried out by the Rietveld method using the TOPAS 4.2 software package [43].

The structures of the elementary cells of hybrid crystal samples at different temperatures (100 and 323 K) were determined by single crystal X-ray diffraction (SCXRD) on a Bruker Kappa Apex II diffractometer with graphite-monochromatized MoK_{α} radiation. Data processing and absorption correction were performed using original software.

Differential scanning calorimetry (DSC) was performed on a METTLER TOLEDO Thermal Analysis System DISC 3 device. Samples in the form of polycrystalline powder weighing 30-50 mg were placed in aluminum crucibles with a volume of 40 μl, which were examined in the temperature range from -90°C to 150°C in an argon atmosphere at a heating/cooling rate of 7 °C min^{-1}.

The optical properties of the studied samples were studied by diffuse reflection spectroscopy. Diffuse reflection spectra in the form $A(\lambda)=1-R(\lambda)$, where A is the absorption coefficient, R is the reflection coefficient, λ is the wavelength of radiation, were recorded in the spectral range from 250 to 800 nm at room temperature using a UV-Visible PerkinElmer Lambda 950 spectrophotometer (Great Britain) equipped with an integrating sphere of 150 mm. Spectralon was used as a reference for comparison.

Low-temperature photoluminescence spectra and luminescence excitation spectra were recorded in the spectral range of 250-800 nm using a FL 8500 PerkinElmer fluorescence spectrometer at a temperature of 77 K using a low-temperature PerkinElmer cell holder.

The charge states in which elements are present in hybrid perovskites of various compositions, as well as the ceiling of the valence band and the output operation, were studied by X-ray photoelectron spectroscopy (XPS) using a SPECS spectrometer (Germany) using $MgK_{\square}$ radiation (hν = 1253,6 eV, 150 W). The binding energy scale was pre-calibrated by the position of the peaks of the core levels of gold and copper: $Au4f_{7/2}$ - 84.0 eV and $Cu2p_{3/2}$ - 932.67 eV. The pressure of the residual gases during the measurements did not exceed $8\square10^{-9}$ mbar. The samples were applied to a standard holder using double-sided conductive copper tape (Scotch 3M©). The Pb4f (138.8 eV) line from lead in halides was used as an internal standard for calibration of

photoelectronic peaks [44]. The processing of the received spectral information was carried out using the XPSPeak 4.1 program.

2.4 Methods of numerical calculations and computer modeling

Modeling of materials is carried out using the ABINIT 8.6.3 software package, which implements the computational approach of the Density Functional Theory (DFT) method with periodic boundary conditions. The corresponding pseudopotentials are used as the atomic basis in this software package. The initial crystal structures for such modeling were experimental data obtained by X-ray diffraction. As a result of modeling, such characteristics of the structure under study as the equilibrium geometries of crystal structures, their energies, band structures and densities of electronic states, as well as optical absorption and Raman scattering spectra, etc. can be obtained.

Conclusions on the 2 chapter

ч

The work carried out allows us to formulate the following main conclusion on the chapter:A method for producing hybrid crystals based on lead halides and a homologous series of diamines of the form $[H_3N\text{-}(CH_2)_n\text{-}NH_3]PbX_4$ (n=4-8, X=Cl, Br, I) has been optimized.

Chapter 3. EXPERIMENTAL RESULTS

This chapter presents data on the experimental characterization of the studied hybrid perovskites, in which the organic cation is represented by an alkyl chain of various lengths with two amine groups at the ends, and the anion is represented by halogens, chlorine, bromine or iodine (hereinafter referred to as the objects of research), as well as the results of their quantum chemical modeling.

3.1 Crystal structure of hybrid compounds based on lead halides and homologous series of limiting diamines of the form $[H_3N\text{-}(CH_2)_n\text{-}NH_3]PbX_4$ (n=4-8, X=Cl, Br, I)

3.1.1 Powder XRD

It was shown above (see Table 1) that for some of the studied hybrid perovskites, crystal structures were studied earlier. Therefore, the method of powder X-ray phase analysis was used to confirm the formation of the target phase of these hybrid perovskites and their phase uniformity. Figures 4-18 shows experimental XRD patterns of these hybrid perovskites in comparison with calculated radiographs obtained from known structures [59]. The elementary cells for this purpose were taken from an open crystallographic database [45].

The excellent correspondence of the calculated XRD patterns with the experimental ones for all the samples considered is visible. That is, it can be stated that in all cases, the formation of hybrid perovskite crystals occurred, the elementary cells of which are identical to those described earlier.

For crystals for which the structure was not established either earlier or in the present study due to the inability to grow them in the form of a single crystal ($(C_8)DAPbCl_4$ and $(C_7)DAPbBr_4$) powder XRD patterns are still quite characteristic and allow us to assert that these crystals are formed two-dimensional.

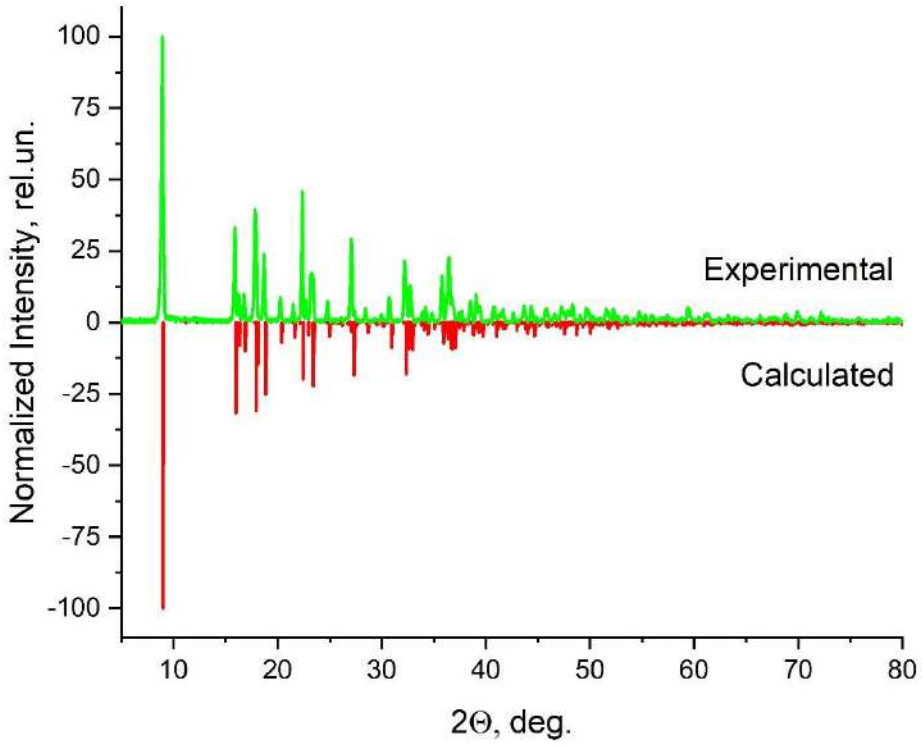

Figure 4. XRD patterns of a hybrid crystal $(C_4)DAPbCl_4$ (green line above) compared to the calculated one based on the known structure (CCDC # 1501643, The red line at the bottom).

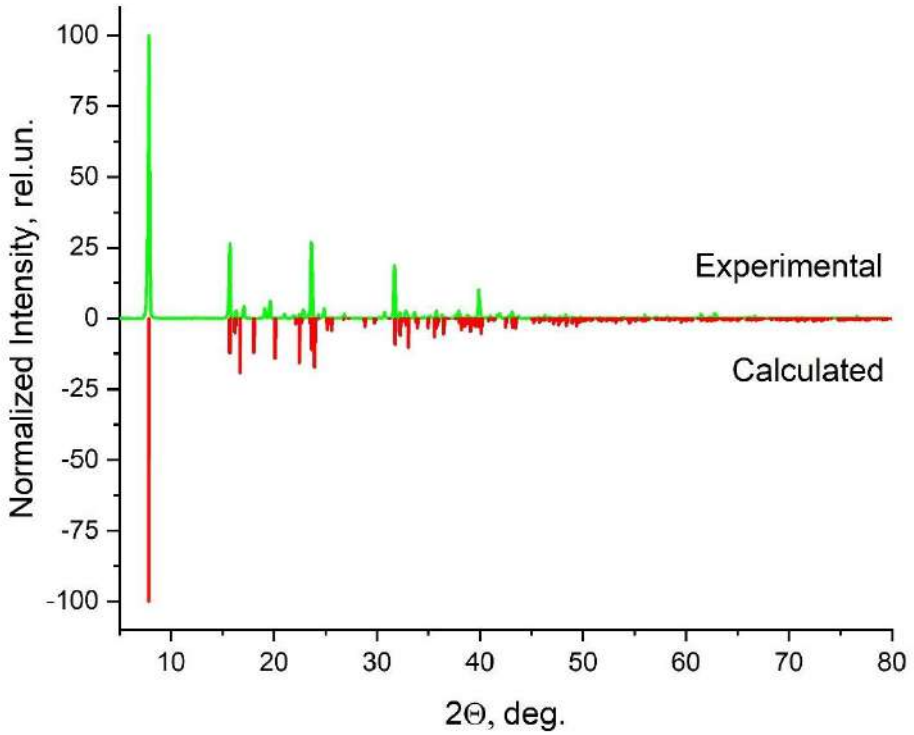

Figure 5. XRD patterns of a hybrid crystal $(C_5)DAPbCl_4$ (green line at the top) in comparison with the calculated structure based on the structure established in this study (see section 3.1.2, red line at the bottom).

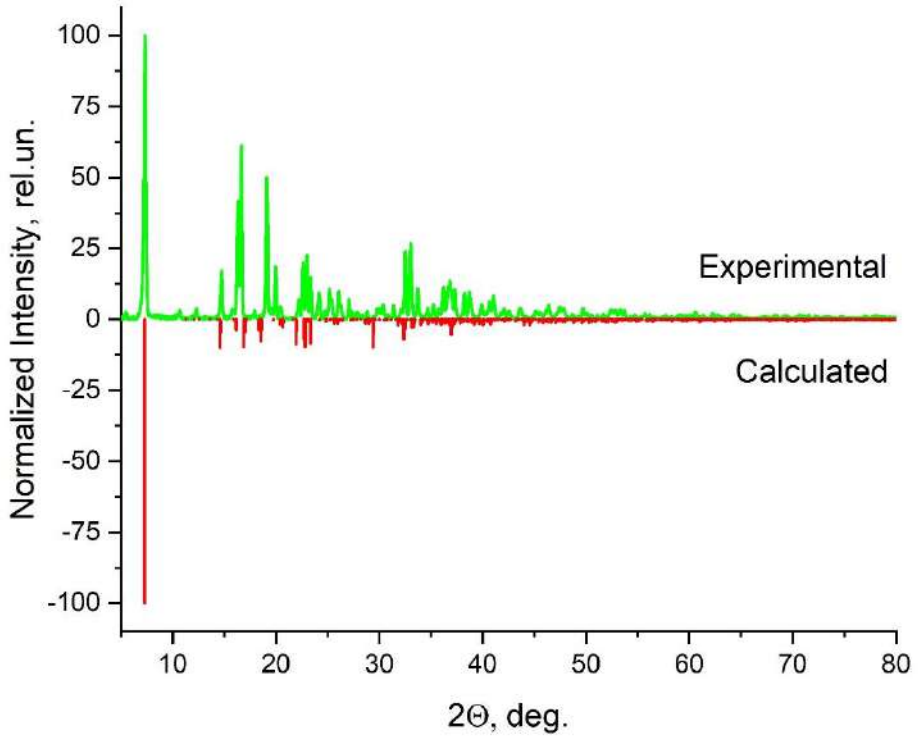

Figure 6. XRD patterns of a hybrid crystal $(C_6)DAPbCl_4$ (green line at the top) in comparison with the calculated structure based on the structure established in this study (see section 3.1.2, red line at the bottom).

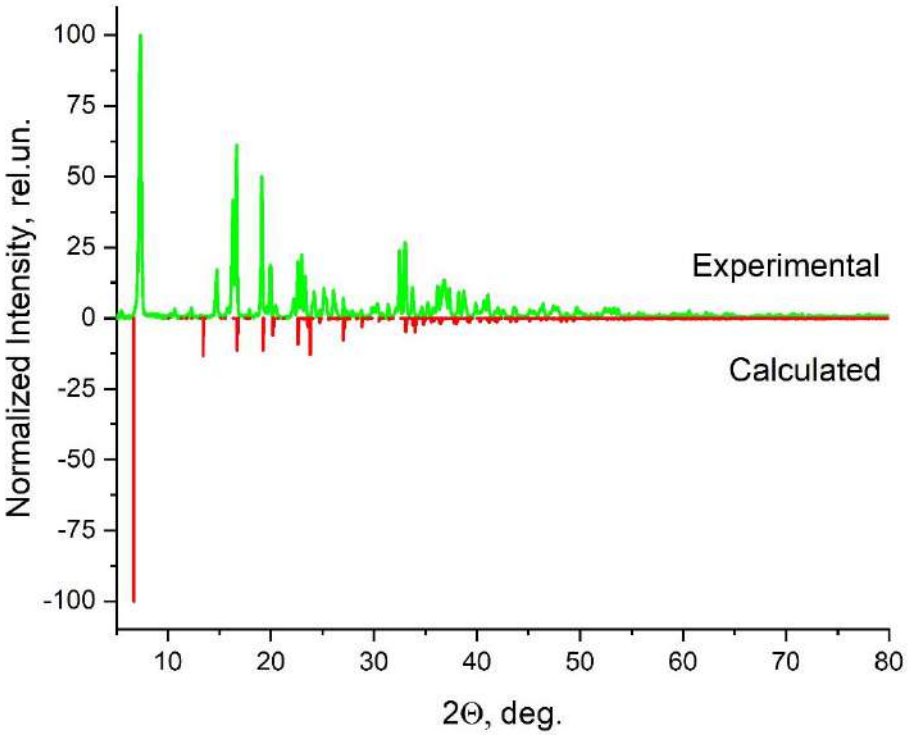

Figure 7. XRD patterns of a hybrid crystal $(C_7)DAPbCl_4$ (green line at the top) in comparison with the calculated structure based on the structure established in this study (see section 3.1.2, red line at the bottom).

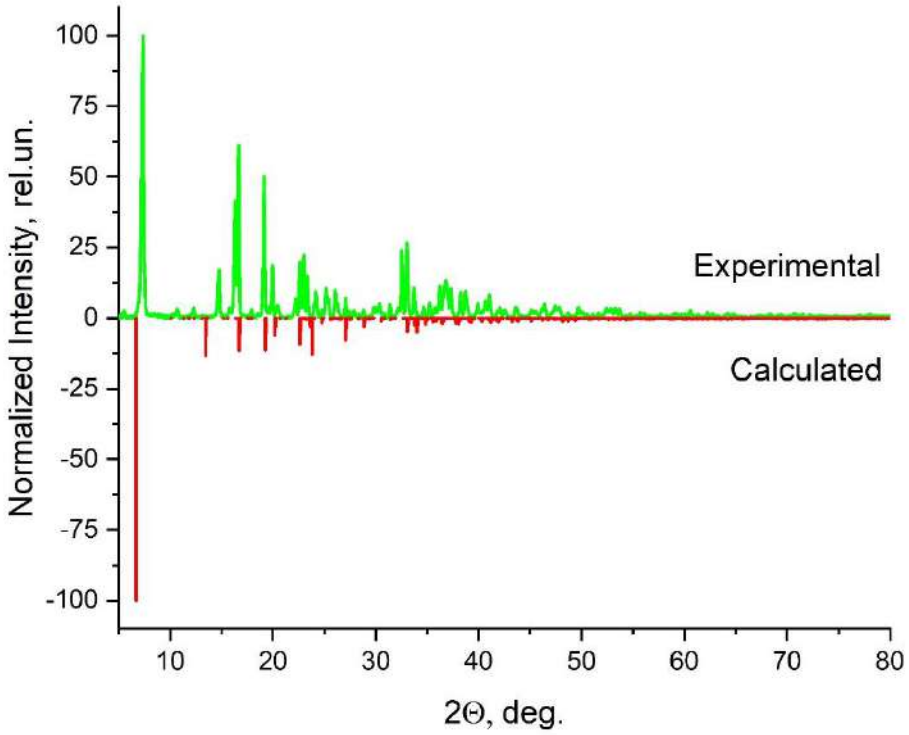

Figure 8. XRD patterns of the hybrid crystal $(C_8)DAPbCl_4$ (green line at the top) in comparison with the calculated structure based on the structure established in this study (see section 3.1.2, red line at the bottom).

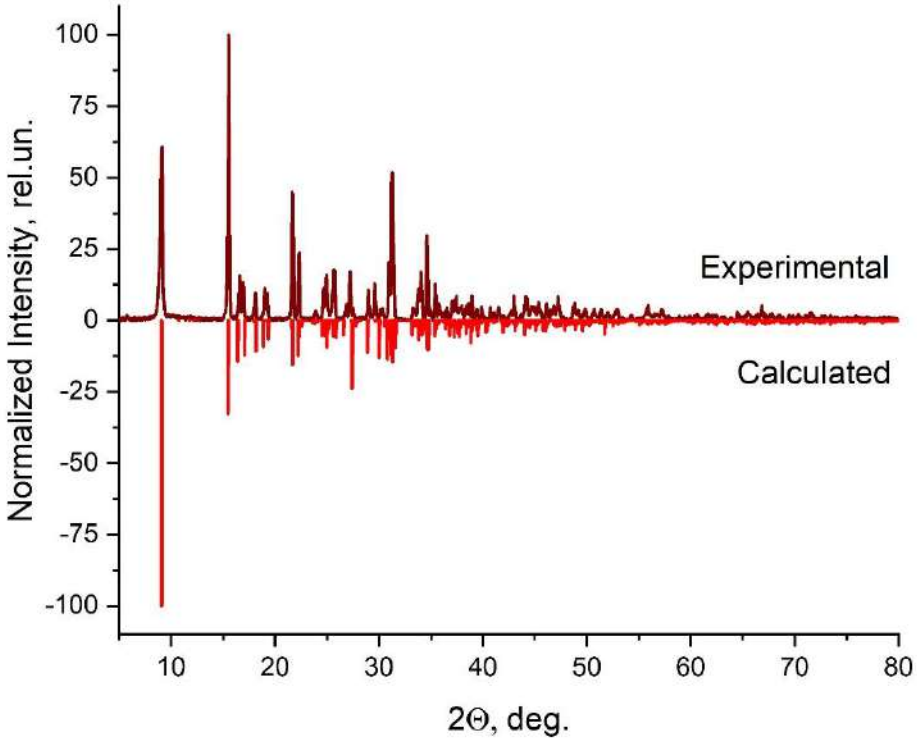

Figure 9. XRD patterns of a hybrid crystal $(C_4)DAPbBr_4$ (dark red line at the top) compared to the calculated one based on the known structure (CCDC # 1545802, red line at the bottom).

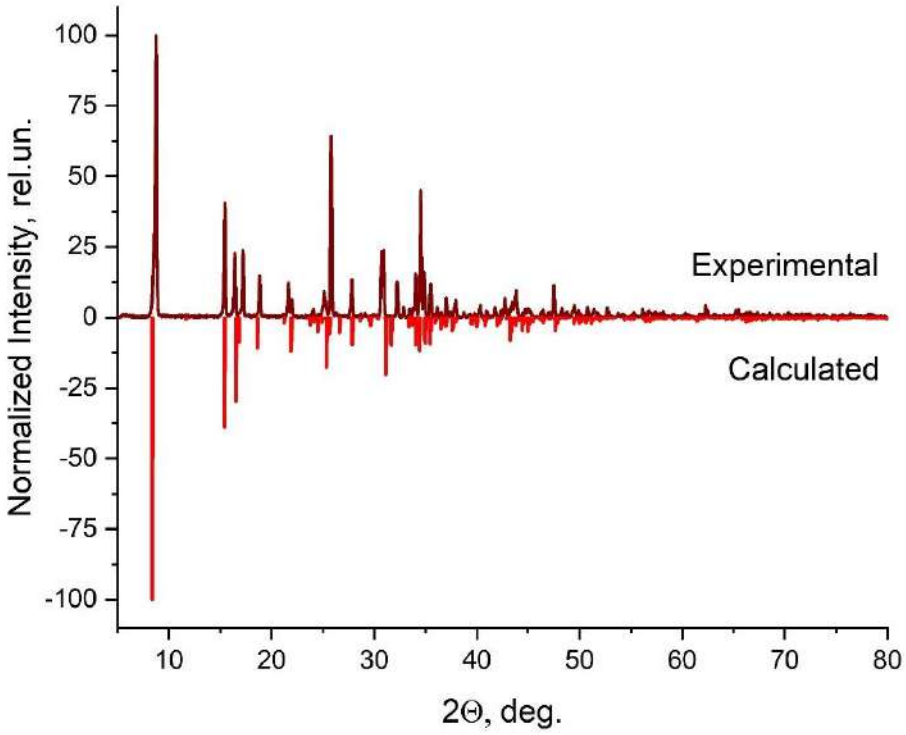

Figure 10. XRD patterns of a hybrid crystal $(C_5)DAPbBr_4$ (dark red line at the top) in comparison with the calculated structure based on the structure established in this study (see section 3.1.2, red line at the bottom).

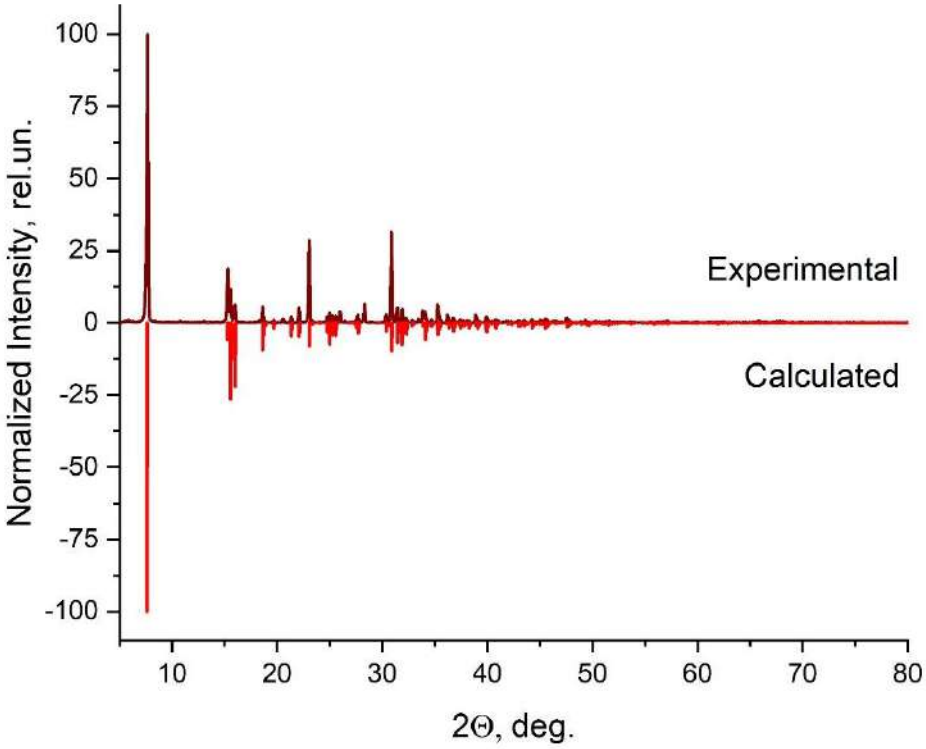

Figure 11. XRD patterns of a hybrid crystal $(C_6)DAPbBr_4$ (dark red line at the top) compared to the calculated one based on the known structure (CCDC # 7203880, red line at the bottom).

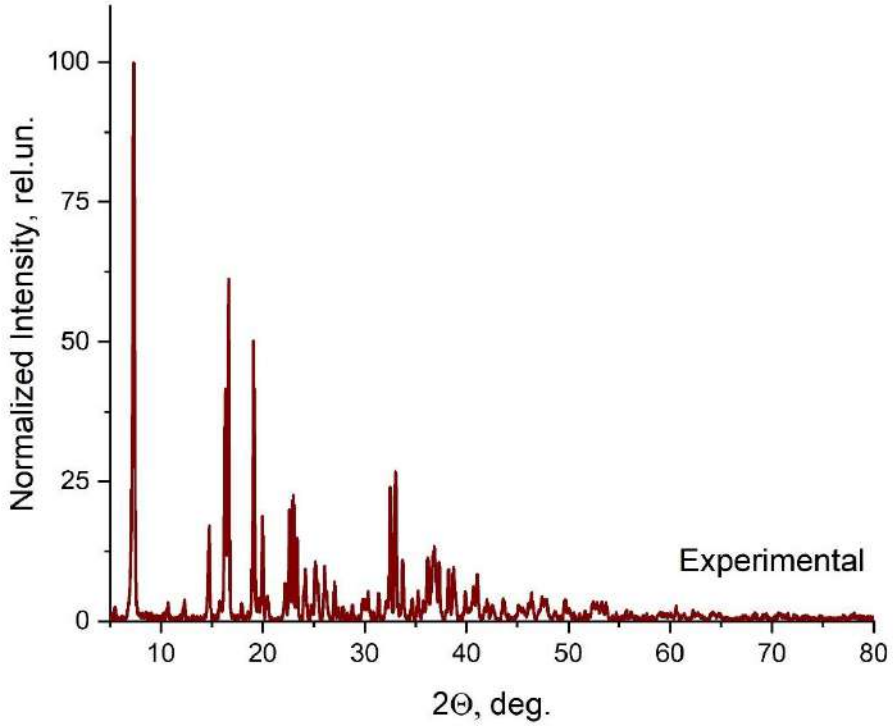

Figure 12. XRD patterns of a hybrid crystal $(C_7)DAPbBr_4$

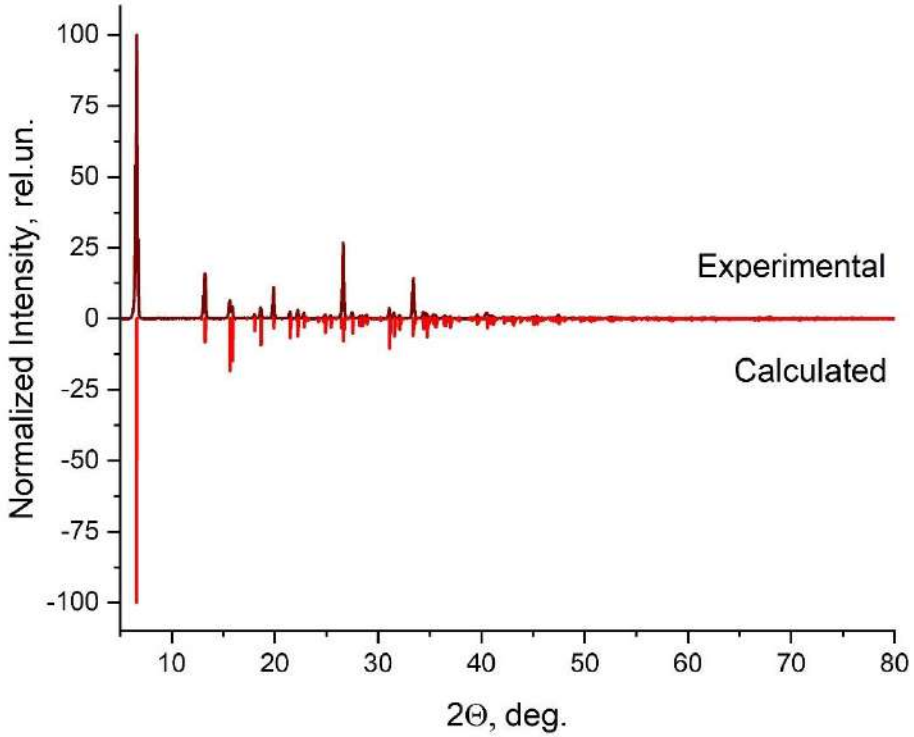

Figure 13. XRD patterns of the hybrid crystal $(C_8)DAPbBr_4$ (dark red line at the top) compared to the calculated one based on the known structure (CCDC # 1545806, red line at the bottom).

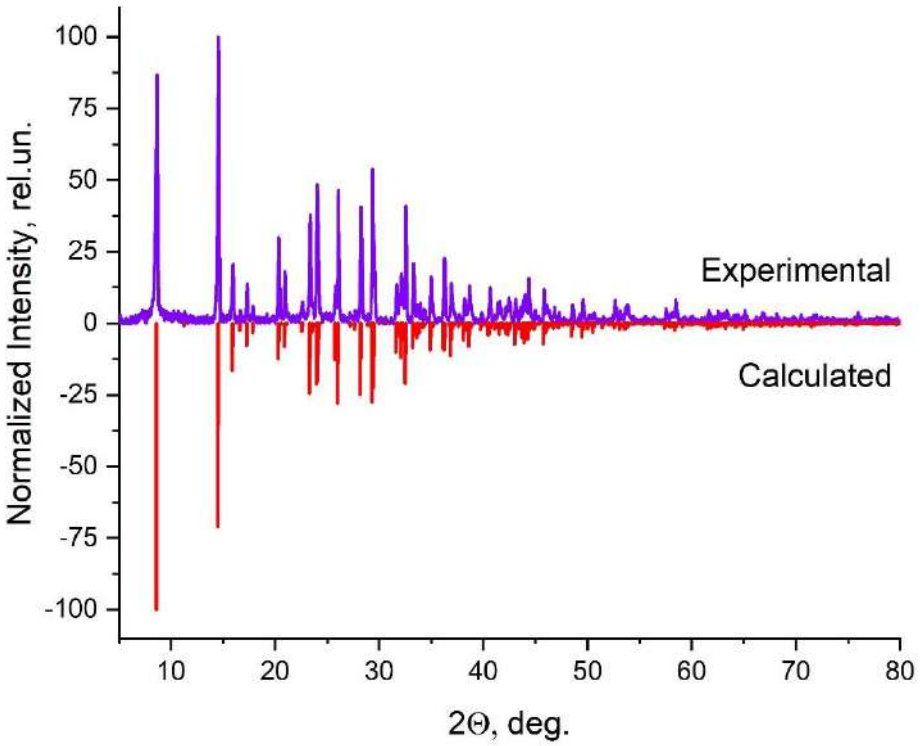

Figure 1. XRD patterns of a hybrid crystal $(C_4)DAPbI_4$ (purple line at the top) compared to the calculated one based on the known structure (CCDC # 7207475, red line at the bottom).

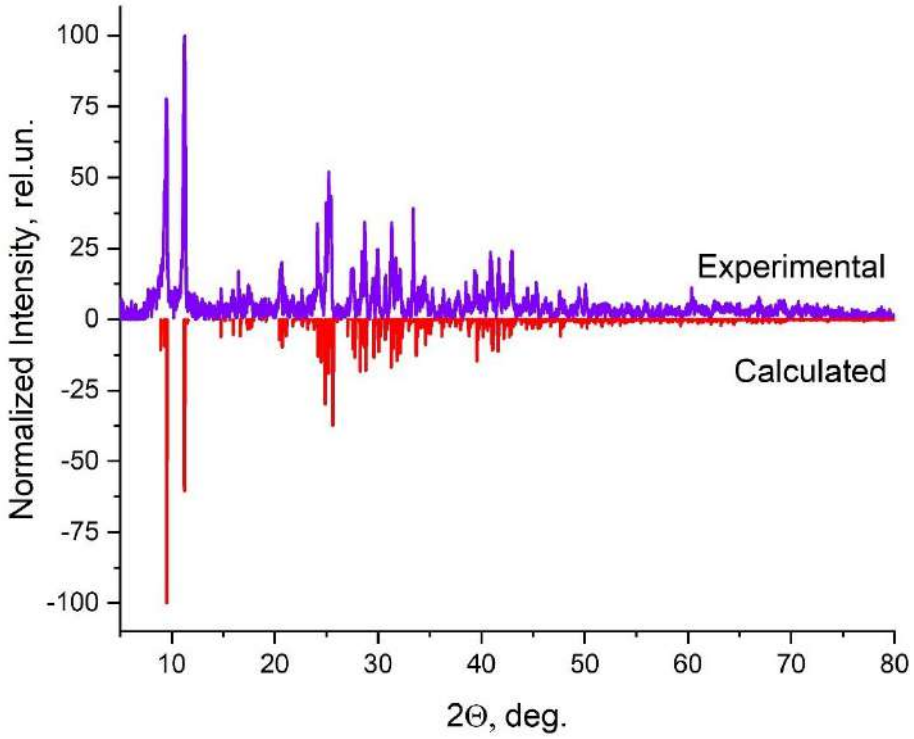

Figure 2. XRD patterns of a hybrid crystal $(C_5)DAPbI_4$ (purple line at the top) in comparison with the calculated one based on the known structure ([44], red line at the bottom).

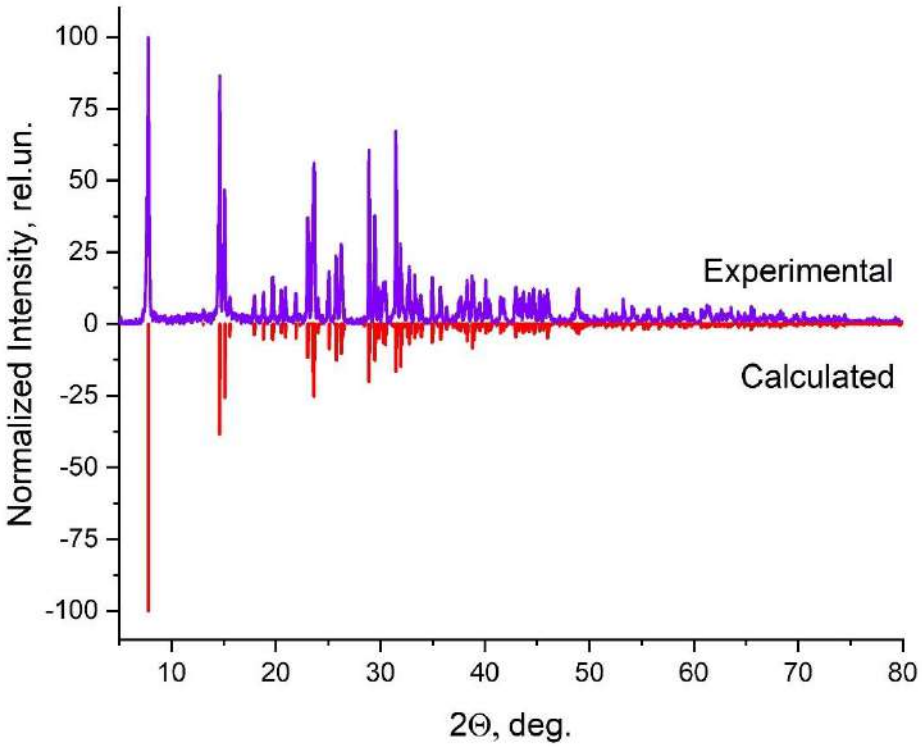

Figure 3. XRD patterns of the hybrid crystal $(C_6)DAPbI_4$ (purple line at the top) compared to the calculated one based on the known structure (CCDC # 7203879, red line at the bottom).

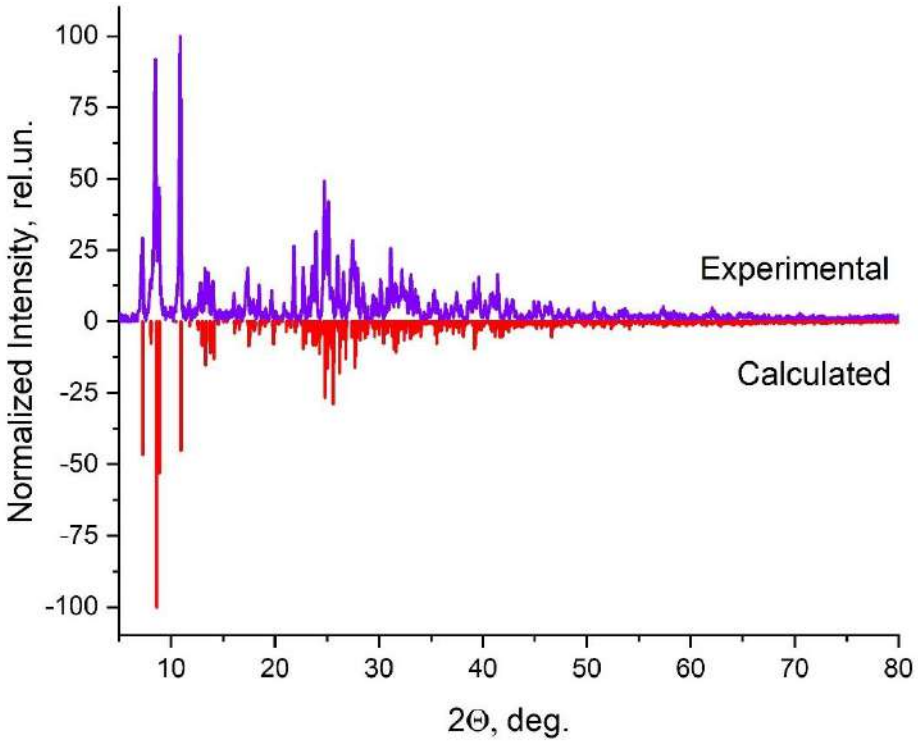

Figure 4. XRD patterns of a hybrid crystal $(C_7)DAPbI_4$ (purple line at the top) compared to the calculated one based on the known structure (CCDC # 7207476, red line at the bottom).

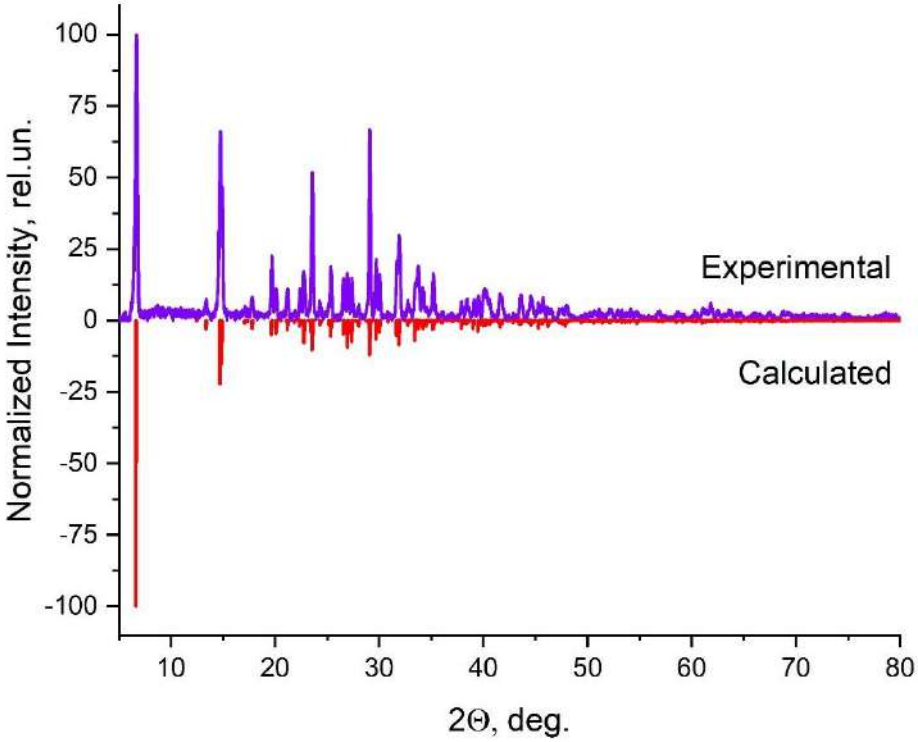

Figure 5. XRD patterns of a hybrid crystal $(C_8)DAPbI_4$ (purple line at the top) compared to the calculated one based on the known structure (CCDC # 7207477, red line at the bottom).

3.1.2 Single crystal XRD

For those samples of hybrid crystal structures for which the structures were not previously described, the method of X-ray diffraction analysis was applied. Figure 19-23 shows the elementary cells of the new structures described for the first time in this study [50], [56], [59].

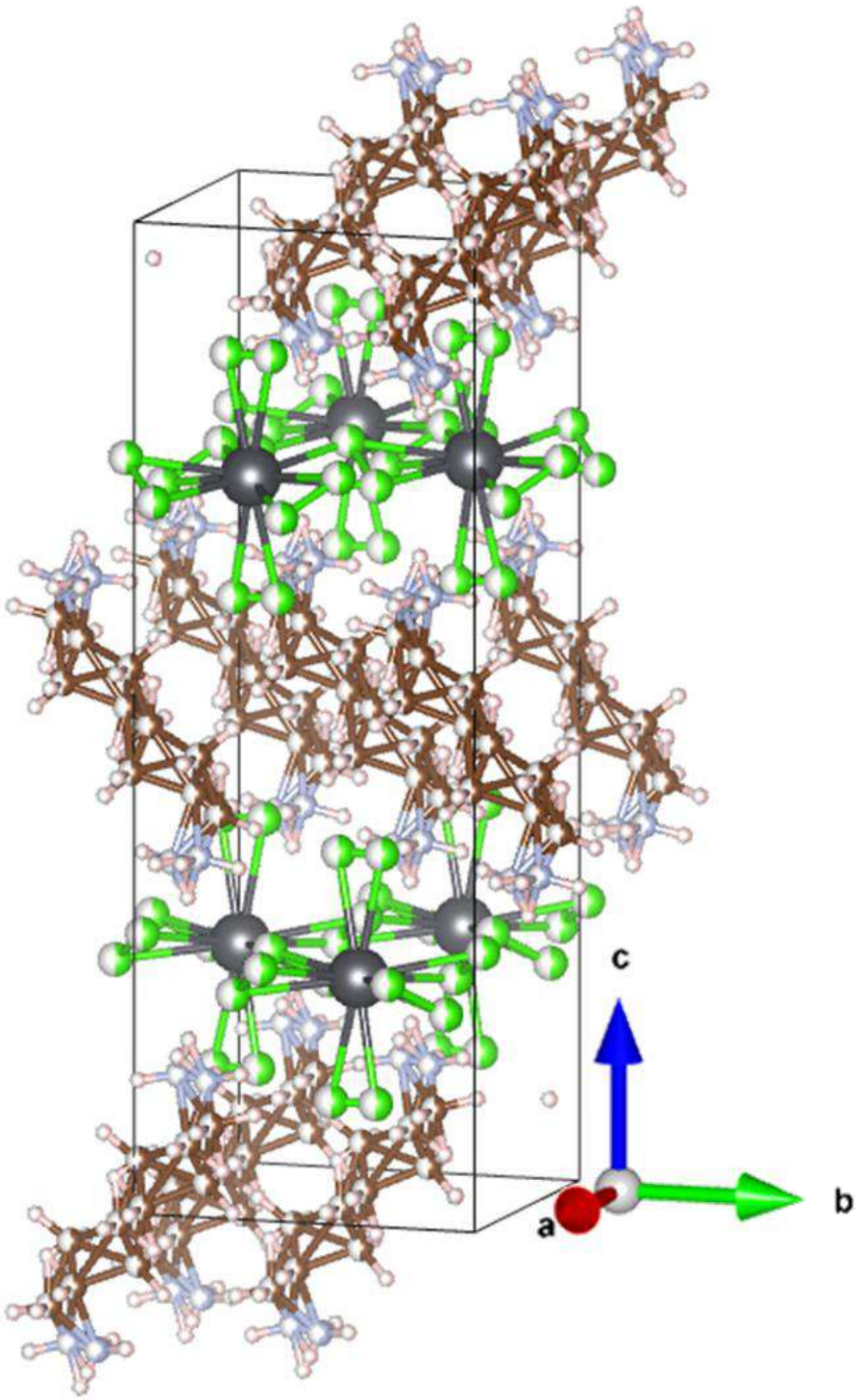

Figure 19. Model of the unit cell of a hybrid crystal $(C_5)DAPbCl_4$: gray balls are lead atoms, green ones are chlorine atoms, brown ones are carbon, light gray ones are nitrogen, light brown ones are hydrogen.

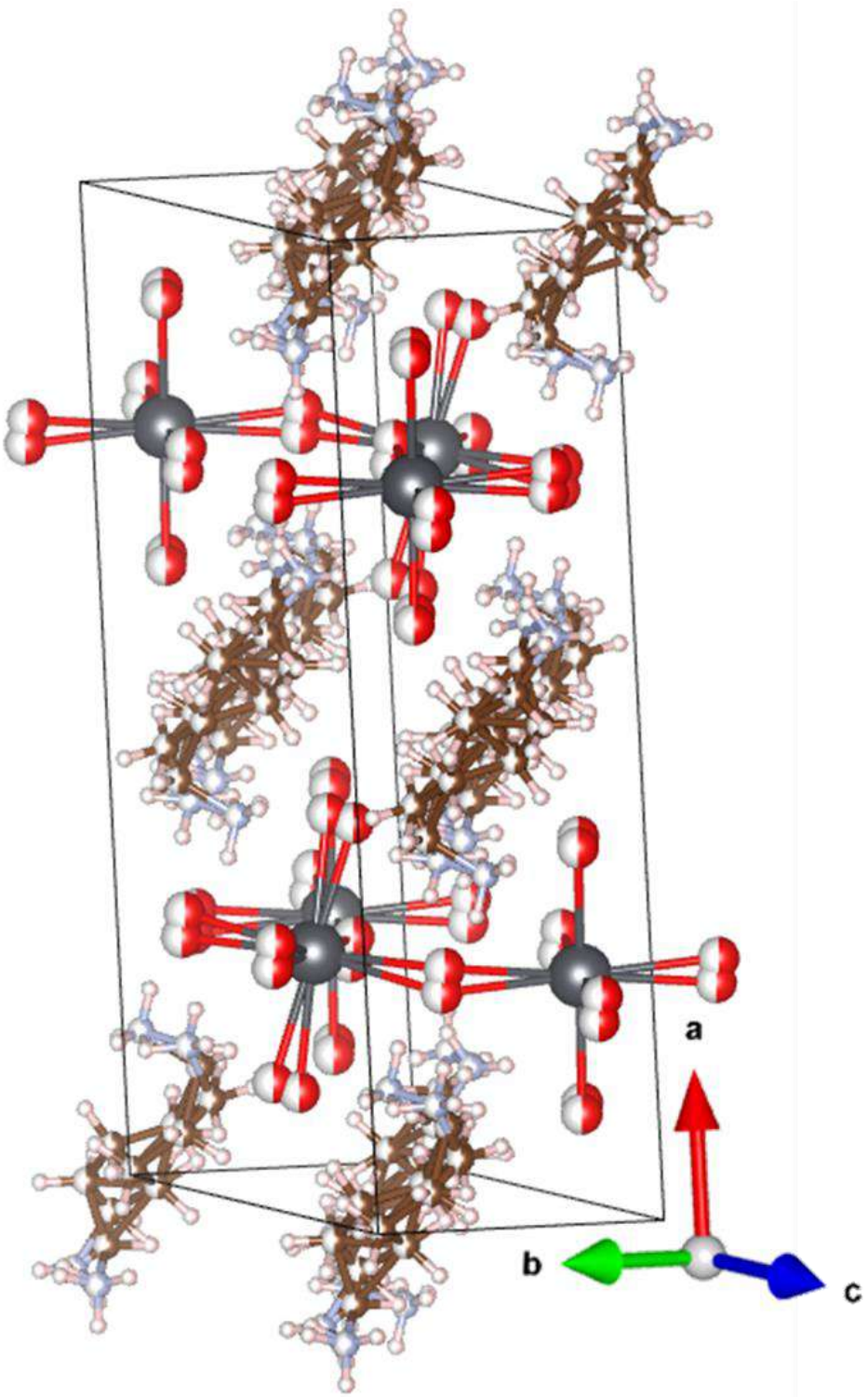

Figure 20. Model of the unit cell of a hybrid crystal $(C_5)DAPbBr_4$: gray balls are lead atoms, red ones are bromine atoms, brown ones are carbon, light gray ones are nitrogen, light brown ones are hydrogen.

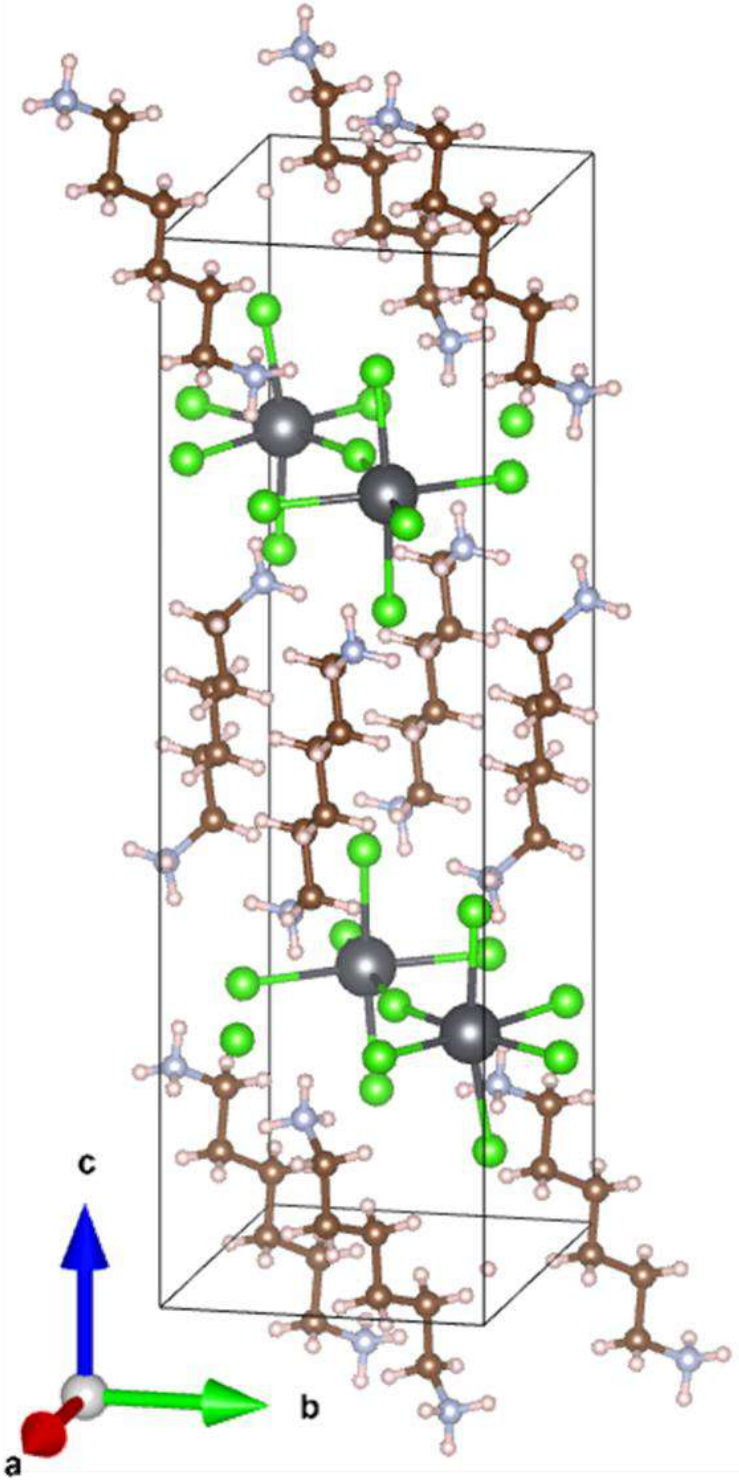

Figure 21. Model of the unit cell of a hybrid crystal $(C_6)DAPbCl_4$: gray balls are lead atoms, green ones are chlorine atoms, brown ones are carbon, light gray ones are nitrogen, light brown ones are hydrogen.

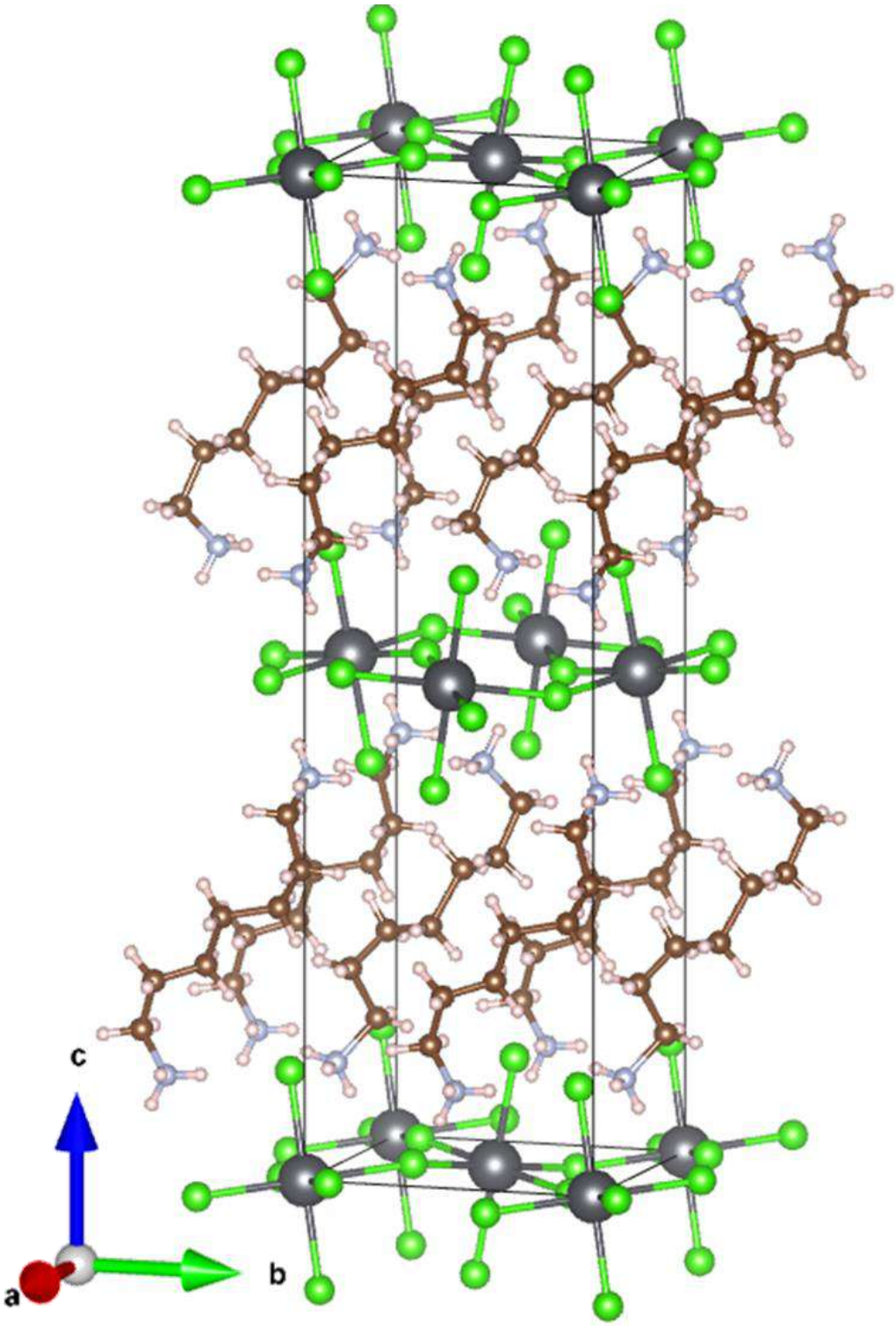

Figure 22. Model of the unit cell of a hybrid crystal $(C_7)DAPbCl_4$: gray balls are lead atoms, green ones are chlorine atoms, brown ones are carbon, light gray ones are nitrogen, light brown ones are hydrogen.

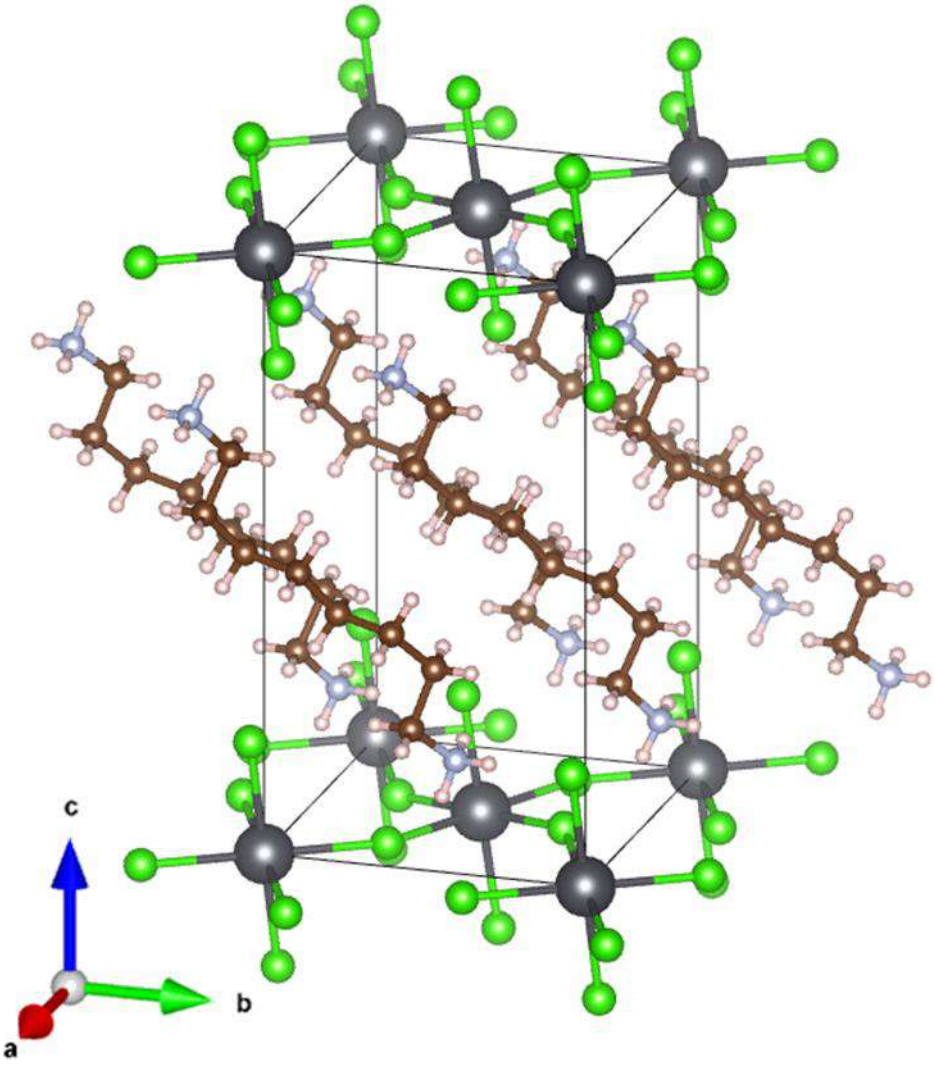

Figure 23. Model of the unit cell of a hybrid crystal $(C_8)DAPbCl_4$: gray balls are lead atoms, green ones are chlorine atoms, brown ones are carbon, light gray ones are nitrogen, light brown ones are hydrogen.

The data obtained indicate that all hybrid crystals are two-dimensional with planes of $PbHal_6$ octahedra, between which diamine molecules oriented by NH_3 groups towards inorganic planes are located.

3.1.3 Analysis of the dependence of the structure of hybrid compounds based on lead halides and the homologous series of limiting diamines of the form $[H_3N\text{-}(CH_2)_n\text{-}NH_3]PbX_4$ on the length of the organic chain and the halogen

The data known from the literature and obtained in the course of this study on the structure of the elementary cells of hybrid crystals of various compositions allow us to analyze how the halogen and the length of the organic cation affect various structural parameters. Figure 24 - Figure 28 shows images of all the studied crystal structures, for which data on the structure of elementary cells were obtained.

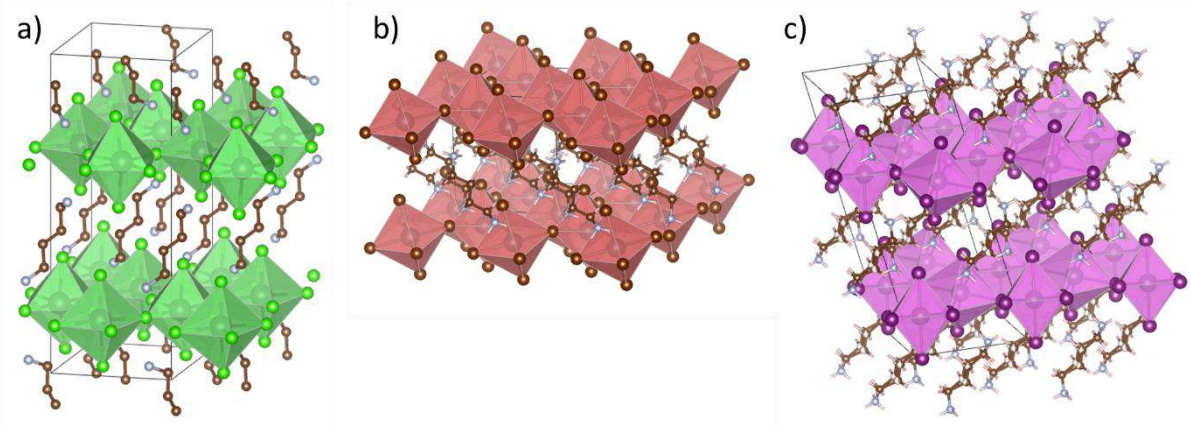

Figure 24. Hybrid crystal models $(C_4)DAPbX_4$: X=Cl (a), X=Br (b), X=I (c).

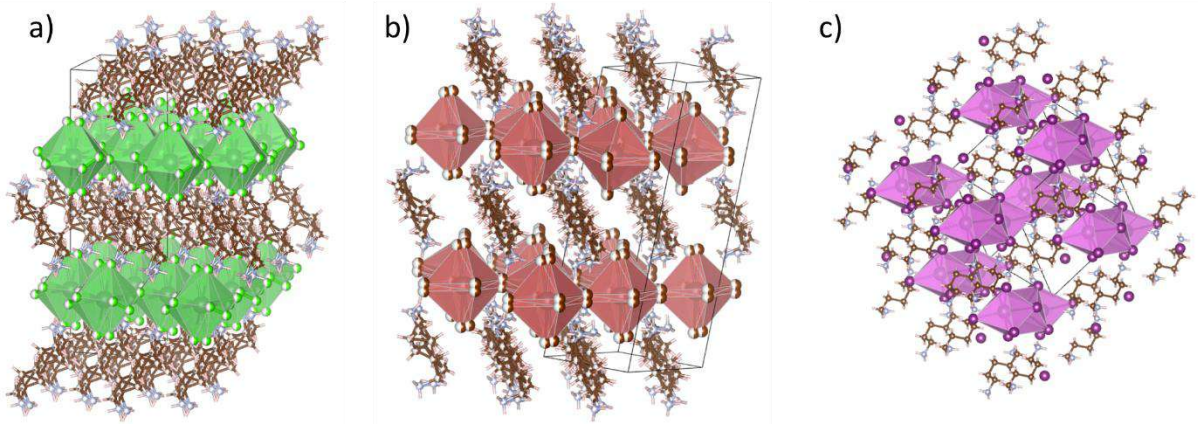

Figure 6. Hybrid crystal models $(C_5)DAPbX_4$: X=Cl (a), X=Br (b), X=I (c).

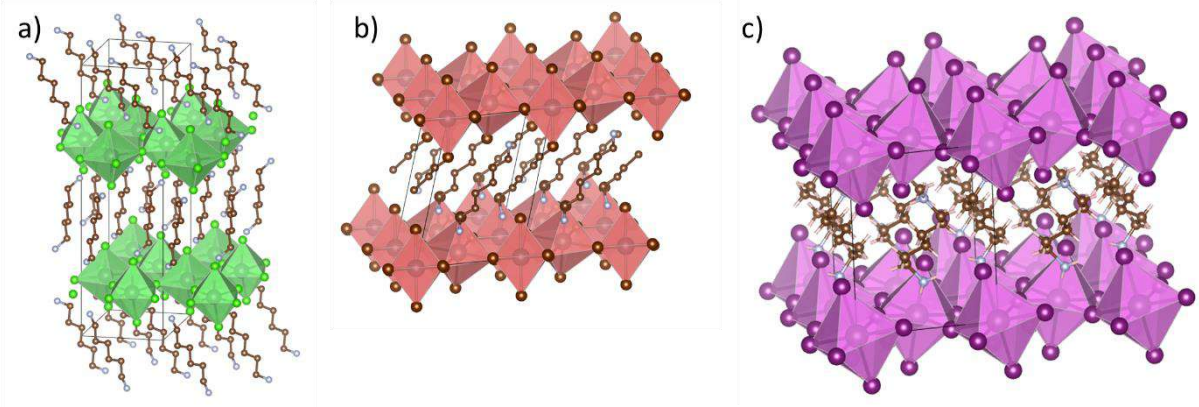

Figure 26. Hybrid crystal models $(C_6)DAPbX_4$: X=Cl (a), X=Br (b), X=I (c).

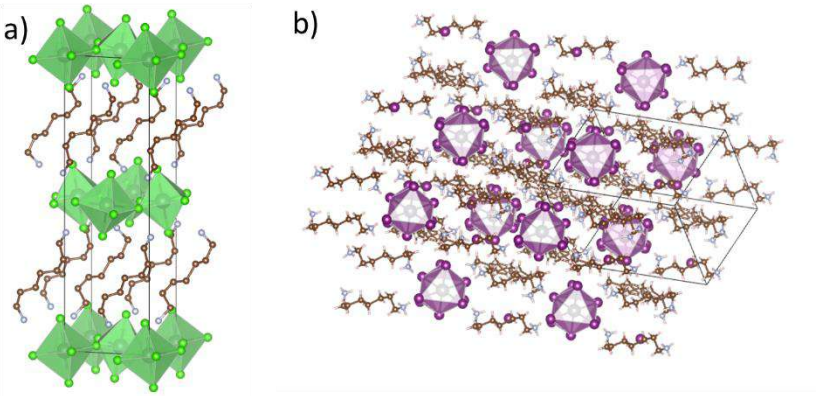

Figure 27. Hybrid crystal models $(C_7)DAPbX_4$: X=Cl (a), X=I (b).

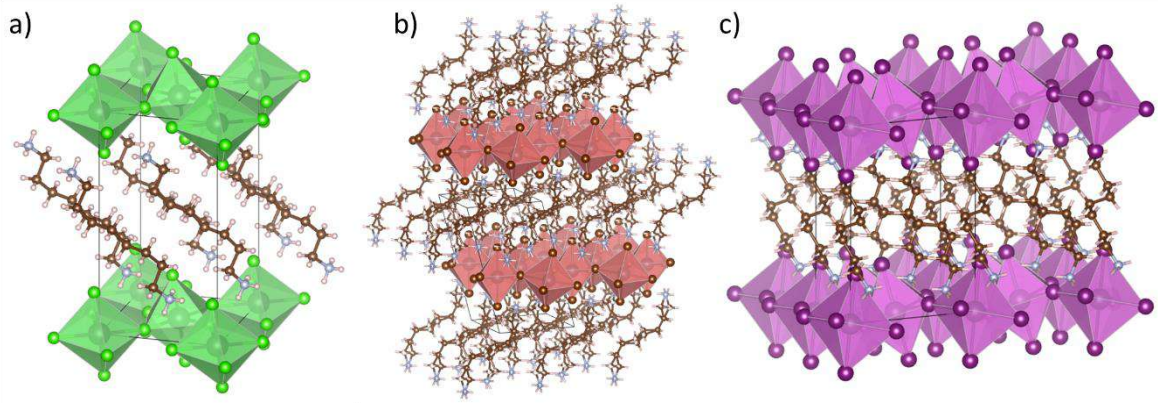

Figure 28. Hybrid crystal models $(C_8)DAPbX_4$: X=Cl (a), X=Br (b), X=I (c).

It can be seen that in all cases, the formation of two-dimensional crystals occurs with the exception of $(C_5)DAPbI_4$ (one-dimensional structure) и $(C_7)DAPbI_4$ (zero-dimensional structure). Thus, the halogen and the parity of the carbon skeleton of alkanediamines in the structure of hybrid crystals determine its dimension [59].

The distance between the planes formed by lead atoms of inorganic octahedra can be measured by the position of the main reflex of powder diffractograms. Figure 29 shows how the distance between the inorganic layers varies depending on the number of CH_2 groups in the organic cation for hybrid crystals based on various halogens.

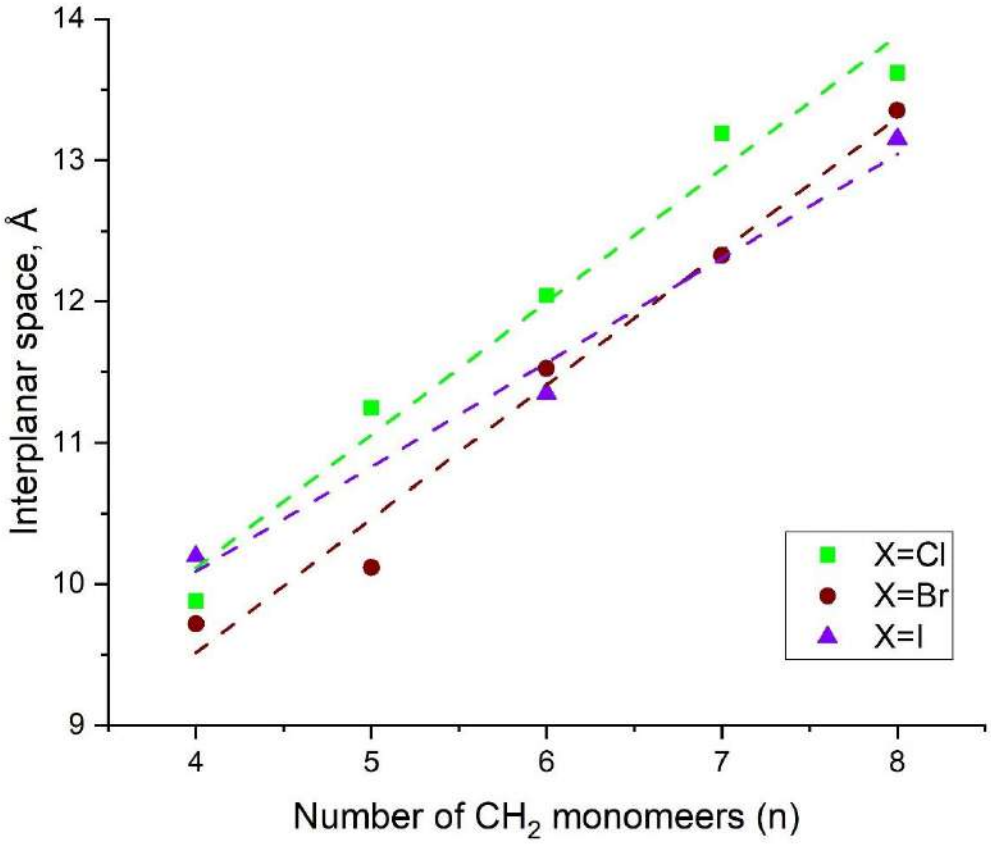

Figure 7. Dependence of the distance between the inorganic layers on the number of monomers in the organic cation.

It can be seen that as the length of the carbon skeleton of an organic cation increases, a proportional increase in the distance between the inorganic layers is observed, and in the case of iodide crystals such an increase occurs more slowly than in the case of bromide or chloride structures.

In general, the structure of hybrid crystals largely determines their optical and electronic properties. Therefore, for the purposes of this study, it is important to analyze how the type of anion and the length of the organic cation affect the various structural properties of hybrid crystals.

In inorganic salts, individual $PbHal_6$ octahedra can be connected to each other by common nodes, common edges, or common faces. Also, the layers of inorganic octahedra can be positioned parallel to each other without displacement, forming Dion-Jacobson (DJ) structures, as shown in Figure 30 a, and can be shifted by ½ octahedron width, forming Ruddelsden-Popper (RP) structures, as shown in Figure 30b

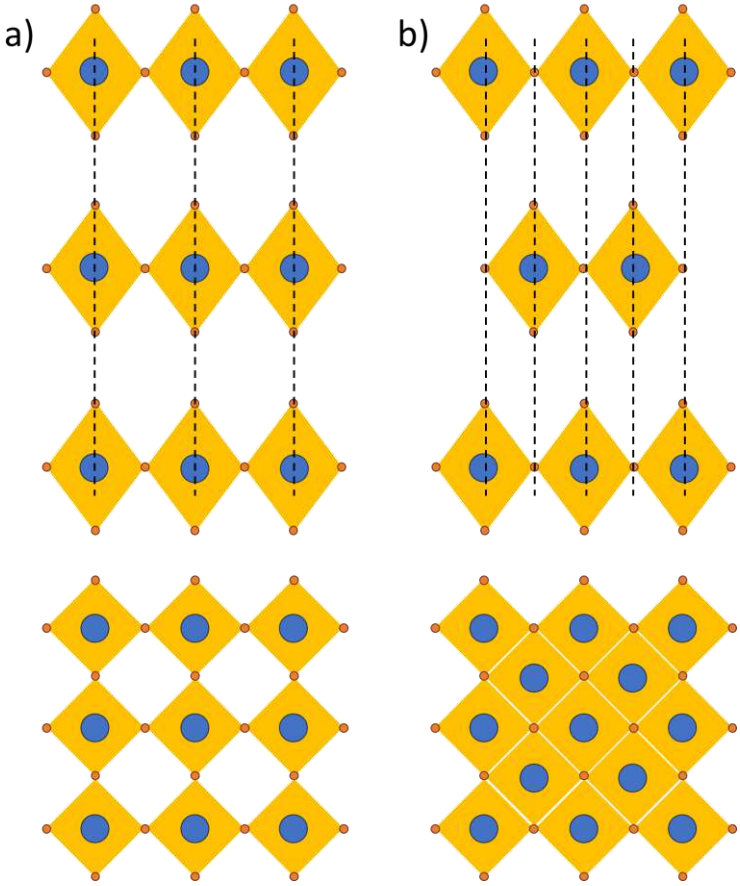

Figure 30. Options for the arrangement of layers of inorganic octahedra relative to each other.

If we analyze the structures of hybrid compounds based on lead halides and a homological series of diamines of the form $[H_3N\text{-}(CH_2)_n\text{-}NH_3]PbX_4$, depending on the length of the organic chain and the halogen, we can conclude that octahedra are connected by common nodes in all two-dimensional crystals. In a zero-dimensional crystal $(C_7)DAPbI_4$ three octahedra are connected by common faces, forming an isolated trimer. In a one-dimensional crystal $(C_5)DAPbI_4$ there are two types of octahedron connections: three octahedra are connected by common faces, forming trimers that are interconnected by common edges in an endless ribbon.

Table 2 shows how the halogen and the length of the organic cation affect the displacement of the layers of inorganic octahedra relative to each other. It can be seen that the parity of the hydrocarbon skeleton of alkanediamines in chloride, bromide and iodide crystals manifests itself in different ways. If for iodide this manifests itself in a change in dimension (as described above), then in chloride and bromide it manifests itself in the displacement of inorganic layers relative to each other: for even organic cations, the layers are located on top of each other without displacement, forming a structural (as in Figure 30a), and for odd ones they are shifted by half of the lateral the size of the octahedron, forming the RP structure (as in Figure 30b) [59].

Table 2. Displacement of inorganic layers relative to each other in the structure of hybrid compounds based on lead halides of the type $(C_n)DAPbX_4$ (X=Cl, Br, I).

Composition	Displacement of the octahedra of the adjacent layer		
	X=Cl	X=Br	X=I
$(C_4)DAPbX_4$	DJ (0;0)	DJ (0;0)	RP (½;½)
$(C_5)DAPbX_4$	RP (½;½)	RP (½;½)	-
$(C_6)DAPbX_4$	DJ (0;0)	DJ (0;0)	DJ (0;0)
$(C_7)DAPbX_4$	RP (½;½)	???	-
$(C_8)DAPbX_4$	DJ (0;0)	DJ (0;0)	DJ (0;0)

Table legend: "???" - there is no structure for analysis; "-" - not applicable.

Thus, the parity of the carbon skeleton of the organic cation, together with the type of anion, affect the structure of the resulting hybrid crystal.

In principle, the effect of zigzag changes in the properties of alkanes depending on their parity of their carbon skeleton has been known for a long time and has been called the "odd-even effect" [46]. In recent work [47] It is shown that the parity of alkanes is directly related to the density of their packing into the crystal during crystallization and even alkanes have a denser packing than odd ones.

In our case, at the ends of the carbon skeleton there are amino groups that play an important structure-forming role in the formation of a hybrid crystal due to the formation of N-H...Pb bonds. Thus, in the case of even carbon skeleton of diaminoalkanes, the inorganic layers of octahedra are arranged on top of each other without displacement as shown in Figure 30a, and in the case of odd ones – with a displacement of ½ octahedron, as shown in Figure 30b.

In other words, it can be said that using the example of hybrid crystals based on lead chlorides and bromides and a homologous series of diamines, the manifestation of the parity-odd effect of the carbon skeleton of an organic cation in hybrid two-dimensional crystals was demonstrated for the first time.

For iodide crystals, the parity-odd effect of the carbon skeleton of the organic cation manifests itself in a different way - in a decrease in dimension. Apparently, the reason for this is that iodide has a much larger atomic radius compared to other halogens. Another feature of iodide structures based on even organic cations is that if, with sufficiently short organic cations (see, (C_4)DAPbI4 in Table 2) the layers of inorganic octahedra are displaced relative to each other, then when magnified (see, (C_6)DAPbI4 and (C_8)DAPbI4 in Table 2) the layers are placed on top of each other without displacement. This is probably due to the fact that longer organic cations have a greater degree of freedom than short ones.

Figure 30 shows the cases of ideal octahedra forming ideal layers: the central atoms are located exactly in the center of the octahedra, the octahedra themselves are symmetrical and not deformed, and they are connected to each other at an angle of 180^0.

In real crystals, there is often a disordered inorganic sublattice, the variants of which are shown in Figure 31. Thus, octahedra can connect to each other at an angle other than 180^0 (see Figure 31a). To characterize this type of disorder, an angle φ can be introduced between the inorganic cations of neighboring octahedra through the anion connecting them. The more this angle differs from 180^0, the greater the degree of disorder the crystal lattice demonstrates.

Other types of disorderliness will characterize the octahedra themselves, rather than their connection.

In an ideal octahedron, the central atom should be centered, respectively, the angles between all the anions located at the vertices of the octahedra, measured through the central atom, should be 90^0. In real crystals, the displacement of the central atom is possible (see Figure 31b), which will lead to the angles being different from 90^0. This

type of disordering of the crystal lattice is usually [48] characterized by the value σ_{oct}^2, determined by the formula:

$$\sigma_{oct}^2 = \frac{1}{12}\sum_{i=1}^{i=12}(\alpha_i - 90)^2, \quad (1)$$

where α_i – i the angle X-Pb-X in each octahedron.

If there are several unique octahedra in the unit cell, the value σ_{oct}^2 is calculated for each of them, after which it is averaged.

Another type of disorder is associated with the deformation of the octahedra themselves (see Figure 31c). As it is easy to see, in this case the angles of X-Pb-X will be straight, but the distance between the central atom and the vertices of the octahedra will be different. This type of disordering of the crystal lattice is usually [48] characterized by the value σ_{oct}^2, determined by the formula:

$$\Delta d = \frac{1}{6}\sum_{i=1}^{i=6}\frac{(d_i - d_{av})^2}{d_i}, \quad (2)$$

where d_i – the length of the i-th Pb-X bond, d_{av} – the average bond length in an octahedron.

If there are several unique octahedra in the unit cell, the values d_i и d_{av} are calculated for each of them, after which the average is calculated.

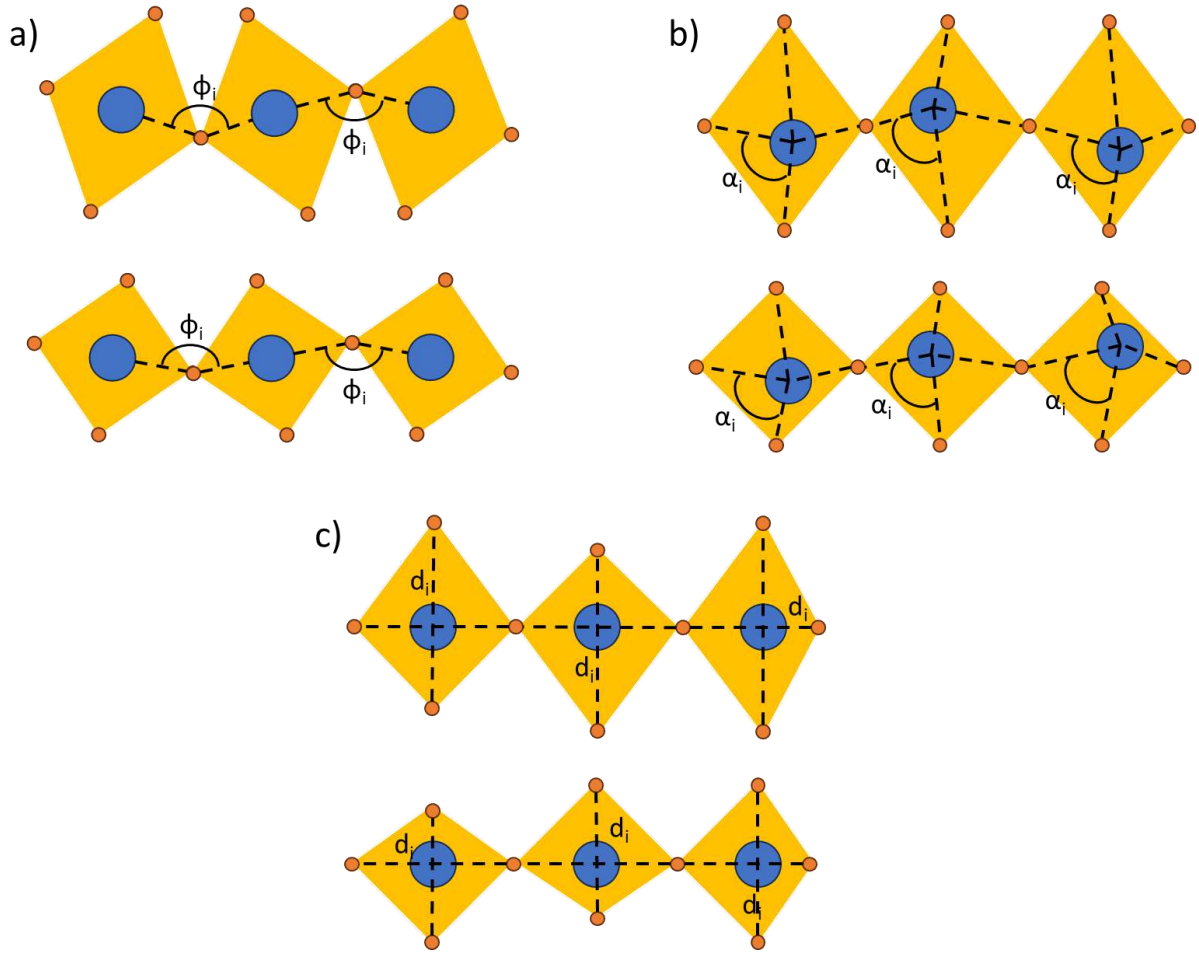

Figure 31. Variants of disordered inorganic octahedra in real crystals.

The analysis of such disorderings of real hybrid crystals is very important, since they affect, among other things, the optical properties of materials. In [49] It is shown that the inclination of the octahedra relative to each other (angle φ) affects the band gap of the perovskites, whereas the deformation of the octahedra themselves (values σ_{oct}^2 и Δd) affects the presence of broadband luminescence in the crystal [48].

Table 3 shows the disordered parameters of the inorganic sublattice of various hybrid compounds based on lead halides of the type studied $(C_n)DAPbX_4$.

Table 3. Disordered parameters of the inorganic sublattice of hybrid compounds based on lead halides type $(C_n)DAPbX_4$.

Composition	d_{av}, Å	$\Delta d*10^{-3}$, Å^2	σ^2_{oct}, $^{0\,2}$	φ_{av}, ^{0}
$(C_4)DAPbCl_4$	2,88	12,42	28,85	150,9
$(C_5)DAPbCl_4$	2,86	2,685	231,62	145,83
$(C_6)DAPbCl_4$	2,87	10,18	33,19	149,41
$(C_7)DAPbCl_4$	2,85	5,07	5,58	145,24
$(C_8)DAPbCl_4$	2,87	3,83	15,35	146,62
$(C_4)DAPbBr_4$	3,0	5,225	8,01	148,36
$(C_5)DAPbBr_4$	2,99	9,53	31,52	150,53
$(C_6)DAPbBr_4$	3,05	6,56	40,27	149,29
$(C_7)DAPbBr_4$	-	-	-	-
$(C_8)DAPbBr_4$	2,99	0,73	3,59	148,21
$(C_4)DAPbI_4$	3,2	1,99	3,82	147,18
$(C_5)DAPbI_4$	3,23	17,96	22,22	77,85
$(C_6)DAPbI_4$	3,21	5,29	2,97	148,47
$(C_7)DAPbI_4$	3,24	20,965	34,39	78,16
$(C_8)DAPbI_4$	3,2	1,79	7,18	147,62

The average length of the lead–halogen bond inside octahedra increases in the chloride – bromide – iodide series: if for chloride crystals the average bond length is 2.85 – 2.88 Å, then for bromide crystals it is from 2.99 to 3.05 Å, and for iodide crystals it is from 3.2 to 3.24 Å. At the same time, there is no correlation between the average bond length in the octahedron and the size or parity of the organic cation.

The displacement of the central atom in the σ^2_{oct}, octahedra, determined by the formula (1), shows a significant disorder of the corresponding type in the crystal $(C_5)DAPbCl_4$.

It was previously shown that chloride and bromide hybrid crystals, in the structure of which there is an organic cation with an odd number of carbon atoms, form inorganic layers shifted relative to each other by ½ the width of the octahedron in the x and y directions. If we exclude them from consideration, the correlation between σ^2_{oct} and the inclination of the octahedra relative to each other ($180-\varphi_{av}$), shown in Figure 32, looks indicative.In this figure, the value $180-\varphi_{av}$ is used to show the degree of imperfection of the crystal lattice: the more the cleavage between the octahedra differs from 180^0, the more imperfect crystals are formed.

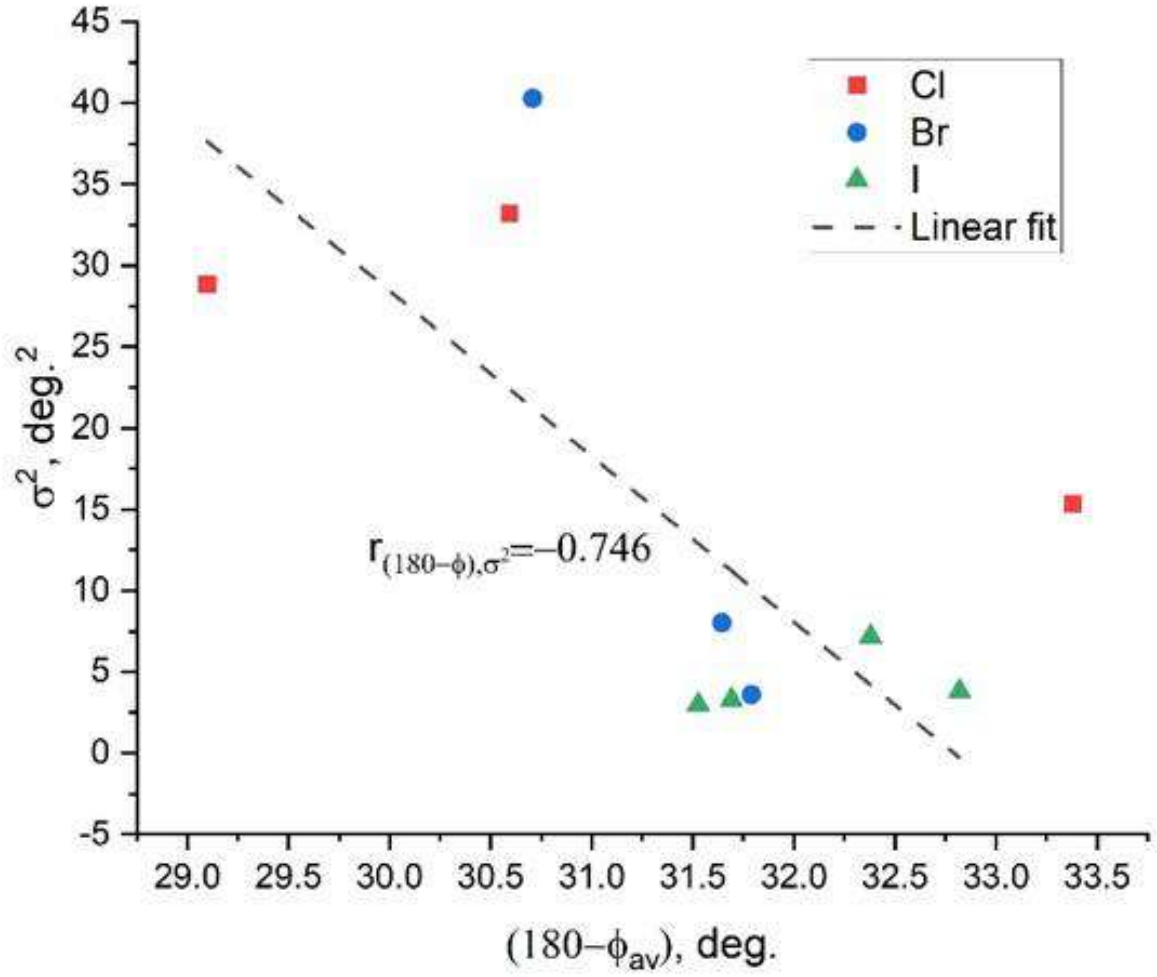

Figure 8. Correlation between the disorder inside the σ^2_{oct} octahedra and the inclination of the octahedra relative to each other (180-φ_{av}) for hybrid crystals of different cationic and anionic compositions

The application of correlation analysis methods to the data shown in Table 3 and Figure 32 makes it possible to determine the Pearson coefficient and, based on it, the presence and strength of correlation between two types of octahedral disorder. The Pearson coefficient is -0.746, which suggests that there is a strong inverse correlation between two types of octahedron distortion: internal, characterized by the parameter σ^2_{oct} and external, characterized by the parameter φ_{av}.

That is, during the formation of the studied hybrid crystals, two competing processes of disordering the inorganic sublattice are observed, between which a strong correlation is found. This confirms the assumptions made earlier [50] by studying a narrower sample of similar hybrid crystals.

3.2 Quantum chemical calculations of hybrid compounds based on lead halides and homologous series of diamines of the form $[H_3N\text{-}(CH_2)_n\text{-}NH_3]PbX_4$ (n=4-8, X=Cl, Br, I)

The data obtained by X-ray phase analysis, as well as previously published data on the elementary cells of the hybrid crystals under study, made it possible to conduct their quantum chemical modeling using the theory of the electron density functional (TFEP), the results of which are presented below in Figure 33 - Figure 46 [59].

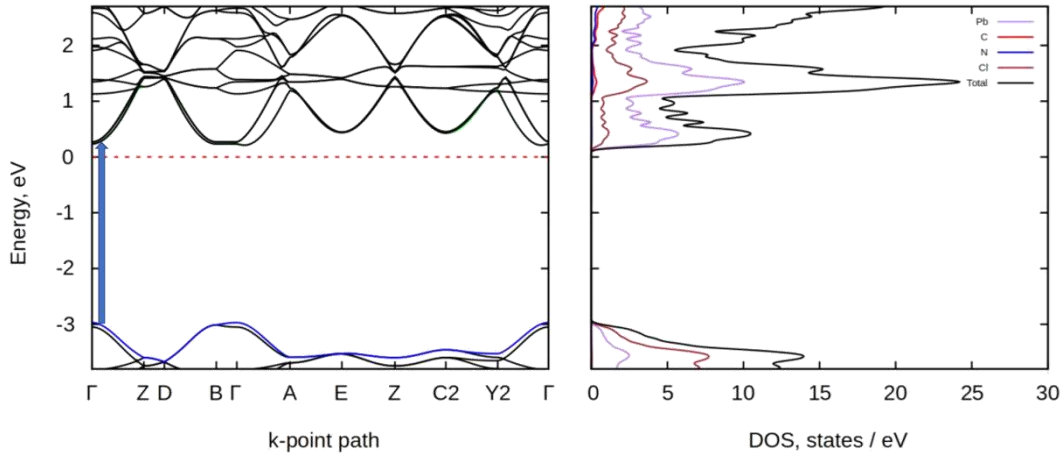

Figure 33. Electronic band structure (left) and density of states (right) for hybrid crystal $(C_4)DAPbCl_4$. The blue arrow indicates the transition between the ceiling of the valence band and the bottom of the conduction band.

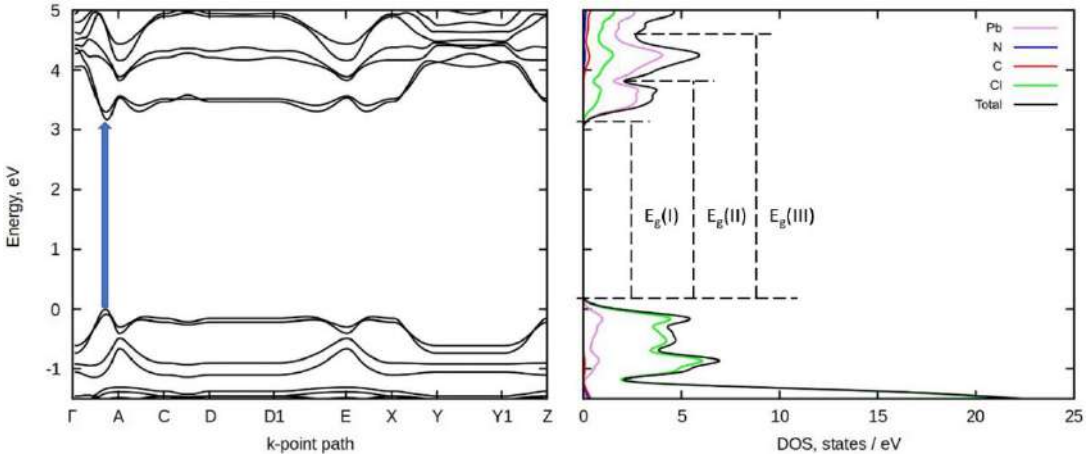

Figure 34. Electronic band structure (left) and density of states (right) for hybrid crystal $(C_5)DAPbCl_4$. The blue arrow indicates the transition between the ceiling of the valence band and the bottom of the conduction band.

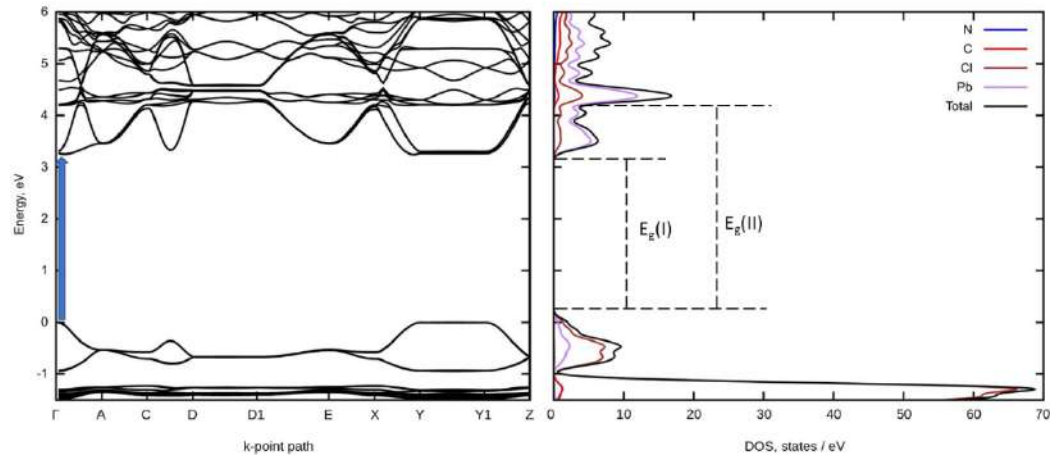

Figure 35. Electronic band structure (left) and density of states (right) for hybrid crystal $(C_6)DAPbCl_4$. The blue and orange arrows indicate the transition between the ceiling of the valence band and the bottom of the conduction band.

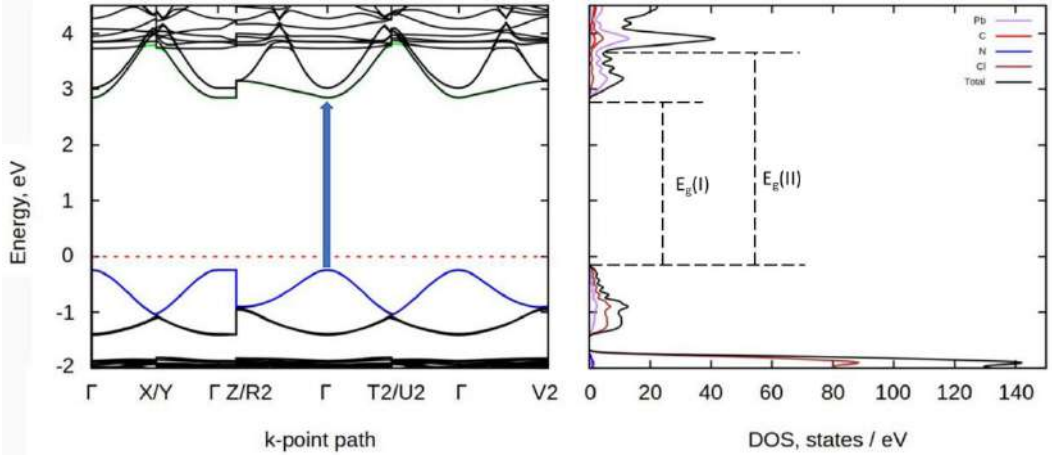

Figure 36. Electronic band structure (left) and density of states (right) for hybrid crystal $(C_7)DAPbCl_4$. The blue arrow indicates the transition between the ceiling of the valence band and the bottom of the conduction band.

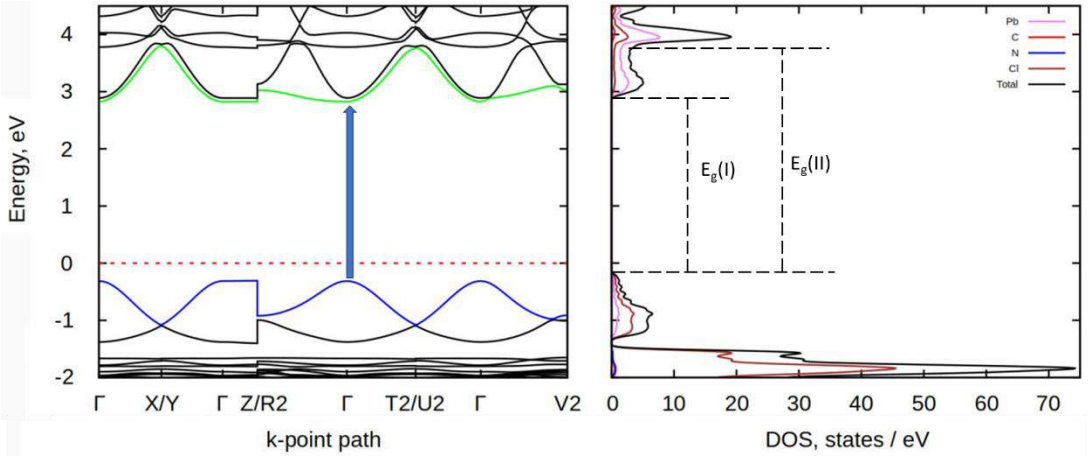

Figure 37. Electronic band structure (left) and density of states (right) for hybrid crystal $(C_8)DAPbCl_4$. The blue arrow indicates the transition between the ceiling of the valence band and the bottom of the conduction band.

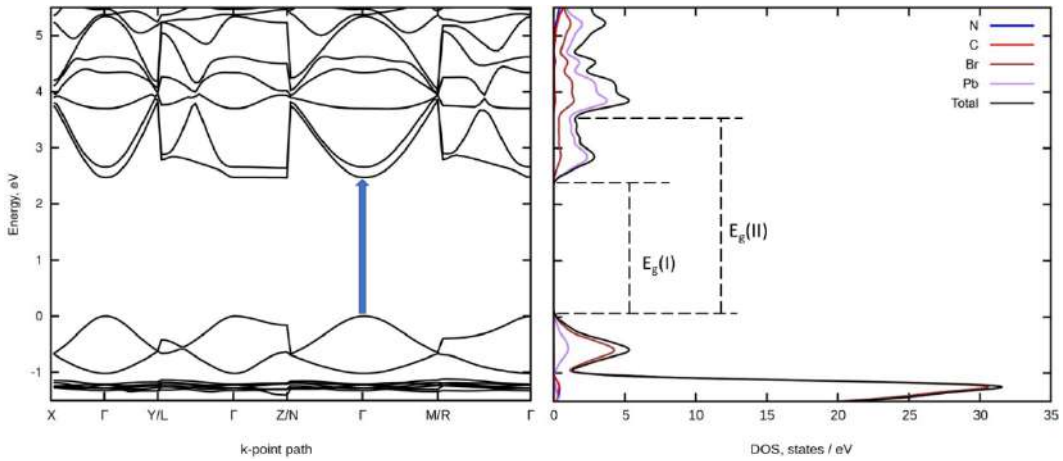

Figure 38. Electronic band structure (left) and density of states (right) for hybrid perovskite $(C_4)DAPbBr_4$. The blue arrow indicates the transition between the ceiling of the valence band and the bottom of the conduction band.

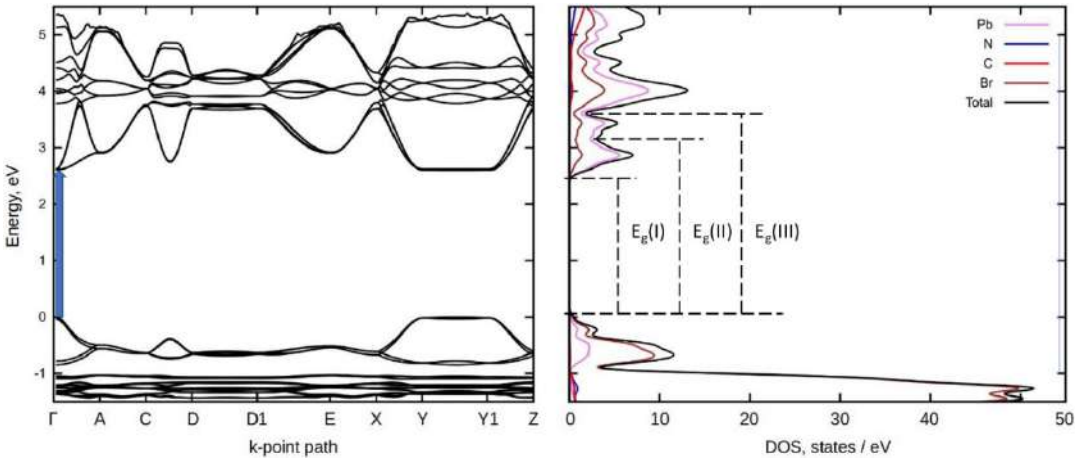

Figure 39. Electronic band structure (left) and density of states (right) for hybrid crystal $(C_5)DAPbBr_4$. The blue arrow indicates the transition between the ceiling of the valence band and the bottom of the conduction band.

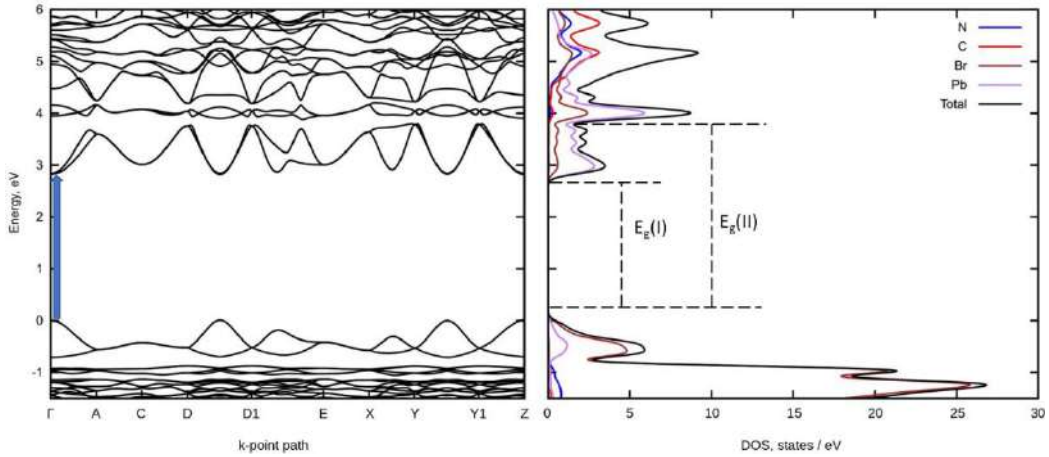

Figure 9. Electronic band structure (left) and density of states (right) for hybrid crystal $(C_6)DAPbBr_4$. The blue arrow indicates the transition between the ceiling of the valence band and the bottom of the conduction band.

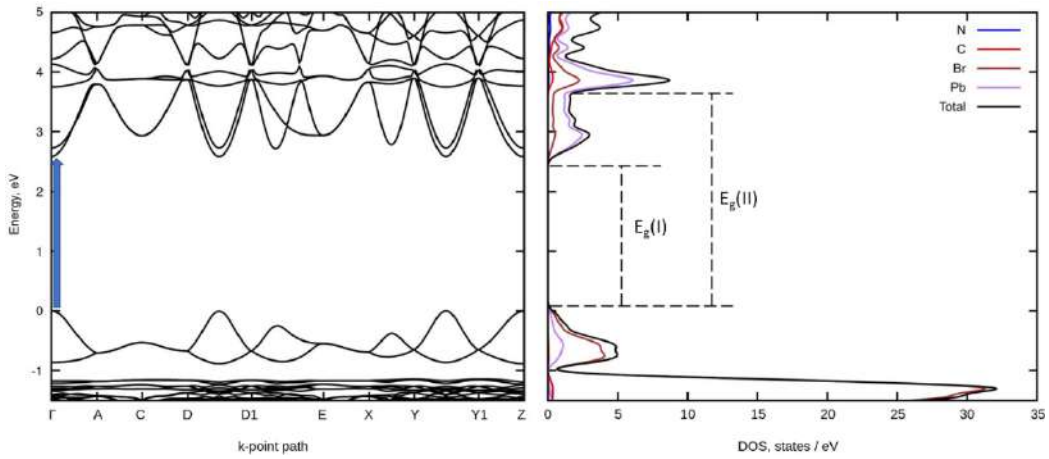

Figure 41. Electronic band structure (left) and density of states (right) for hybrid crystal $(C_8)DAPbBr_4$. The blue and orange arrows indicate the transition between the ceiling of the valence band and the bottom of the conduction band.

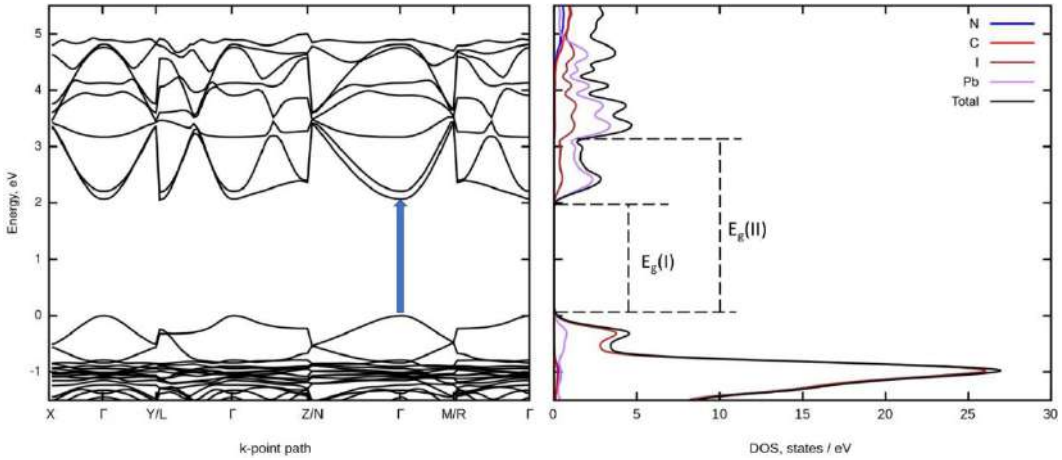

Figure 42. Electronic band structure (left) and density of states (right) for hybrid crystal $(C_4)DAPbI_4$. The blue arrow indicates the transition between the ceiling of the valence band and the bottom of the conduction band.

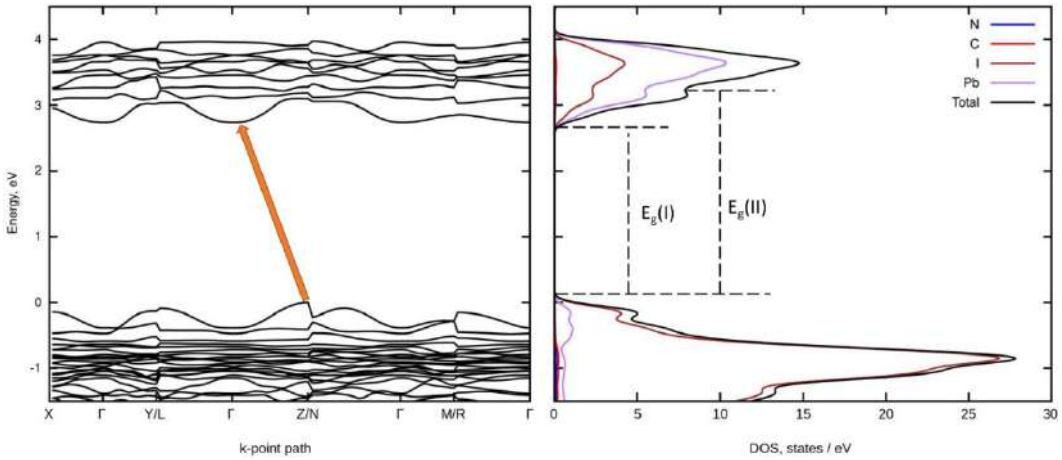

Figure 43. Electronic band structure (left) and density of states (right) for hybrid crystal $(C_5)DAPbI_4$. The orange arrow indicates the transition between the ceiling of the valence band and the bottom of the conduction band.

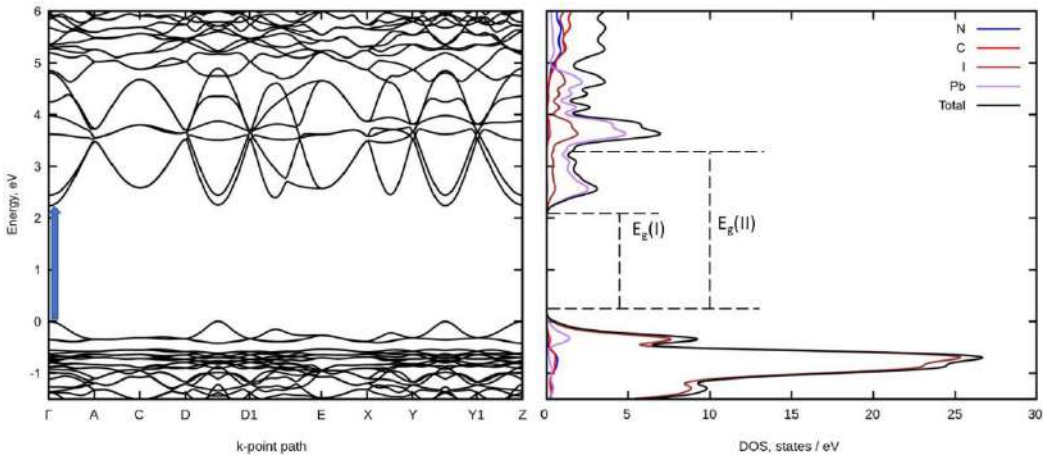

Figure 44. Electronic band structure (left) and density of states (right) for hybrid crystal $(C_6)DAPbI_4$. The blue arrow indicates the transition between the ceiling of the valence band and the bottom of the conduction band.

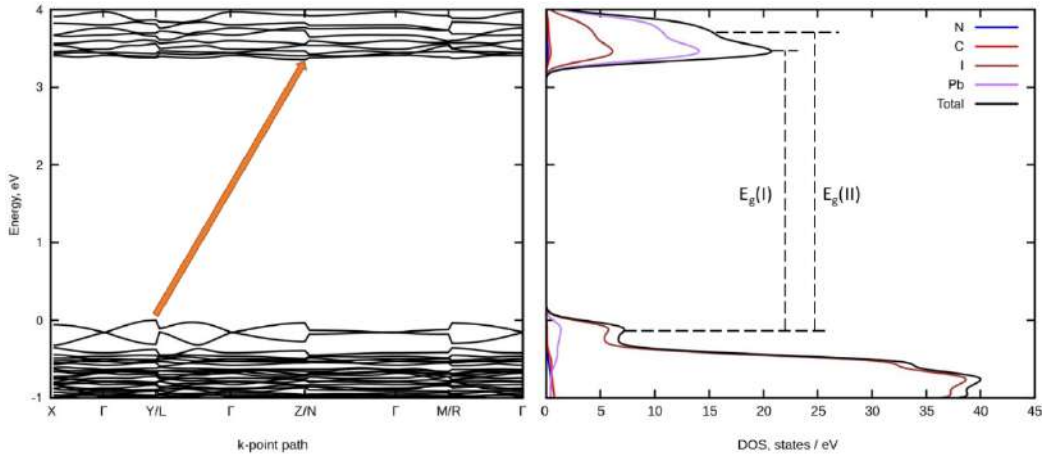

Figure 45. Electronic band structure (left) and density of states (right) for hybrid crystal $(C_7)DAPbI_4$. The orange arrow indicates the transition between the ceiling of the valence band and the bottom of the conduction band.

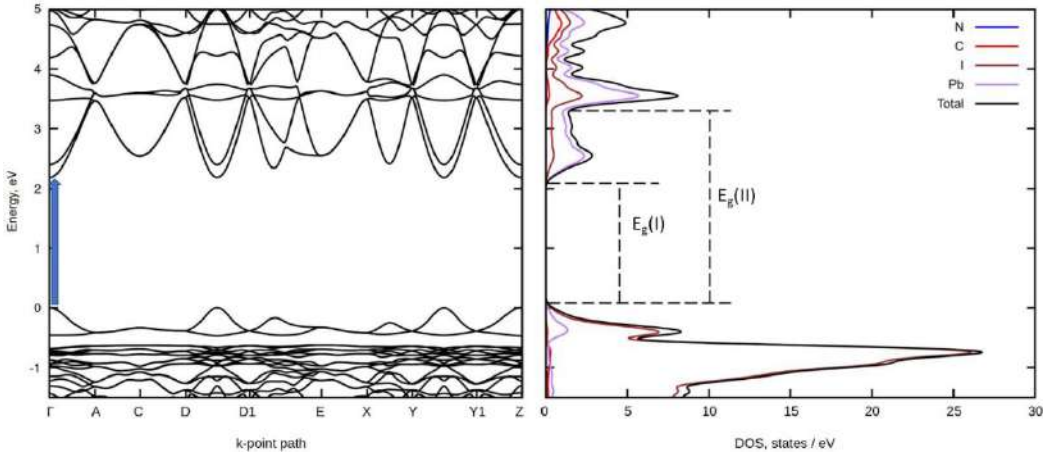

Figure 46. Electronic band structure (left) and density of states (right) for hybrid perovskite $(C_8)DAPbI_4$. The blue arrow indicates the transition between the ceiling of the valence band and the bottom of the conduction band.

For ease of analysis, the basic information and the type of transition in each particular semiconductor and the corresponding value of the band gap are summarized in Table 4.

It can be seen from the calculations that all two-dimensional crystals (all chloride and bromide, as well as iodide with an even number of carbon atoms in the structure of an organic cation) are straight-band semiconductors, transitions from the valence band to the conduction band in which mainly occur at the point Γ of the Brillouin zone.

In turn, iodide crystals with an odd number of carbon atoms in the structure of an organic cation forming one-dimensional and zero-dimensional structures are non-direct band semiconductors, while this is a conditional concept for zero-dimensional crystals.

Table 4. Types and characteristics of transitions for various hybrid crystals of the type $(C_n)DAPbX_4$ (X=Cl, Br, I; n=4-8).

Composition	Type of transition	Point of the Brillouin zone	Calculated band gap Eg, eV
$(C_4)DAPbCl_4$	Direct allowed	Γ → Γ	3,20
$(C_5)DAPbCl_4$	Direct allowed	Γ/A→ Γ/A	3,17
$(C_6)DAPbCl_4$	Direct allowed	Γ → Γ	3,24
$(C_7)DAPbCl_4$	Direct allowed	Γ → Γ	3,08
$(C_8)DAPbCl_4$	Direct allowed	Γ → Γ	3,05
$(C_4)DAPbBr_4$	Direct allowed	Γ → Γ	2,47
$(C_5)DAPbBr_4$	Direct allowed	Γ → Γ	2,60
$(C_6)DAPbBr_4$	Direct allowed	Γ → Γ	2,82
$(C_7)DAPbBr_4$	No	No	No
$(C_8)DAPbBr_4$	Direct allowed	Γ → Γ	2,59
$(C_4)DAPbI_4$	Direct allowed	Γ → Γ	2,05
$(C_5)DAPbI_4$	Direct allowed	Z/N→ Γ	2,73
$(C_6)DAPbI_4$	Direct allowed	Γ → Γ	2,23
$(C_7)DAPbI_4$	Direct allowed	Y/L→Z/N	3,35
$(C_8)DAPbI_4$	Direct allowed	Γ → Γ	2,18

Table legend: "No" - there is no structure for calculation.

If we turn to the analysis of the density of states (the right part of Figure 33 - Figure 46), it can be seen that there are at least two regions in the conduction band in which the density of states is maximum. The first region is adjacent to the bottom of the conduction band and is composed mainly of electronic orbitals of the B (lead)

cation. Electron transitions into this region from the ceiling of the valence band ($VB_m \rightarrow CB_m$) apparently, they form the edge of the fundamental absorption and correspond to the optical width of the band gap indicated in figures $E_g(I)$. The second region begins about 1 eV above the first and is designated as $E_g(II)$. Transitions correspond to it $VB_m \rightarrow CB+1$.

3.3 Optical properties of hybrid compounds based on lead halides and a homologous series of diamines of the form $[H_3N\text{-}(CH_2)_n\text{-}NH_3]PbX_4$ (n=4-8, X=Cl, Br, I)

3.3.1 Diffuse reflection spectroscopy

Diffuse reflection spectra of hybrid perovskites $(C_n)DAPbX_4$ are shown in Figure 47. All the above spectra have several common features, despite the significantly different compositions. Firstly, the area of self–absorption of chloride perovskites is maximally shifted to the blue, and iodide - to the red region, while bromide perovskites occupy an intermediate position. Secondly, for all the studied samples, local absorption maxima are present in the area of intrinsic absorption. From the differences presented in Figure 47, it should be pointed out that there is a significant absorption in its own area inherent in all iodide perovskites [59].

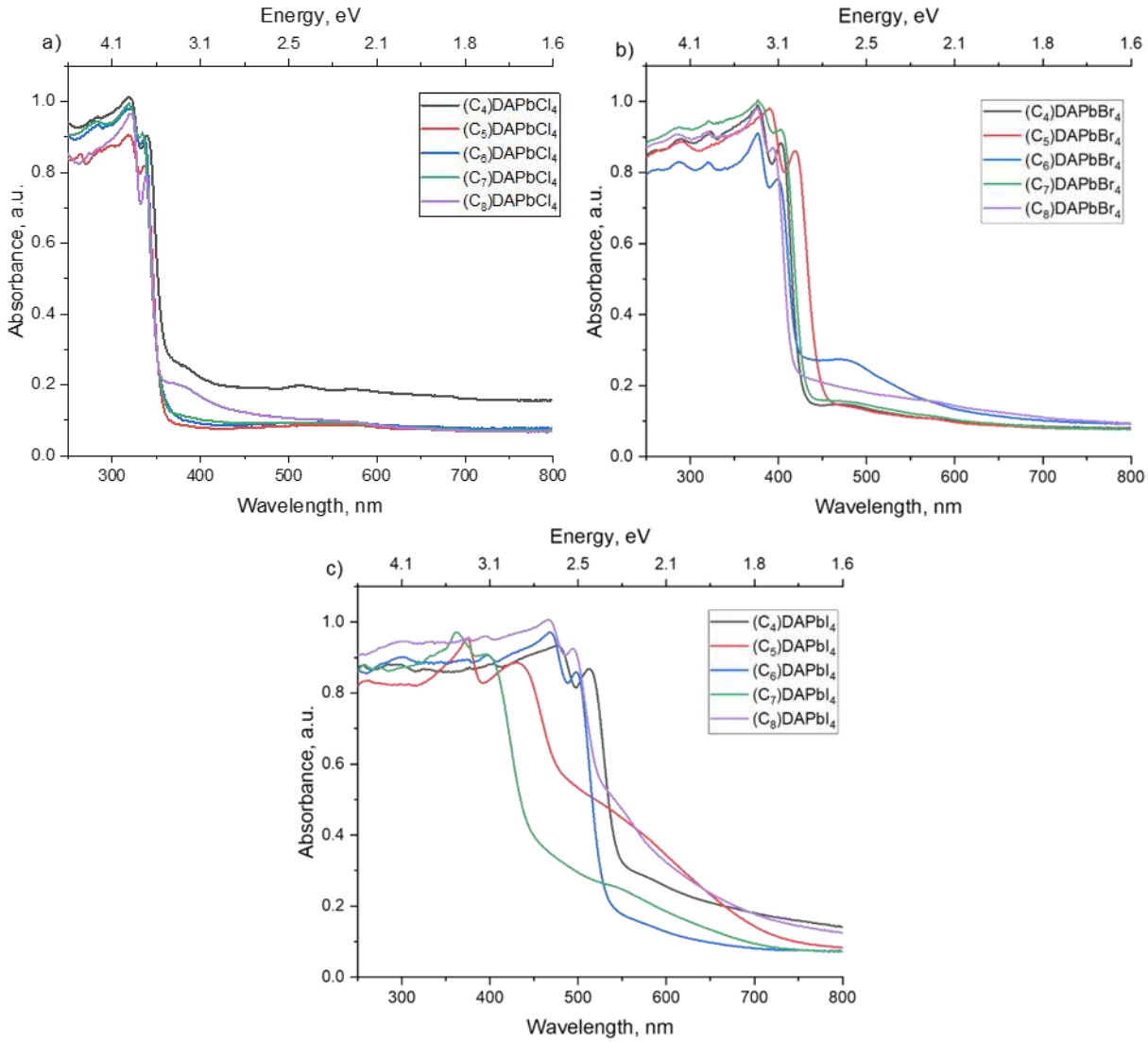

Figure 47. Diffuse reflection spectra $(C_n)DAPbCl_4$ (a), $(C_n)DAPbBr_4$ (b) и $(C_n)DAPbI_4$ (c).

To determine the optical bandgap widths of the studied hybrid compounds, the derivative method [60] was used, the results of which are shown in Figure 48.

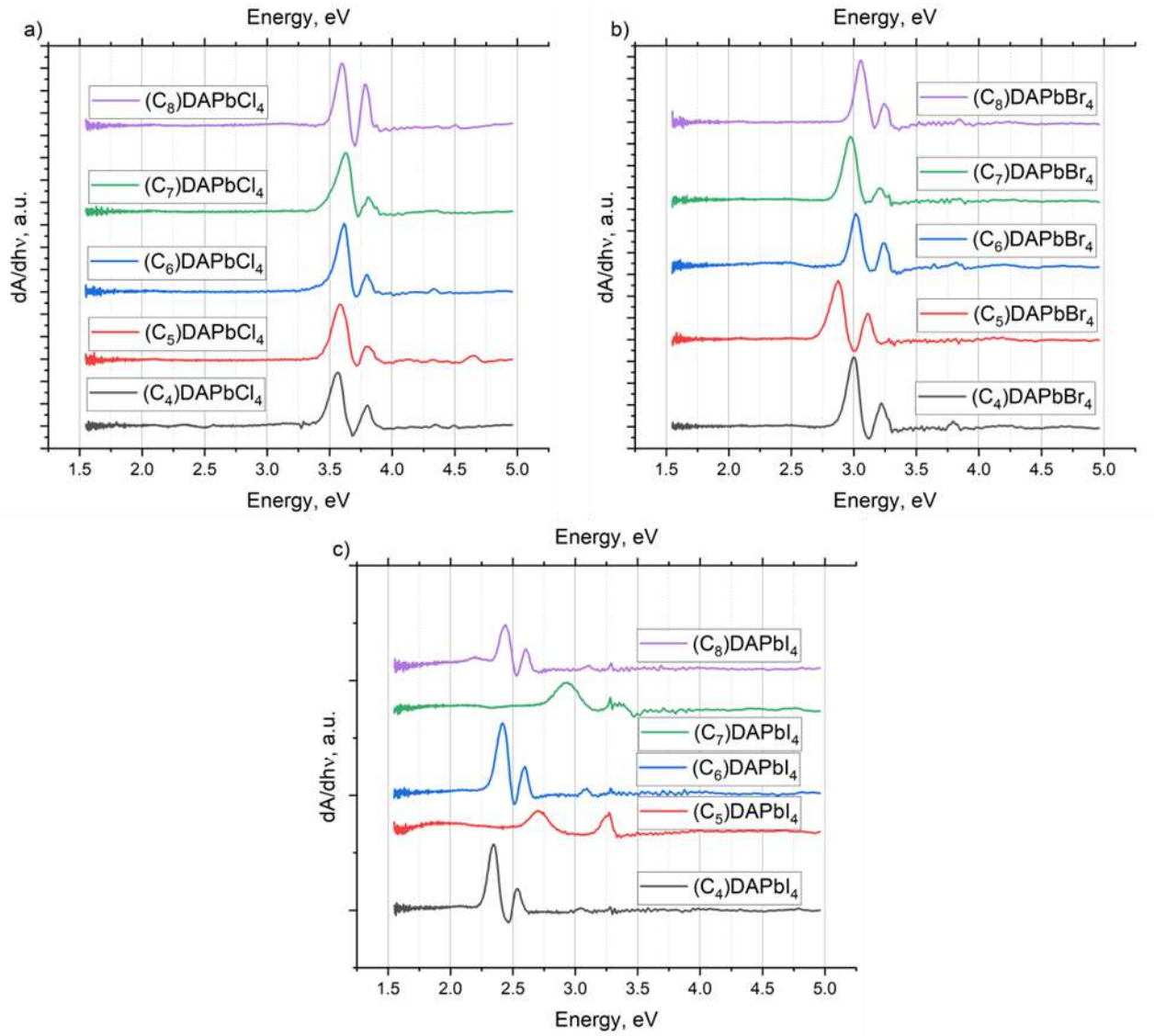

Figure 48. Approximation by the method of derivative diffuse reflection spectra of hybrid perovskites $(C_n)DAPbCl_4$ (a), $(C_n)DAPbBr_4$ (b) и $(C_n)DAPbI_4$ (c).

On the given curves, the presence of two maxima is characteristic for all hybrid perovskites studied in this work. The position of the lower-energy maximum corresponds to the optical band gap of the perovskite, and the second maximum, shifted to the region of high energies, is obviously associated with the absorption bands described above in the region of their fundamental absorption.

For the convenience of analyzing the results obtained, they are shown in Figure 49 and Table 5. In this figure and in the table, the optical band gap is indicated as $E_g(I)$, and the energy corresponding to the second maximum in Figure 48 is indicated as $E_g(II)$. The reasons for this will be explained in detail below.

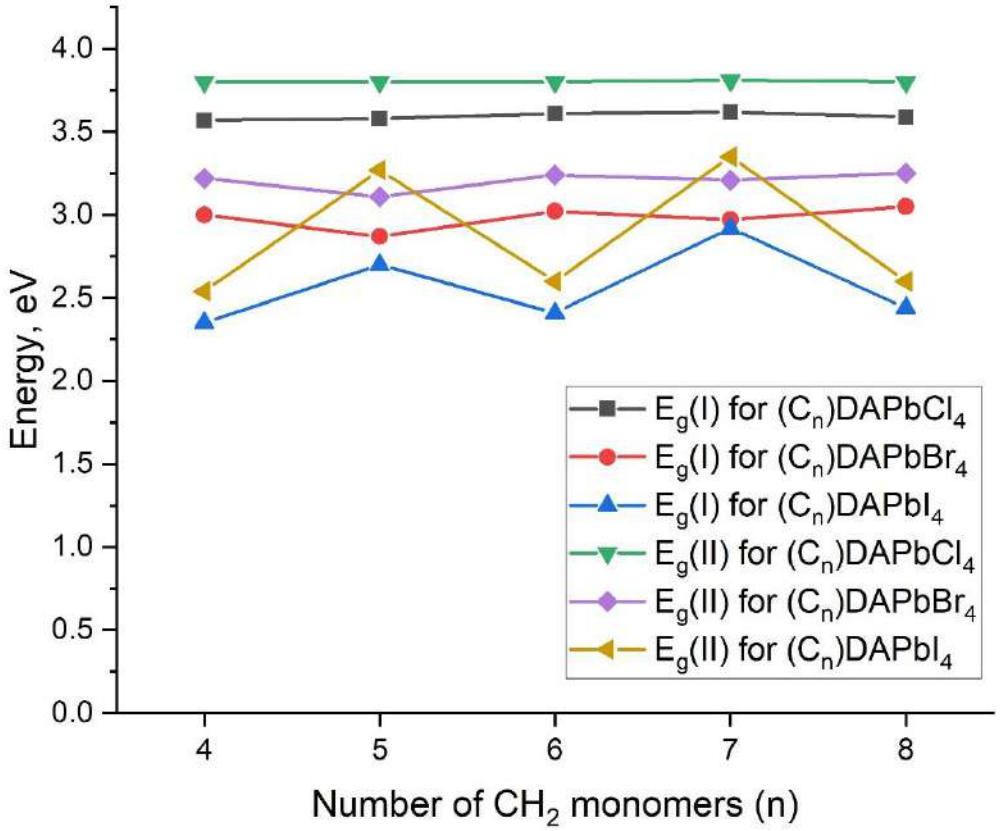

Figure 49. Dependence of the band gap width of $(C_n)DAPbX_4$ (X=Cl, Br, I) of the number of CH_2 monomers in the structure of the organic cation

Table 5. Values of optical band gap widths for various hybrid perovskites of the type $(C_n)DAPbX_4$ (X=Cl, Br, I).

Composition	E_g(I), eV			E_g(II), eV		
	X=Cl	X=Br	X=I	X=Cl	X=Br	X=I
$(C_4)DAPbX_4$	3,57	3	2,35	3,8	3,22	2,54
$(C_5)DAPbX_4$	3,58	2,87	2,7	3,8	3,11	3,27
$(C_6)DAPbX_4$	3,61	3,02	2,41	3,8	3,24	2,6
$(C_7)DAPbX_4$	3,62	2,97	2,92	3,81	3,21	3,35
$(C_8)DAPbX_4$	3,59	3,05	2,44	3,8	3,25	2,6

The patterns of dependence of the optical band gap width (E_g(I)) are traced both from the anion and from the length of the carbon chain of the organic cation.

For chloride perovskites, E_g(I) does not depend on the length of the carbon chain and is in the range of 3.57-3.62 eV.

For bromide perovskites, E_g(I) of "even" crystals (that is, those in which the organic cation has an even number of CH_2 monomers in the structure) (n=4, 6, 8) is in

the range 3-3.05 eV, whereas E_g(I) for "odd" (n=5, 7) it turns out to be slightly lower and is 2.87-2.97 eV.

The most pronounced differences due to the parity of the carbon chain of the organic cation are manifested in iodide crystals. As can be seen from Figure 49, an increase in E_g(I) is observed as the length of the carbon chain (n) increases. And just as in the case of bromide perovskites, there is a modulation of E_g(I) oscillations due to the parity of the carbon chain. However, in this case, the situation is reversed for bromide perovskites: for "even" perovskites (n=4, 6, 8), we observe a monotonous increase in E_g(I) from 2.35 eV to 2.44 eV, and for «odd» (n=5, 7), the band gap turns out to be much higher and is 2.7 eV and 2.92 eV, which is due to the influence of the quantum dimensional effect corresponding to the one-dimensional and zero-dimensional structure of these samples in comparison with the other two-dimensional ones.

If we compare the experimental values of the band gap widths (E_g(I) in Table 5) with the calculated values (Table 4), then there is a good convergence of the data: the calculated values are slightly underestimated, the difference is up to 0.5 eV, which is common when using the selected pseudopotentials.

Further, if we compare the values of E_g(II) from Table 5, we can conclude that the corresponding features of the diffuse reflection spectra, which are quite characteristic of hybrid perovskites, are due to the peculiarities of their electronic structure and correspond to transitions $VB_m \rightarrow CB+1$.

3.3.2 Luminescent properties

The low-temperature luminescence of hybrid crystals based on lead halides and a homologous series of diamines of the form $[H_3N\text{-}(CH_2)_n\text{-}NH_3]PbX_4$ was studied depending on the halogen and the length of the organic cation. The corresponding emission spectra and luminescence excitation spectra are shown in Figure 50 - Figure 62 [59].

Before proceeding to their analysis, it is necessary to clarify terminologically what terms we will use next to describe the luminescent properties of the materials under study. A free exciton (FE) is a delocalized exciton state. Its formation is manifested by a narrow band in the luminescence excitation spectrum with an energy less than the band gap width. An self-trapped exciton (STE) is an exciton that polarized the lattice, creating a local minimum of energy, and as a result localized in a certain region of the crystal. Usually, the energy change caused by the polarization of the lattice is small and the luminescence shift of such an exciton in energy relative to FE is also small. The difference between these two energies (E_{tr}) corresponds to the defect-trapping energy of the free exciton (see the notation in the inserts in Figure 50 - Figure 62):

$$E_{tr} = E_{ex} - E_{em}. \quad (3)$$

A defect-trapped exciton (DTE) is an exciton captured by a defect when one of the exciton components, an electron or a hole, is captured by the Coulomb field of the defect. Then the localization energy can be significant, which leads to a large shift in the luminescence of such an exciton with respect to FE. Since there is a wide variety of defects in a real crystal (both in type and energy), their distribution determines a wide distribution of luminescence [51]. This is typical for any luminescence associated with defects.

Figure 50 shows the spectrum of low-temperature photoluminescence for the sample $(C_4)DAPbCl_4$. The emission spectrum shows intense broadband luminescence with a maximum in the region of 553 nm. Broadband luminescence is usually identified

with the luminescence of defect-trapped excitons (DTE). At the same time, there is no narrow-band luminescence of self-trapped excitons (STE), which is possibly due to the fact that the lattice energy at a given temperature is sufficient to cause the transition of a free exciton to a state localized on the defect. Several bands can also be distinguished in the luminescence excitation spectrum. Thus, luminescence is most effectively excited by radiation with a wavelength of 315 nm, but closer to the edge of its own absorption there are two more luminescence excitation bands with maxima at 333.2 and 341.6 nm.

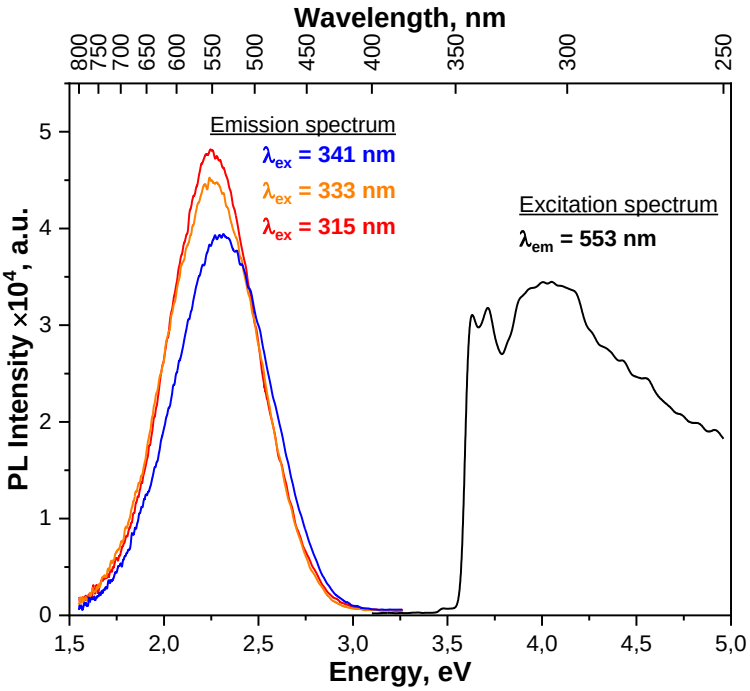

Figure 50. The spectrum of low-temperature photoluminescence $(C_4)DAPbCl_4$

If we analyze the luminescent properties of the remaining chloride-based hybrid crystals shown in Figure 51 - Figure 54, we can state that the case $(C_4)DAPbCl_4$ is typical for crystals of this series. So, for all of them, the characteristic is: the presence of broadband luminescence in the emission spectra.

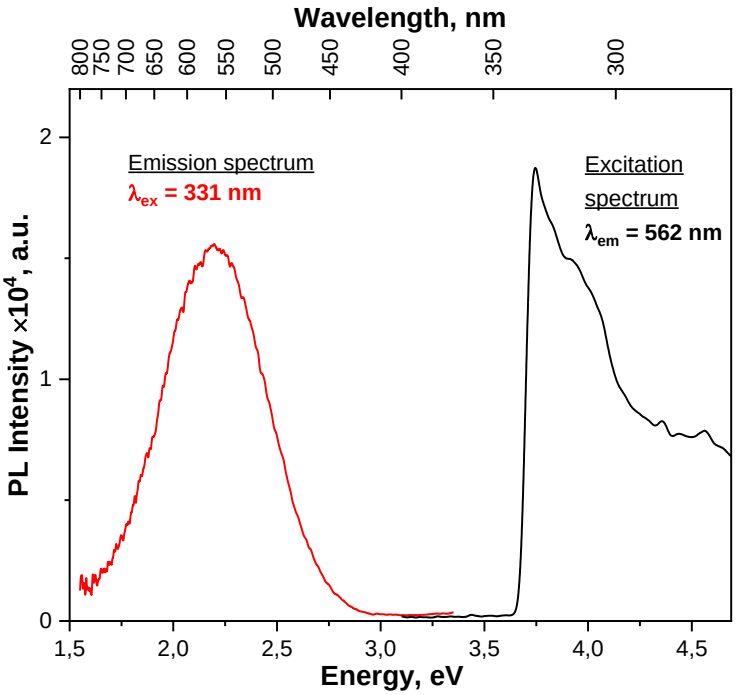

Figure 51. The spectrum of low-temperature photoluminescence $(C_5)DAPbCl_4$

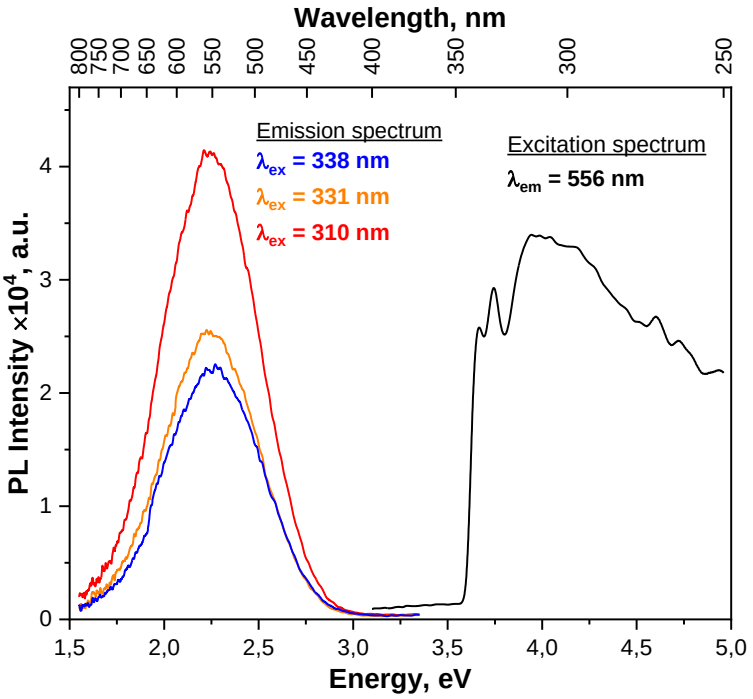

Figure 52. The spectrum of low-temperature photoluminescence $(C_6)DAPbCl_4$

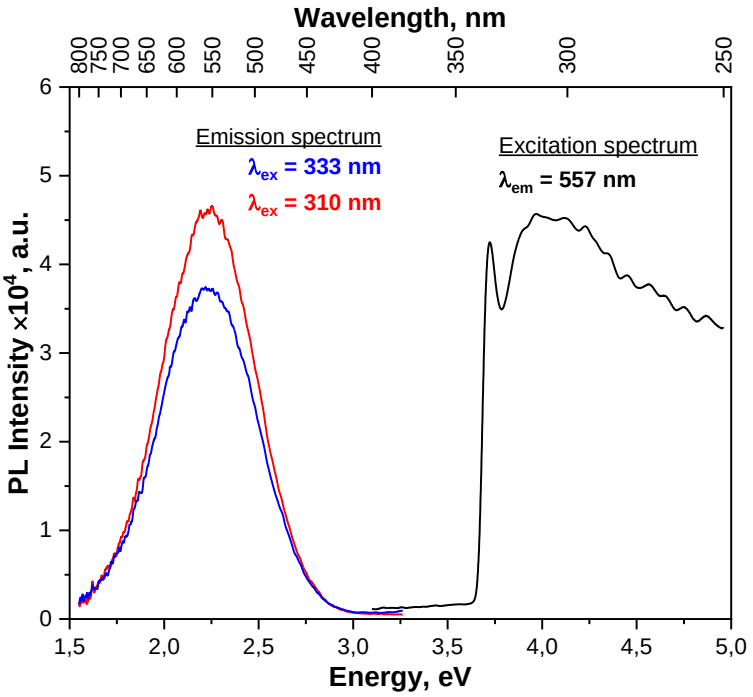

Figure 53. The spectrum of low-temperature photoluminescence $(C_7)DAPbCl_4$

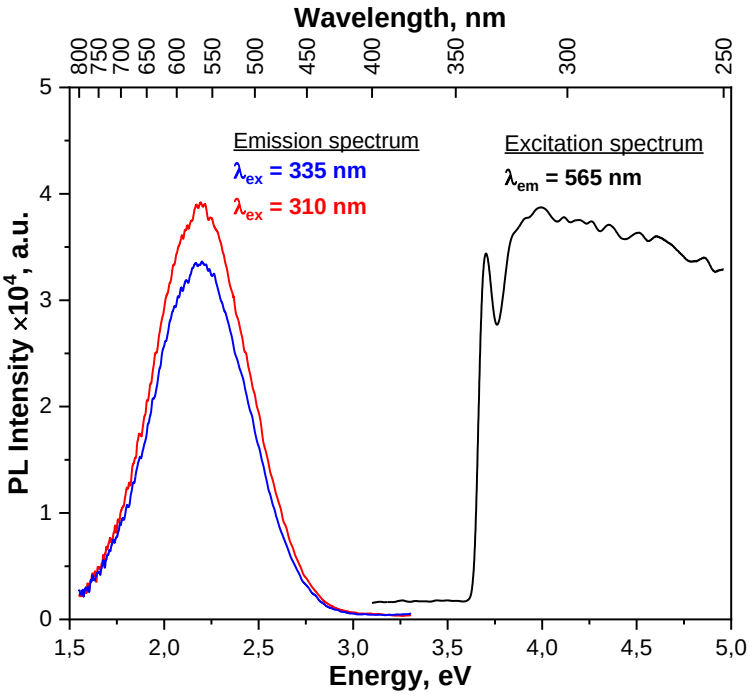

Figure 54. The spectrum of low-temperature photoluminescence $(C_8)DAPbCl_4$

The photoluminescence spectra of bromide-based hybrid crystals shown in Figure 55-59 reveal both similarities with chloride crystals and unique characteristic features.

Unlike chloride samples, the following features are characteristic of bromide samples:

- the presence of two photoluminescence bands: narrowband and broadband;
- higher luminescence intensity of self-trapped excitons compared to the intensity of defect-trapped excitons;
- decrease in the density of the I_{STE}/I_{DTE} luminescence intensity as the organic cation lengths increase from 105 for $(C_4)DA$ to 1 for $(C_8)DA$;
- The value of the free exciton self-trapping energy (E_{tr}) – from 20 to 31 meV.

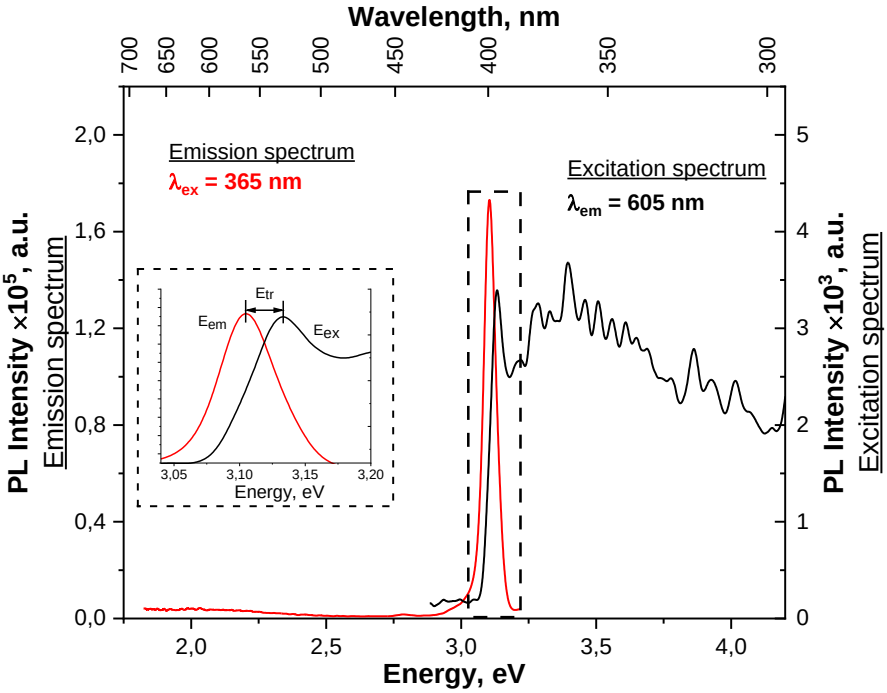

Figure 55. The spectrum of low-temperature photoluminescence $(C_4)DAPbBr_4$. In the insert, the region near the peak of the emission of an self-trapped exciton and the excitation spectrum of a free exciton.

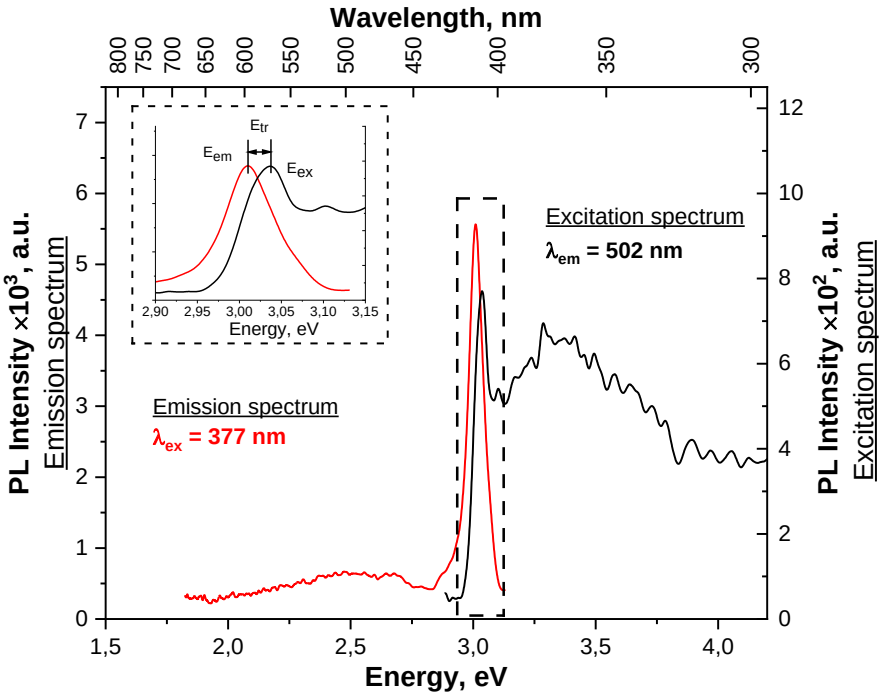

Figure 56. The spectrum of low-temperature photoluminescence $(C_5)DAPbBr_4$. In the insert, the region near the peak of the emission of an self-trapped exciton and the excitation spectrum of a free exciton.

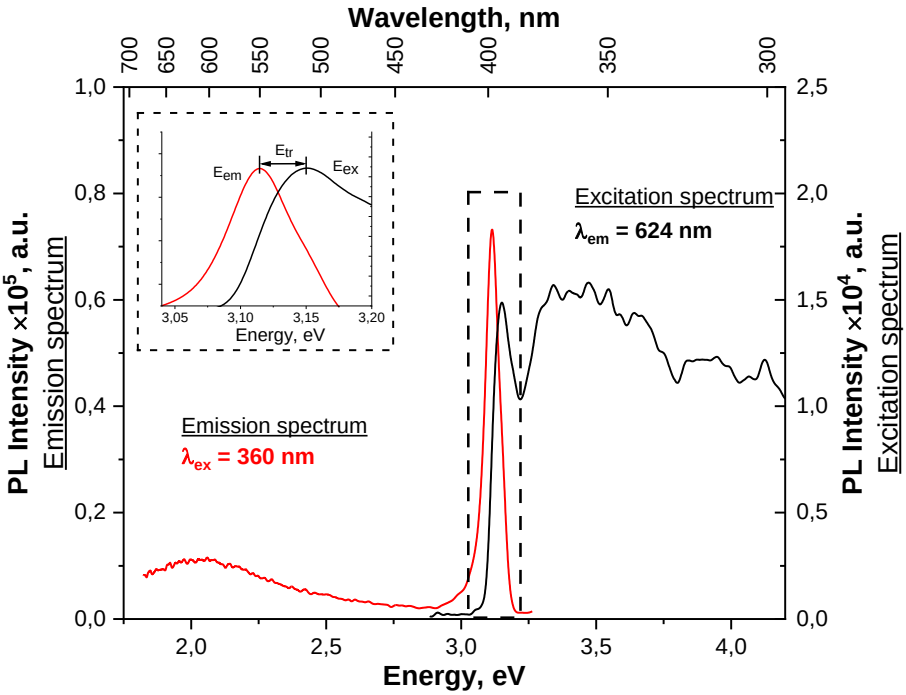

Figure 57. The spectrum of low-temperature photoluminescence $(C_6)DAPbBr_4$. In the insert, the region near the peak of the emission of an self-trapped exciton and the excitation spectrum of a free exciton.

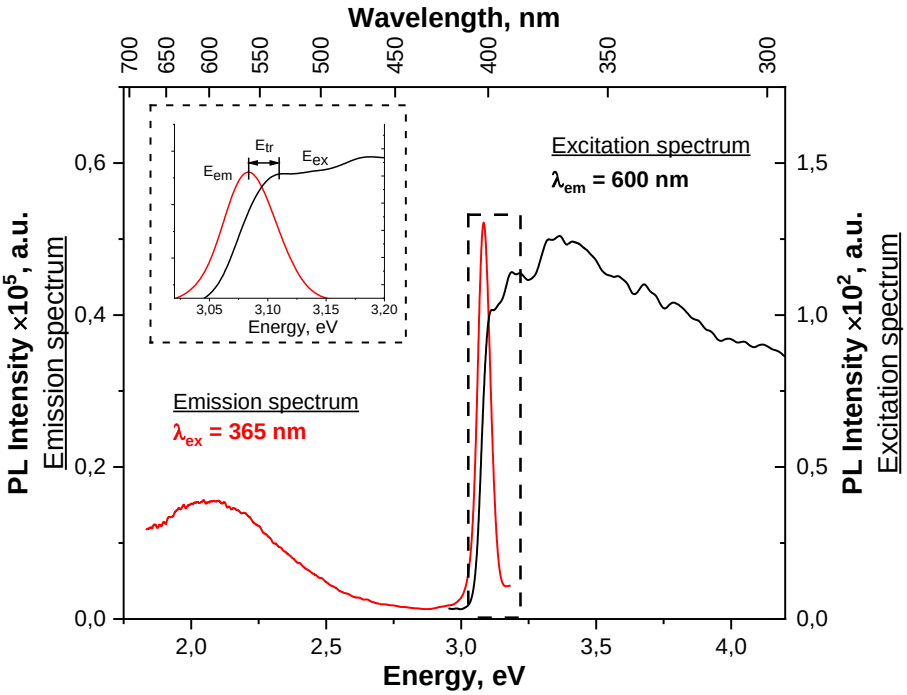

Figure 58. The spectrum of low-temperature photoluminescence $(C_7)DAPbBr_4$. In the insert, the region near the peak of the emission of an self-trapped exciton and the excitation spectrum of a free exciton.

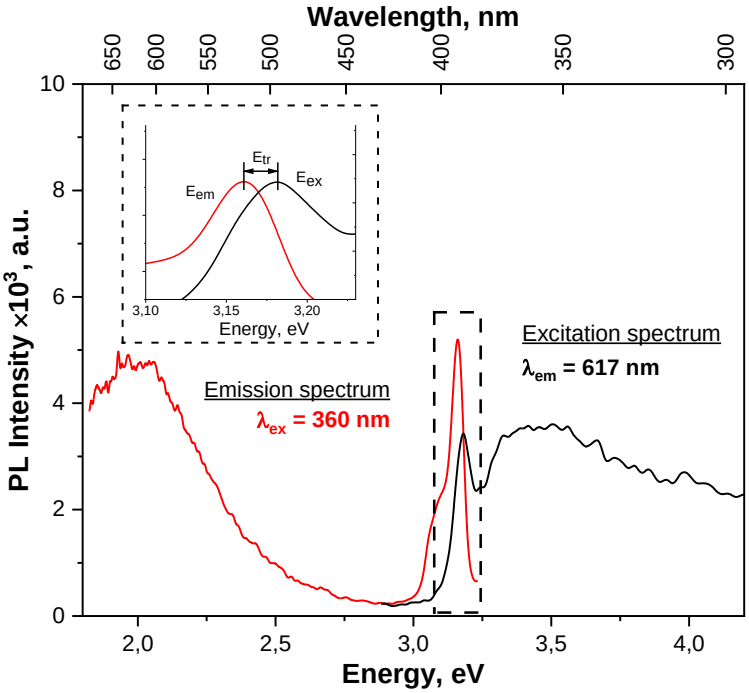

Figure 59. The spectrum of low-temperature photoluminescence $(C_8)DAPbBr_4$. In the insert, the region near the peak of the emission of an self-trapped exciton and the excitation spectrum of a free exciton.

The luminescence of iodide hybrid crystals, shown in Figure 60-62, differs significantly from the previously considered chloride and bromide cases. The first significant difference is that samples with an odd number of carbon atoms in the organic cation - $(C_5)DAPbI_4$ and $(C_7)DAPbI_4$ - do not have luminescent properties, which is probably due to their one-dimensional zero-dimensional structures. Secondly, the photoluminescence intensity of suitable samples is orders of magnitude lower than the usual values for chloride and bromide.

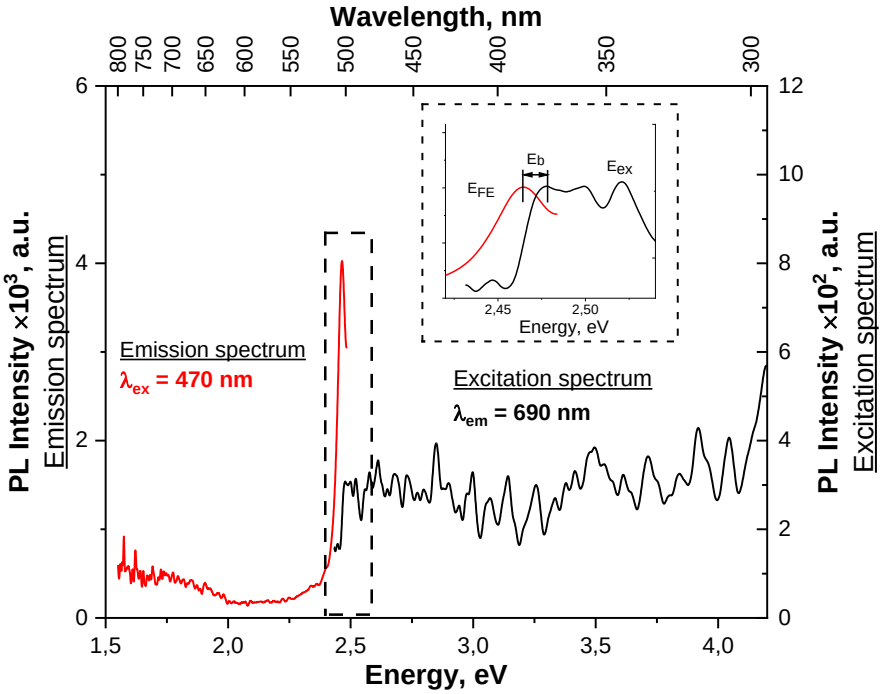

Figure 60. The spectrum of low-temperature photoluminescence $(C_4)DAPbI_4$. In the insert, the region near the peak of the emission of an self-trapped exciton and the excitation spectrum of a free exciton.

Otherwise, the luminescence of samples with an even number of carbon atoms in an organic cation is $(C_4)DAPbI_4$, $(C_6)DAPbI_4$ and $(C_8)DAPbI_4$ is similar to the luminescence of bromide samples: the intensity of narrow–band luminescence of self-trapped excitons (STE) is many times greater than the intensity of broadband luminescence of defect-trapped excitons (DTE), and the energy of self-trapping of free exciton (E_{tr}) lies in the range of 11-31 meV.

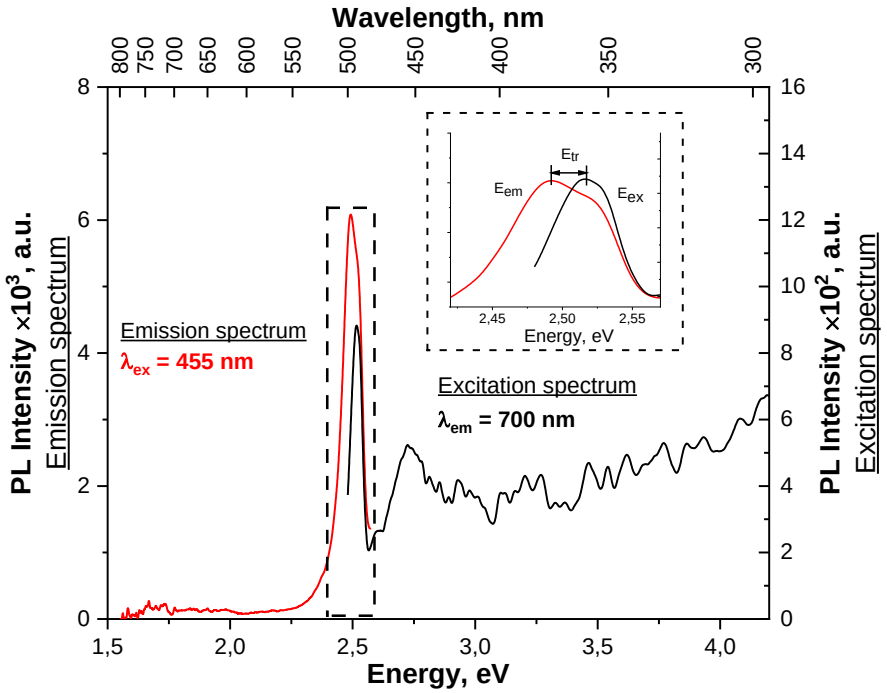

Figure 6110. The spectrum of low-temperature photoluminescence $(C_6)DAPbI_4$. In the insert, the region near the peak of the emission of an self-trapped exciton and the excitation spectrum of a free exciton.

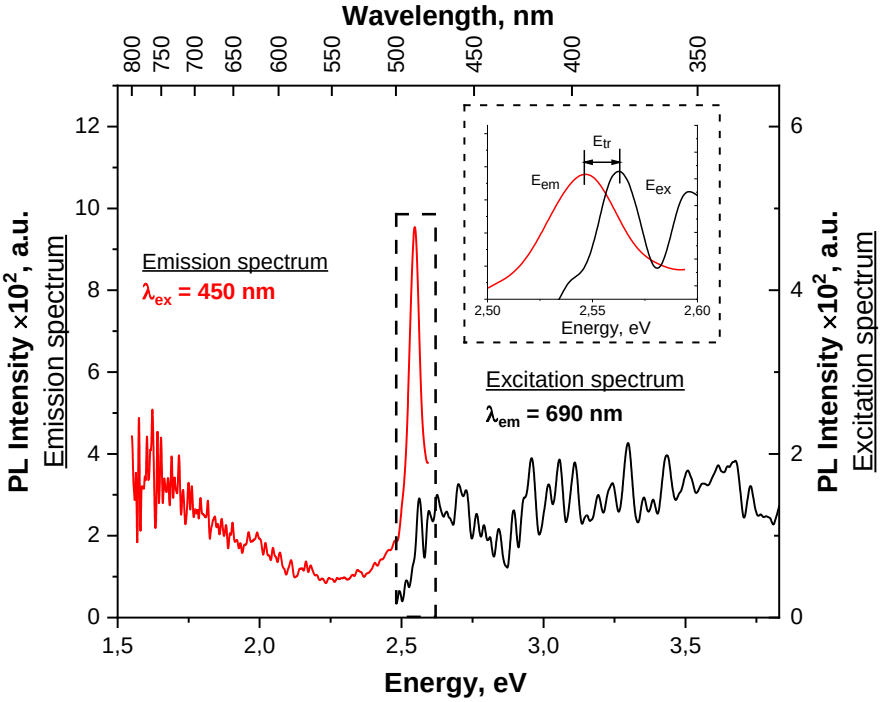

Figure 62. The spectrum of low-temperature photoluminescence $(C_8)DAPbI_4$. In the insert, the region near the peak of the emission of an self-trapped exciton and the excitation spectrum of a free exciton.

Table 6 shows some parameters of low-temperature photoluminescence for various hybrid perovskites of type $(C_n)DAPbX_4$, depending on their anionic (X=Cl, Br, I) and cationic (n=4-8) composition.

Table 6. Main parameters of low-temperature photoluminescence for various hybrid perovskites of the type $(C_n)DAPbX_4$ (X=Cl, Br, I; n=4-8).

Composition	E_{STE}, nm	E_{STE}, eV	E_{DTE}, nm	E_{DTE}, eV	E_{ex}, nm	E_{ex}, eV	E_{tr}, meV	I_{STE}/I_{DTE}
$(C_4)DAPbCl_4$	нет	нет	550,0	2,254	341,6	3,63	-	-
$(C_5)DAPbCl_4$	нет	нет	564,9	2,195	331,7	3,738	-	-
$(C_6)DAPbCl_4$	нет	нет	550,0	2,254	339,5	3,652	-	-
$(C_7)DAPbCl_4$	нет	нет	552,5	2,244	333,1	3,723	-	-
$(C_8)DAPbCl_4$	нет	нет	562,2	2,206	334,2	3,71	-	-
$(C_4)DAPbBr_4$	399,3	3,105	443,9	2,793	395,6	3,134	29,0	105,482
$(C_5)DAPbBr_4$	412,1	3,009	498,6	2,487	408,2	3,038	28,7	11,161
$(C_6)DAPbBr_4$	398,2	3,114	619,3	2,002	394,2	3,146	31,6	7,136
$(C_7)DAPbBr_4$	402,1	3,084	598,2	2,073	398,9	3,108	24,7	3,362
$(C_8)DAPbBr_4$	392,4	3,16	624,6	1,985	389,9	3,18	20,3	1,106
$(C_4)DAPbI_4$	504,1	2,460	736,6	1,683	497,6	2,492	32,2	6,353
$(C_5)DAPbI_4$	нет	нет	нет	нет	нет	нет	-	-
$(C_6)DAPbI_4$	498,5	2,487	709,0	1,749	492,4	2,518	30,9	8,416
$(C_7)DAPbI_4$	нет	нет	нет	нет	нет	нет	-	-
$(C_8)DAPbI_4$	486,7	2,548	676,8	1,832	484,5	2,559	11,6	5,016

Legend to the table: "no" - no luminescence.

The following patterns are visible:

- all hybrid crystals with luminescent properties demonstrate broadband luminescence of defect-trapped excitons; however, among them only bromide and iodide samples demonstrate narrowband luminescence of self-trapped excitons;
- iodide crystals with an odd number of carbon atoms in an organic cation do not have luminescent properties;
- chloride crystals are characterized only by broadband luminescence of defect-trapped excitons;
- bromide and iodide crystals are characterized by a high luminescence intensity of self-trapped excitons compared to the luminescence intensity of defect-trapped excitons;

- the free excitons energy of self-trapping depends on the anionic composition of hybrid crystals: for bromide crystals – in the range from 20 to 31 meV, for iodide crystals – from 11 to 31 meV;
- for bromide crystals, the ratio of luminescence intensities of self-trapped excitons and defect-trapped excitons depends on the size of the organic cation and decreases as it grows;
- for iodide crystals, the position of the luminescence band of self-trapped excitons depends on the length of the organic cation and shifts to a region of smaller wavelengths as it grows.

3.4 X-ray photoelectron spectroscopy of hybrid compounds based on lead halides and a homologous series of limiting diamines of the form $[H_3N\text{-}(CH_2)_n\text{-}NH_3]PbX_4$ (n=4-8, X=Cl, Br, I)

3.4.1 Investigation of the chemical environment of the main elements

Figure 63 and Figure 64 show the XPS spectra of hybrid crystals $(C_6)DAPbX_4$, (X=Cl, Br, I) in the field of characteristic binding energies of the main elements included in their structure (halogens, as well as nitrogen, carbon and lead).

The characteristic lead lines Pb4f7/2 and Pb4f5/2 have a half-width of 1.8 eV (Figure 63a). Each of these lines can be approximated by only one Gaussian. The position of the maxima of the Pb4f5/2 line for $(C_6)DAPbCl_4$, $(C_6)DAPbBr_4$ and

$(C_6)DAPbI_4$ amounts to 139.0 eV, 138.4 eV and 138.2 eV, respectively. The observed drift towards lower binding energies is consistent with the literature data [44].

Like the lead lines, the C1s carbon lines (Figure 63 b), characterized by a maximum at 285 eV for all three compositions, can also be approximated by a single Gaussian. That is, neither the position nor the shape of the carbon line depend on the halogen atom.

In turn, each of the Cl2p, Br3d and I4d halogen lines has two well-distinguishable components (Figure 63 c). Given that some of the halogens are located in the equatorial plane of the octahedra at a greater distance from the amino groups, and some are at the vertices of the octahedra facing the amino groups, this splitting may be due to this.

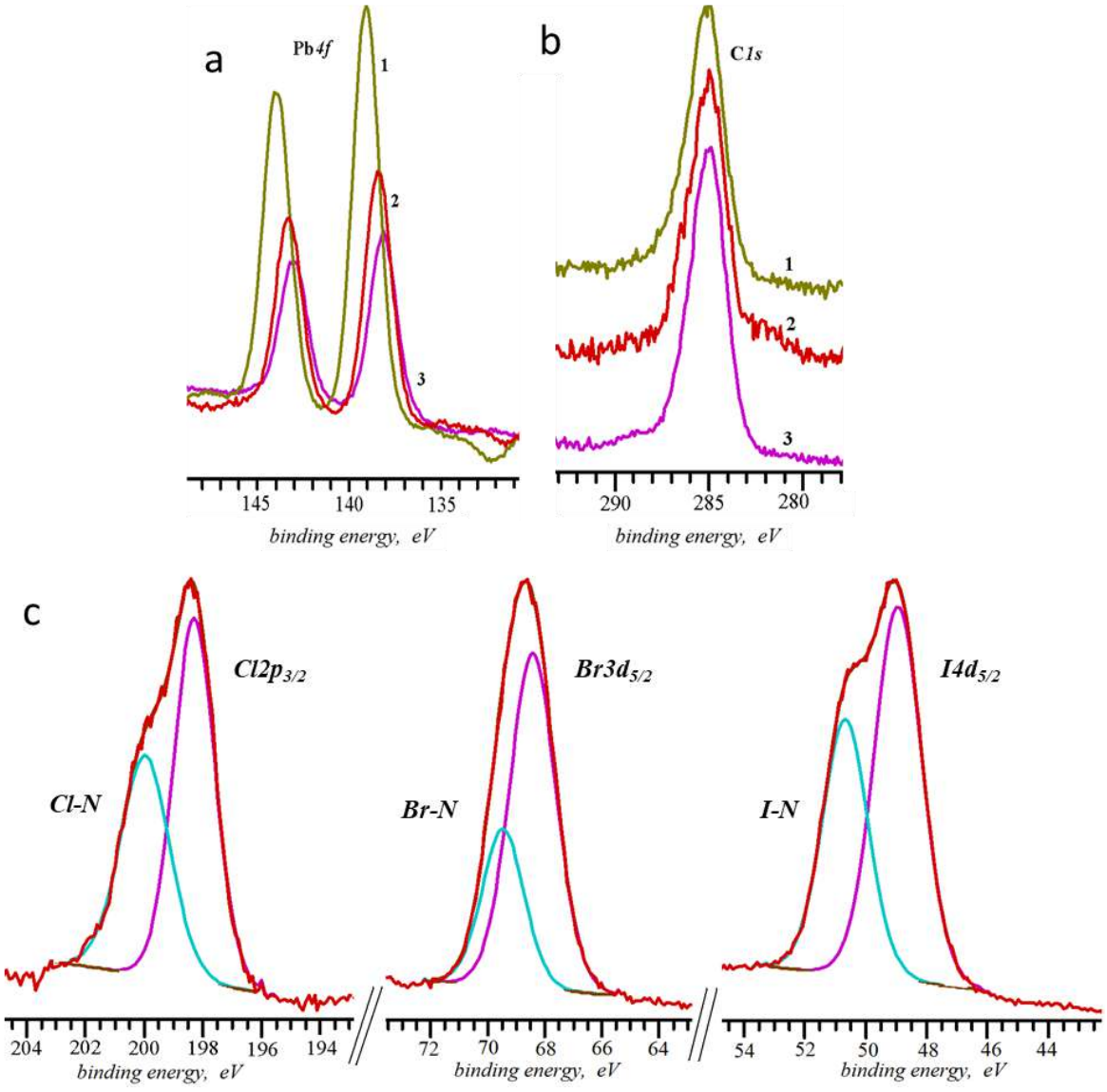

Figure 63. XPS spectra $(C_6)DAPbX_4$, (X=Cl, Br, I) in the field of characteristic binding energies: a) Pb4f; b) C1s; c) halogens - 1, 2 и 3 соответствуют Cl, Br и I.

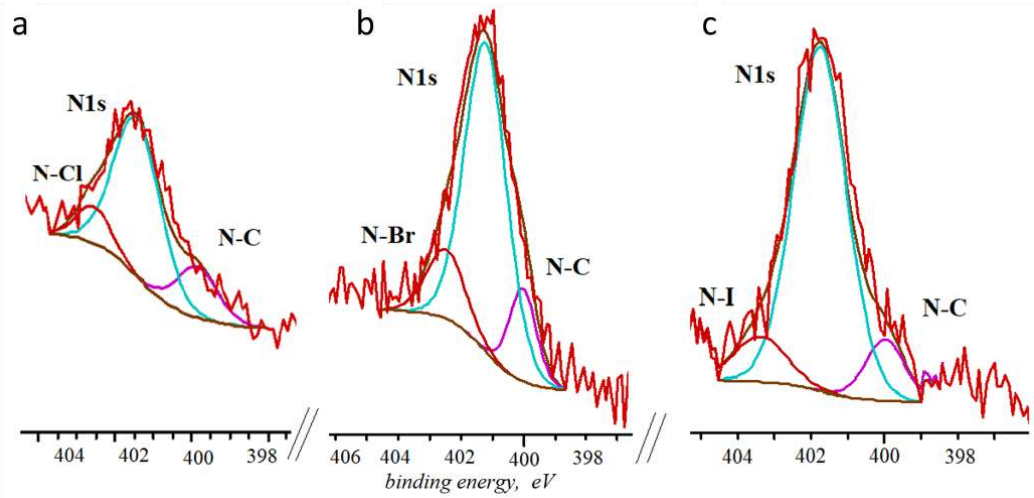

Figure 64. XPS spectra $(C_6)DAPbX_4$ in the field of characteristic binding energies N1s for: a) X=Cl; b) X=Br; c) X=I.

The characteristic nitrogen line (Figure 64) has a complex shape and can be approximated by a superposition of three Gaussians. Such a complex shape is due to chemical shifts that occur as a result of the interaction of nitrogen atoms with both the carbon skeleton of the organic cation (N-C) and with halogens (N-Cl, N-Br, N-I), which was manifested above in the splitting of halogen lines. The latter is due to the fact that nitrogen atoms are involved in the formation of hydrogen bonds -N-H...X, which stabilize the low-dimensional hybrid structure of hybrid crystals [33].

The conducted studies of other samples gave similar results and are not given here so as not to overload the text of the work.

3.4.2 Determination of the output operation and the potential of the valence band ceiling

To determine the output operation (E_{WF}) and the potential of the valence band ceiling (E_{VB}) for all objects of study, the spectra of the valence band (VB) and

secondary Electron Cut-off (SEC) were measured by X-ray photoelectron spectroscopy. The values of the output operation were calculated according to formula (4), and the ceiling of the valence band was calculated according to formula (5) in accordance with the methodology proposed in [52]:

$$E_{WF} = h\nu - E_{SEC}, \quad (4)$$

$$E_{VB} = h\nu - (E_{SEC} - E_I), \quad (5)$$

where hν is the radiation energy (1253.6 eV), E_{SEC} is the energy determined by linear interpolation of the high–energy edge of the secondary electron breakage line, E_I is the energy determined by linear interpolation of the low–energy edge of the line in the valence region.

Typical results obtained during these measurements are shown in Figure 65.

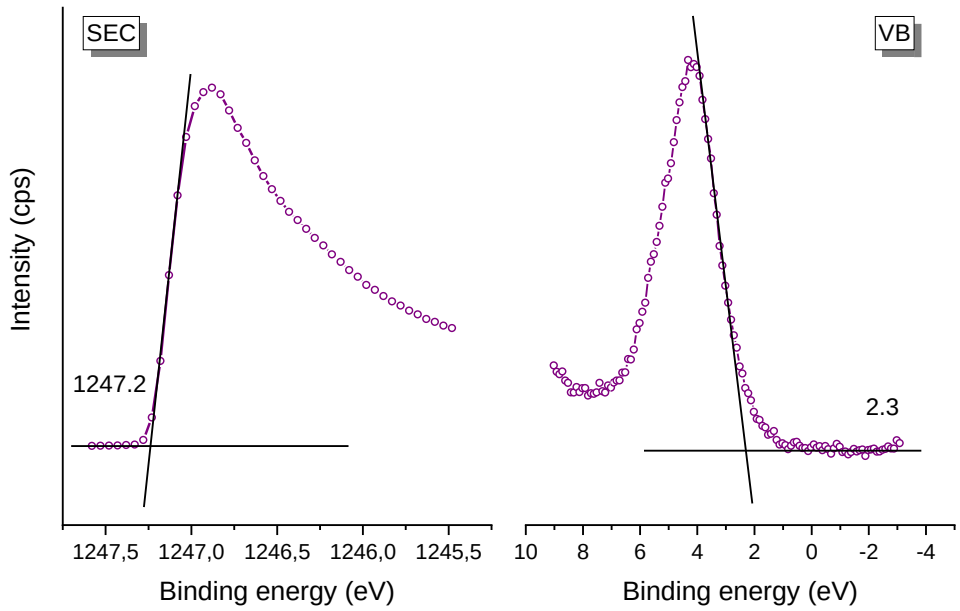

Figure 65. Spectra of secondary electron breakage (SEC) и valence band (VB) spectra measured for the sample $(C_4)DAPbBr_4$.

The data obtained by the described method for all studied hybrid crystals on the maximum of the valence band, as well as the ionization potential, are shown in Table 7.

Table 7. Values of output operation (WF), valence band ceiling (E_{VB}) for hybrid perovskites ($(C_n)DAPbX_4$ (n=4-8, X=Cl, Br, I).

Composition	X=Cl		X=Br		X=I	
	E_{VB}, eV	WF, eV	E_{VB}, eV	WF, eV	E_{VB}, eV	WF, eV
$(C_4)DAPbX_4$	2.6	6.5	2.3	6.4	1.2	6.8
$(C_5)DAPbX_4$	2.7	7	2.3	7.1	1.2	8.6
$(C_6)DAPbX_4$	2.8	6.5	2.4	6.9	1.2	7.6
$(C_7)DAPbX_4$	2.8	6.4	2.4	6.2	1.3	7
$(C_8)DAPbX_4$	2.8	6.7	2.3	7.1	1.3	7.5

It can be seen from the table that the position of the ceiling of the valence band relative to the outlet operation practically does not depend on the length of the carbon chain of the organic cation and is determined by the type of anion in the composition of perovskite. In [56] for example $(C_6)DAPbX_4$ (X=Cl, Br, I) It has been shown that the position of the valence band ceiling is determined by the electronegativity of the anion. Figure 66a shows the position of the valence band ceiling depending on the electronegativity of the anion.

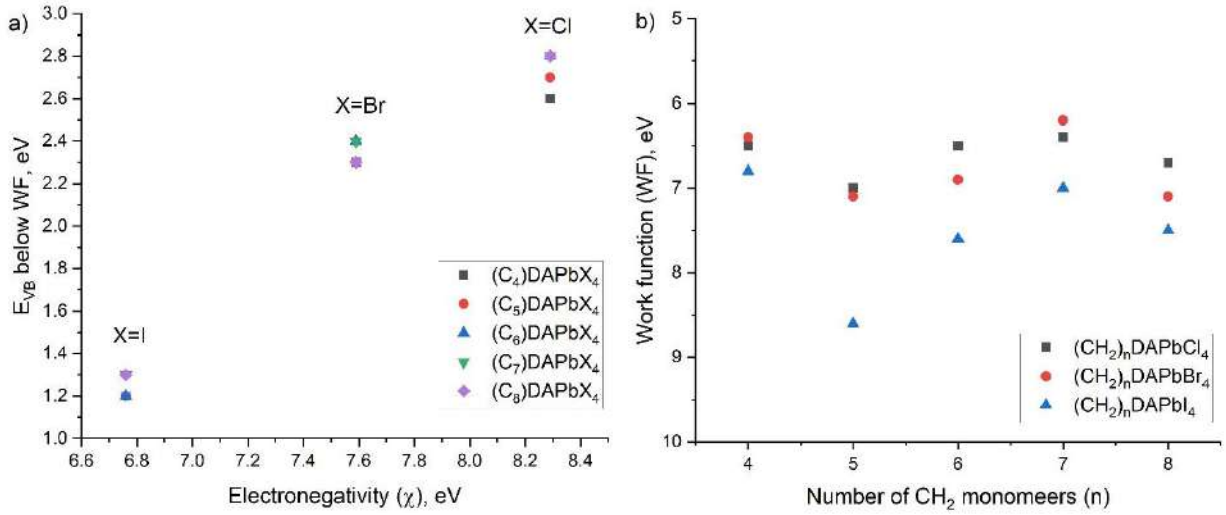

Figure 66. The position of the valence band ceiling is below the output operation depending on the electronegativity of the anion (a) and the value of the output operation (b) for various hybrid perovskites.

It can be seen that, as in the work [56], There is a direct relationship between the electronegativity of the anion and the position of the valence band ceiling relative to the operation of the perovskite outlet. Only for chloride perovskites, there is also a trend to increase the potential of the valence band ceiling as the length of the organic cation increases.

At the same time, the behavior of the output (Figure 66b) differs significantly and shows a significant influence on itself both from the type of anion and the length of the carbon chain of the organic cation.

3.5 Electronic band structures of hybrid compounds based on lead halides and a homologous series of diamines of the form $[H_3N\text{-}(CH_2)_n\text{-}NH_3]PbX_4$ (n=4-8, X=Cl, Br, I)

The values of the band gap widths obtained earlier by the Diffuse Reflectance Spectroscopy (Table 5) and data on the position of the valence band ceiling potential and the position of the outlet operation (Table 7) make it possible to construct the band structures of the studied hybrid perovskites (Figure 67).

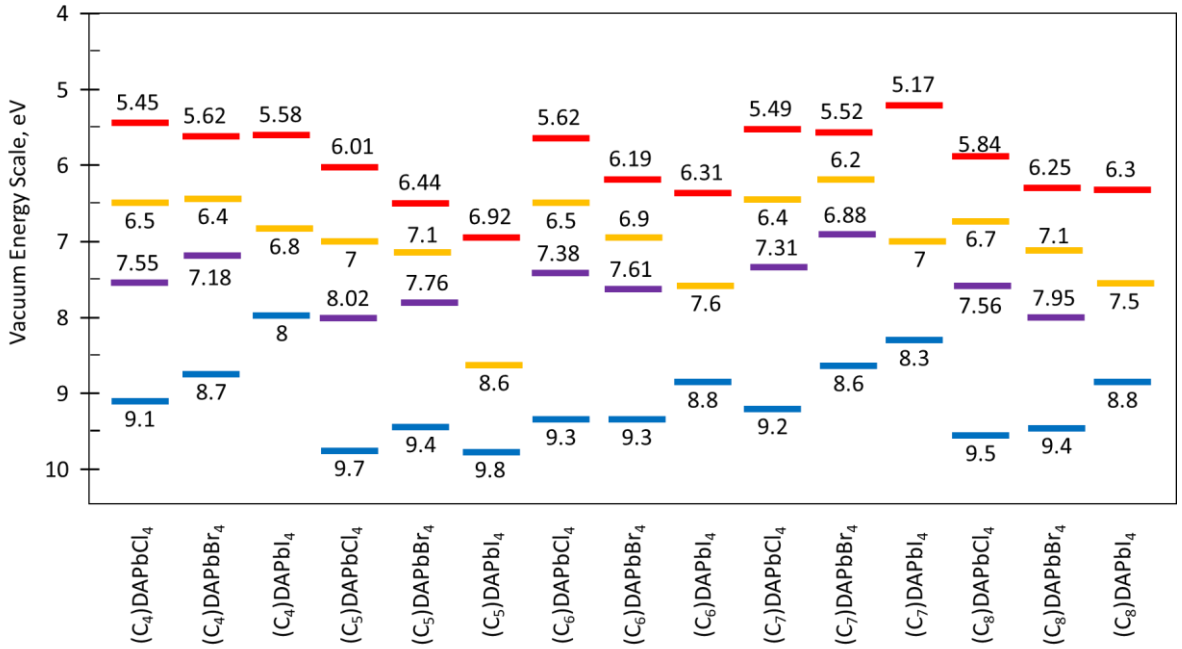

Figure 67. Electronic band structures $(C_n)DAPbX_4$ (n=4-8, X=Cl, Br, I). Blue lines indicate the position of the valence band ceiling, red lines indicate the bottom of the conduction band, yellow lines indicate the values of the output operation, purple lines indicate the expected defect levels (explanations in the text).

Several general patterns can be seen. Thus, for chloride and bromide perovskites, the output operation is shifted to the sides of the conduction band and is located under it approximately at a distance of ¼ of the width of the band gap of the corresponding perovskite. For iodide perovskites, the output work occupies a position almost in the middle between the valence band and the conduction band. Such a shift in the output operation is usually observed in semiconductors if there is an n-type defect or impurity in them, the energy localization of which is shown in Figure 67 by the purple line.

3.6 Phase transitions in hybrid compounds based on lead halides and a homologous series of diamines of the form $[H_3N-(CH_2)_n-NH_3]PbX_4$ (n=4-8, X=Cl, Br, I)

3.6.1 Differential scanning calorimetry

The presence of sufficiently extended linear organic cations in the studied hybrid crystals separating the inorganic layers makes it possible for them to exist in various crystalline configurations, the transition between which can be accompanied by phase transitions. To study the phase diversity of the hybrid crystals under study, they were analyzed by differential scanning calorimetry.

Figure 68 shows thermogravimetric curves in the cooling-heating cycles for hybrid crystals $(C_n)DAPbCl_4$ (n=4-8). It can be seen that the presence of a phase transition and its characteristics for chloride crystals strongly depend on the structure of the organic cation.

For $(C_4)DAPbCl_4$ (Figure 68a) the phase transition is observed at 289-326 K. Here and further, the temperature of the phase transition during cooling is indicated first (T_{cool}), and then – when heated (T_{heat}). The temperature difference of the phase transition for a hybrid crystal $(C_4)DAPbCl_4$ $\Delta T = T_{heat} - T_{cool}$ amounts 36 K.

For $(C_5)DAPbCl_4$ (Figure 68b) there is no phase transition.

For $(C_6)DAPbCl_4$ (Figure 68c) several phase transitions are observed. The first is observed when 403-401 K (ΔT = 2 K). The second phase transition is more complex: when cooled, the corresponding exoeffect is observed at 269 K, whereas when heated, two endoeffects are observed at 229 K (ΔT = -40 K) and at 293 K (ΔT = 24 K).

For $(C_7)DAPbCl_4$ (Figure 68d) one phase transition is observed at 369-375 K (ΔT = 6 K).

For $(C_8)DAPbCl_4$ (Figure 68e) there is also one phase transition at 311-319 K (ΔT = 8 K).

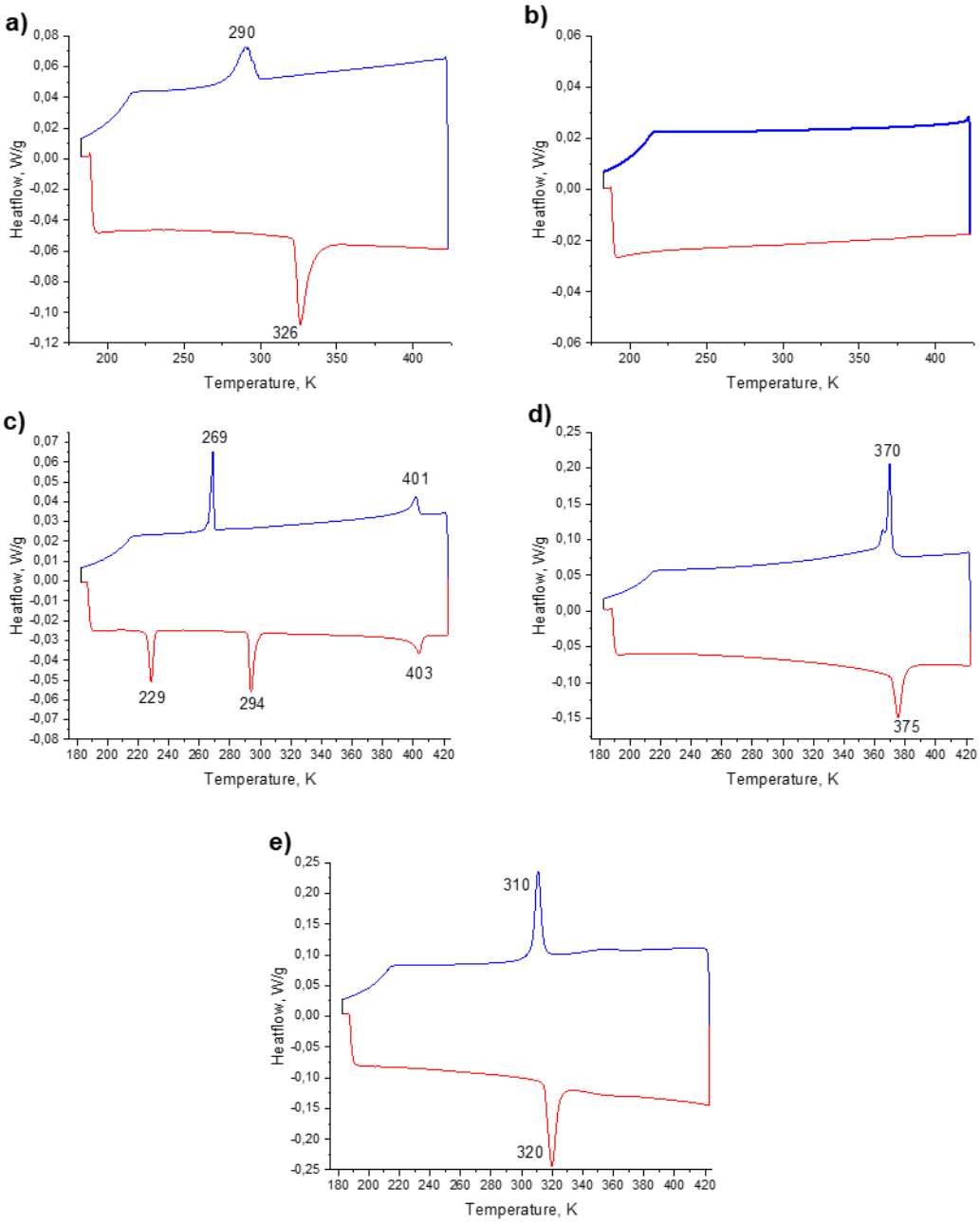

Figure 68. DSC curves in "cooling-heating" cycles for $(C_n)DAPbCl_4$: n=4 (a), n=5 (b), n=6 (c), n=7 (d), n=8 (e).

Figure 69 shows the DSC curves in the cooling-heating cycles for hybrid crystals $(C_n)DAPbBr_4$ (n=4-8). As in the case of chloride crystals, it can be seen that the presence of a phase transition and its characteristics strongly depend on the structure of the organic cation.

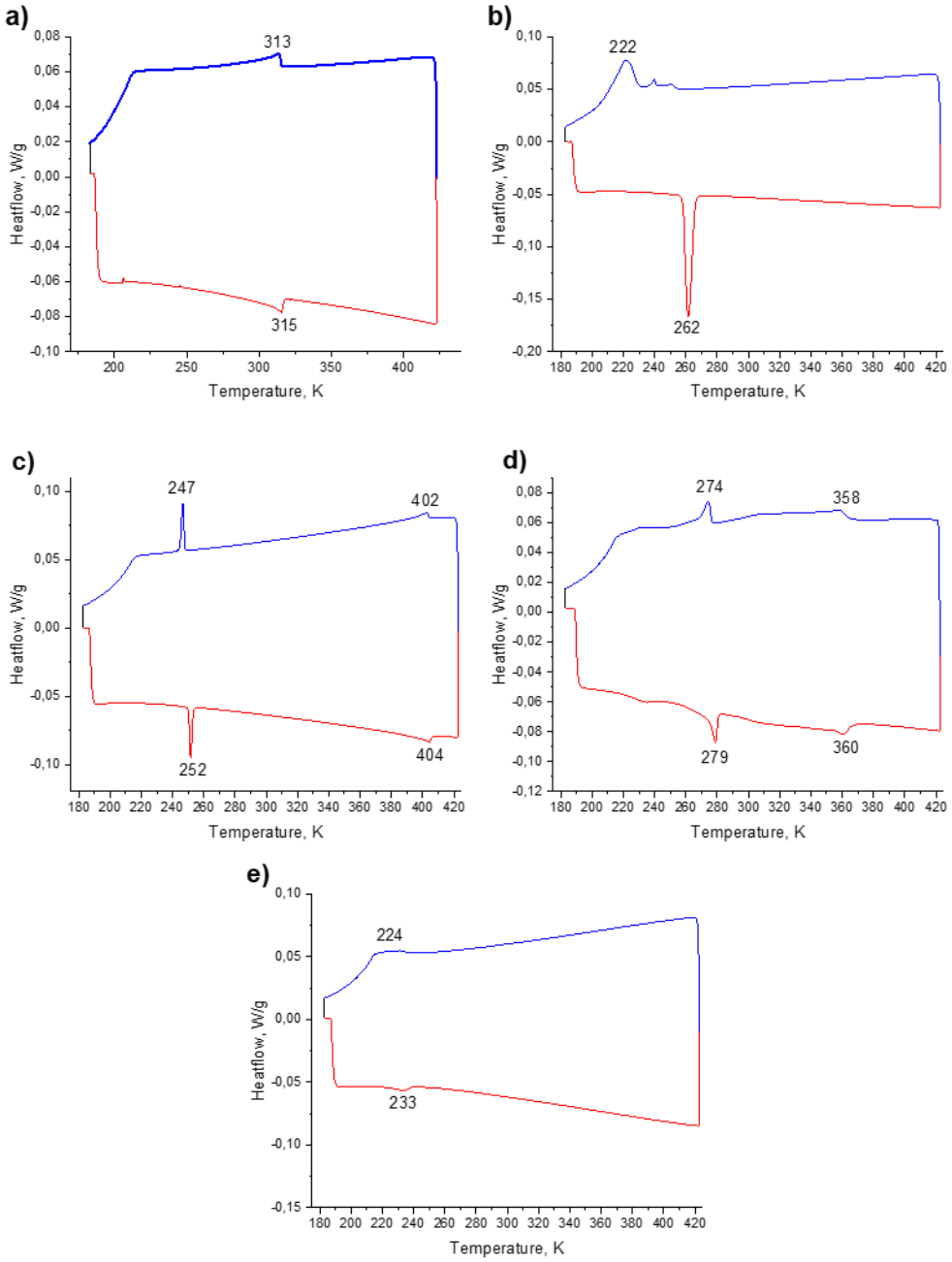

Figure 69. DSC curves in "cooling-heating" cycles for $(C_n)DAPbBr_4$: n=4 (a), n=5 (b), n=6 (c), n=7 (d), n=8 (e).

For $(C_4)DAPbBr_4$ (Figure 69a) the phase transition is observed at 313-315 K (ΔT = 2 K). For $(C_5)DAPbBr_4$ (Figure 69b) the phase transition is observed at 222-262 K (ΔT = 40 K). For $(C_6)DAPbBr_4$ (Figure 69c) is characterized by two phase transitions: one is observed at 402-404 K (ΔT = 2 K), the second one is at 247-252 K (ΔT = 5 K). For $(C_7)DAPbBr_4$ (Figure 69d) is also characterized by two phase transitions: at 358-361 K (ΔT = 3 K) and at 273-278 K (ΔT = 4,5 K). For $(C_8)DAPbBr_4$ (Figure 69e) one

phase transition is observed at 232-234 K (ΔT = 2 K). Thus, it can be seen that mainly bromide crystals are characterized by phase transitions with a low value of ΔT (up to 5 K). The only exception is composition $(C_5)DAPbBr_4$.

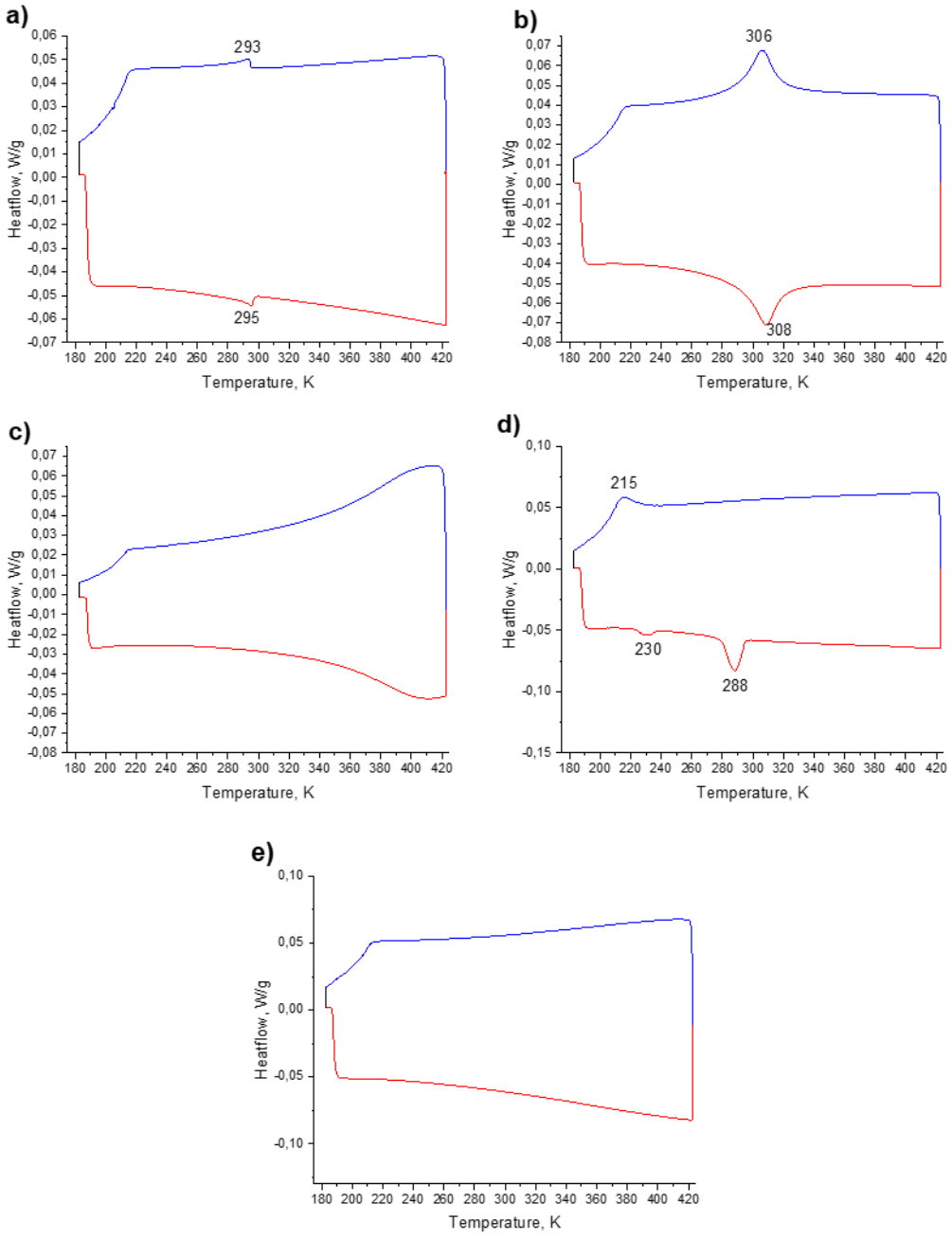

Figure 70. DSC curves in "cooling-heating" cycles for $(C_n)DAPbI_4$: n=4 (a), n=5 (b), n=6 (c), n=7 (d), n=8 (e).

Figure 70 shows the DSC curves in the cooling-heating cycles for hybrid crystals $(C_n)DAPbI_4$ (n=4-8). Samples $(C_6)DAPbI_4$ and $(C_8)DAPbI_4$ does not exhibit phase transitions. For crystals $(C_4)DAPbI_4$ phase transition is observed at 293-295 K (ΔT = 2

K). For crystals $(C_5)DAPbI_4$ phase transition is observed at 306-308 K (ΔT = 2 K). For crystals $(C_7)DAPbI_4$ has a pattern similar to $(C_6)DAPbCl_4$: When cooled, the exo-effect is observed at 217 K, whereas when heated, two endo-effects are observed: at 231 K (ΔT = 14 K) and at 288 K (ΔT = 71 K).

Table 8 summarizes data on the temperatures of phase transitions and the corresponding enthalpy changes for hybrid crystals of various anionic and cationic compositions.

Table 8. Temperature and enthalpy of exo- and endo-effects during cooling/heating of hybrid compounds of the type $(C_n)DAPbX_4$ (X=Cl, Br, I).

Состав	Cooling		Heating	
	T, K	ΔH, J/mol	T, K	ΔH, J/mol
$(C_4)DAPbCl_4$	290	1032	326	1422
$(C_5)DAPbCl_4$	no	no	no	no
$(C_6)DAPbCl_4$	401	201	403	191
	269	383	293	453
			229	336
$(C_7)DAPbCl_4$	369	1659	375	1472
$(C_8)DAPbCl_4$	311	3128	319	3623
$(C_4)DAPbBr_4$	313	271	315	210
$(C_5)DAPbBr_4$	222	1899	262	3016
$(C_6)DAPbBr_4$	402	60	404	84
	247	381	252	400
$(C_7)DAPbBr_4$	358	158	361	198
	273	435	278	527
$(C_8)DAPbBr_4$	232	660	234	128
$(C_4)DAPbI_4$	293	137	295	129
$(C_5)DAPbI_4$	306	2801	308	2924
$(C_6)DAPbI_4$	no	no	no	no
$(C_7)DAPbI_4$	217	1372	231	246
			288	1906
$(C_8)DAPbI_4$	no	no	no	no

Table legend: "no" - absence of exo- or endo-effect.

3.6.2 Investigation of phase transitions by X-ray diffraction methods

Due to the large number of research objects and the abundance of detected phase transitions in them, the features of the structure change of hybrid crystals during phase transitions will be studied in more detail using the example $(C_6)DAPbCl_4$, as in the most typical sample.

In [56] the unit cell of the hybrid crystal under study at 100K is described and analyzed in detail (see Figure 71a). When the temperature rises to 323 K, a change in the crystal lattice is observed (see Figure 71b). Here and further, the sample characterized by the crystal lattice shown in Figure 71a will be called the low-temperature (LT) phase $(C_6)DAPbCl_4$ (LT-$(C_6)DAPbCl_4$), and the sample characterized by the crystal lattice shown in Figure 71b is the high–temperature (HT) phase $(C_6)DAPbCl_4$ (HT-$(C_6)DAPbCl_4$).

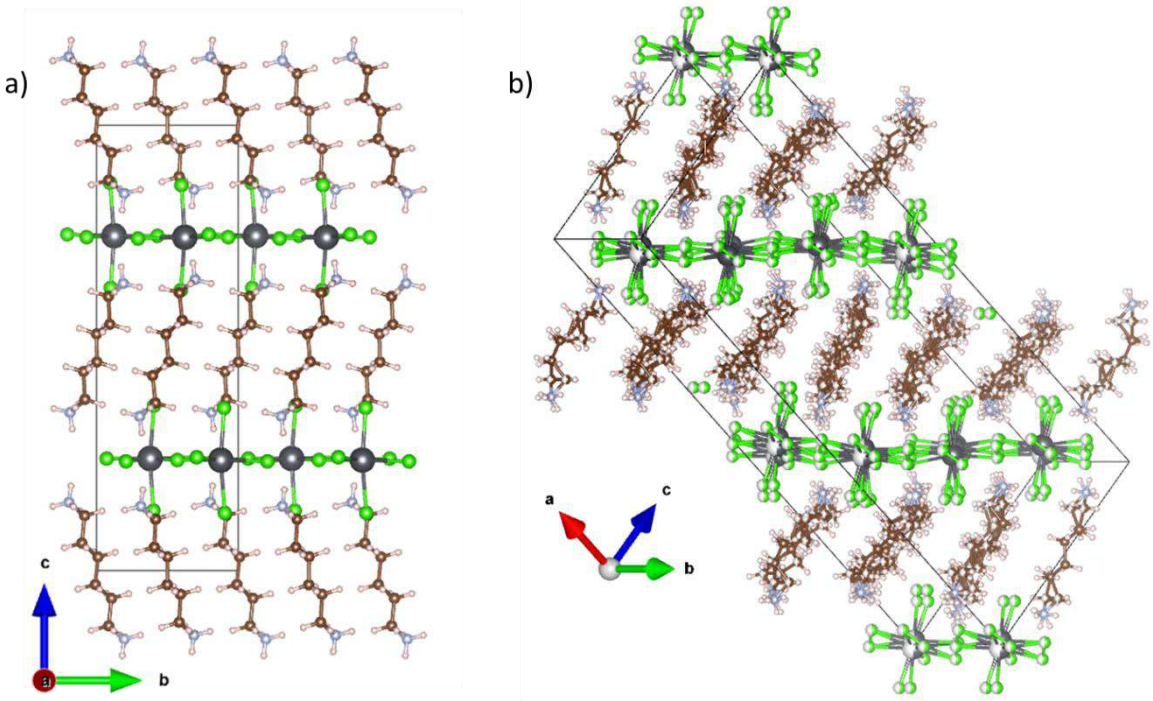

Figure 71. The unit cell of a hybrid crystal $(C_6)DAPbCl_4$ at 100 K (a) and at 323 K (b).

It can be seen that the HT-phase is characterized by a significant degree of disordering of both the network of inorganic octahedra (Figure 72) and the organic cation (Figure 73).

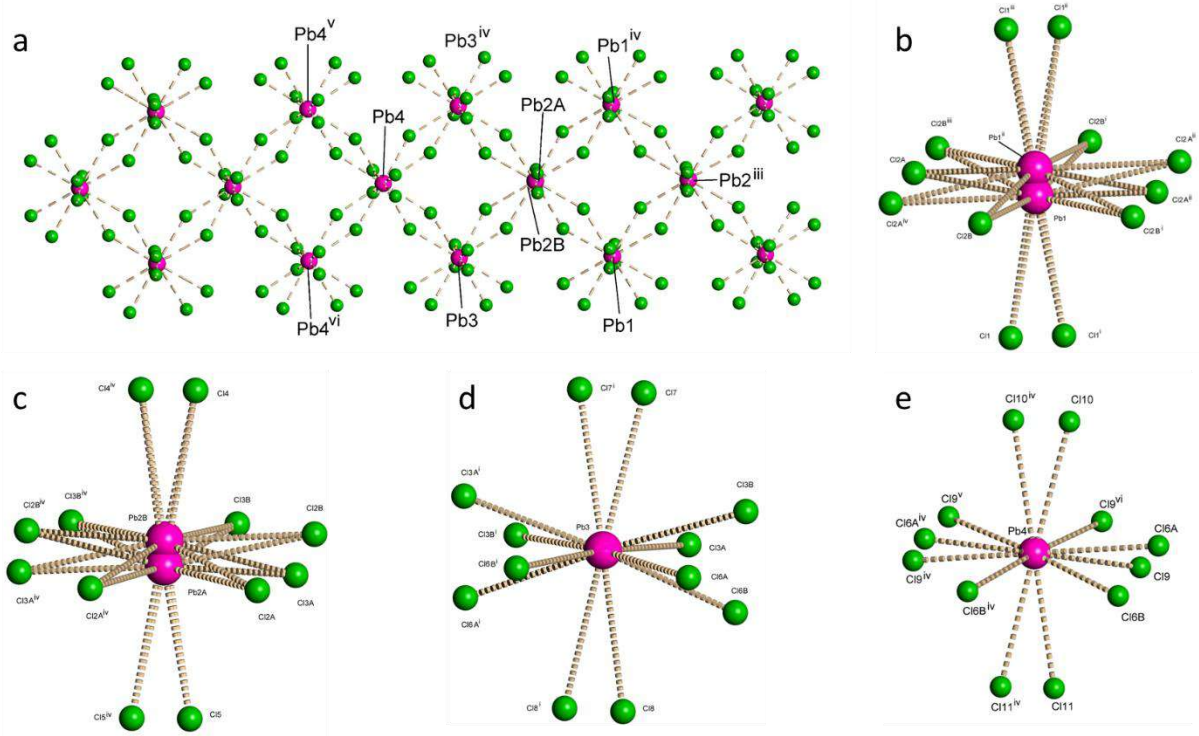

Figure 72. Disordering of a network of inorganic octahedra (a) and some octahedra (b-e) in an elementary cell LT-$(C_6)DAPbCl_4$.

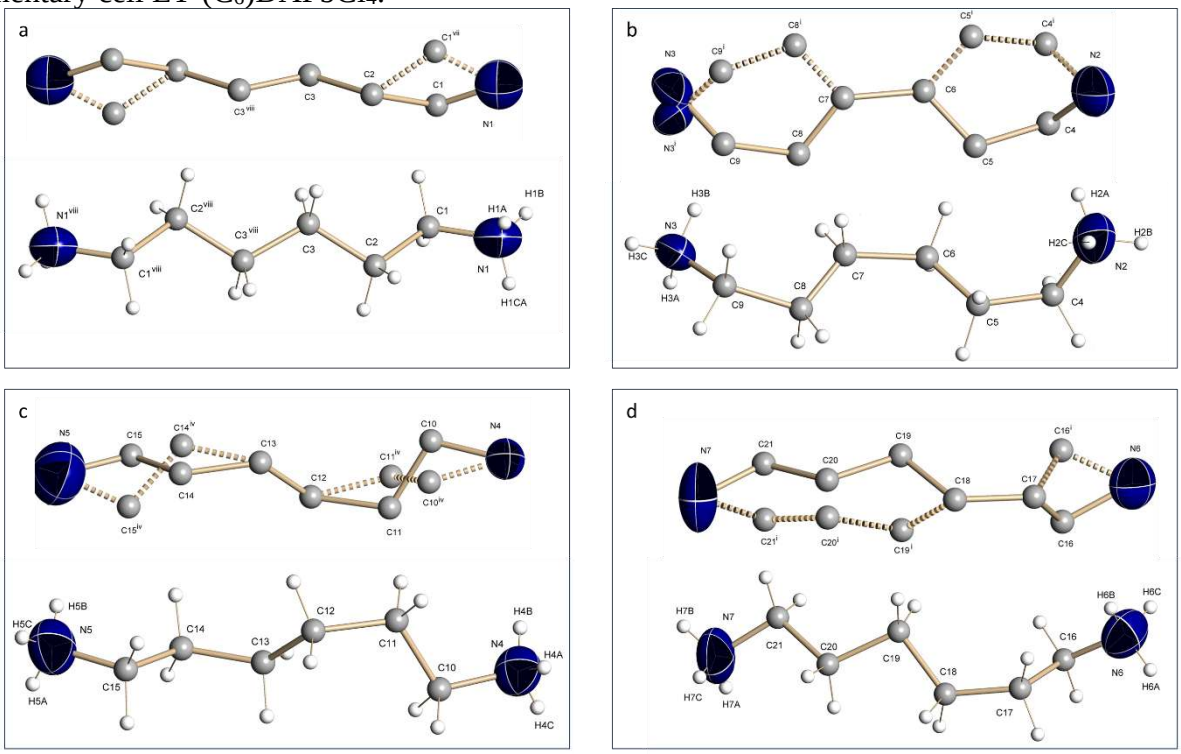

Figure 73. Different conformations of the organic cation present in the unit cell LT-$(C_6)DAPbCl_4$. Each conformation is shown in two projections.

Table 9 shows data on the bond lengths between different atoms in the unit cell of a hybrid perovskite $(C_6)DAPbCl_4$.

Table 9. Bond lengths (in Å) in the unit cell LT-$(C_6)DAPbCl_4$.

Pb1—Cl1^{i}	2.631 (6)	Pb2B—Cl3B	2.888 (5)	Cl1—Pb1^{ii}	3.115 (6)
Pb1—Cl1	2.631 (6)	Pb2B—Cl3B^{iv}	2.888 (5)	Cl2A—Pb1^{ii}	2.835 (6)
Pb1—Cl2A^{ii}	2.835 (6)	Pb2B—Cl3A^{iv}	2.891 (5)	Cl2B—Pb1^{ii}	2.922 (6)
Pb1—Cl2A^{iii}	2.835 (6)	Pb2B—Cl3A	2.891 (5)	Cl9—Pb4^{vi}	2.879 (5)
Pb1—Cl2B^{i}	2.840 (6)	Pb2B—Cl5	3.093 (6)	N1—C1	1.37 (3)
Pb1—Cl2B	2.840 (6)	Pb2B—Cl5^{iv}	3.093 (5)	N1—C1^{vii}	1.37 (3)
Pb1—Cl2A	2.904 (6)	Pb3—Cl3A	2.822 (5)	C1—C2	1.47 (2)
Pb1—Cl2A^{i}	2.904 (6)	Pb3—Cl3A^{i}	2.822 (5)	C2—C3	1.49 (3)
Pb1—Cl2B^{ii}	2.922 (6)	Pb3—Cl7	2.834 (5)	C3—C3^{viii}	1.44 (3)
Pb1—Cl2B^{iii}	2.922 (6)	Pb3—Cl7^{i}	2.834 (5)	N2—C4	1.437 (16)
Pb1—Cl1^{ii}	3.115 (6)	Pb3—Cl6B^{i}	2.863 (5)	N3—C9	1.474 (17)
Pb1—Cl1^{iii}	3.115 (6)	Pb3—Cl6B	2.863 (5)	C4—C5	1.46 (3)
Pb2A—Cl5	2.658 (5)	Pb3—Cl3B^{i}	2.867 (5)	C5—C6	1.37 (3)
Pb2A—Cl5^{iv}	2.658 (5)	Pb3—Cl3B	2.867 (5)	C6—C7	1.54 (3)
Pb2A—Cl2A^{iv}	2.811 (6)	Pb3—Cl8^{i}	2.872 (5)	C7—C8	1.31 (3)
Pb2A—Cl2A	2.811 (6)	Pb3—Cl8	2.872 (5)	C8—C9	1.51 (3)
Pb2A—Cl3A^{iv}	2.817 (5)	Pb3—Cl6A	2.907 (5)	N4—C10	1.470 (15)
Pb2A—Cl3A	2.817 (5)	Pb3—Cl6A^{i}	2.907 (5)	N5—C15	1.455 (17)
Pb2A—Cl2B	2.929 (6)	Pb4—Cl10	2.833 (6)	C10—C11	1.515 (17)
Pb2A—Cl2B^{iv}	2.929 (6)	Pb4—Cl10^{iv}	2.833 (6)	C11—C12	1.527 (17)
Pb2A—Cl3B	2.933 (5)	Pb4—Cl6B	2.845 (5)	C12—C13	1.431 (18)
Pb2A—Cl3B^{iv}	2.933 (5)	Pb4—Cl6B^{iv}	2.846 (5)	C13—C14	1.494 (17)
Pb2A—Cl4	3.082 (6)	Pb4—Cl11	2.846 (6)	C14—C15	1.503 (19)
Pb2A—Cl4^{iv}	3.082 (6)	Pb4—Cl11^{iv}	2.846 (6)	N6—C16	1.454 (18)
Pb2B—Cl4	2.647 (6)	Pb4—Cl9^{iv}	2.851 (6)	N7—C21	1.432 (15)
Pb2B—Cl4^{iv}	2.647 (6)	Pb4—Cl9	2.851 (6)	C16—C17	1.511 (18)
Pb2B—Cl2B	2.855 (6)	Pb4—Cl6A^{iv}	2.865 (5)	C17—C18	1.454 (17)
Pb2B—Cl2B^{iv}	2.855 (6)	Pb4—Cl6A	2.865 (5)	C18—C19	1.520 (18)
Pb2B—Cl2A^{iv}	2.873 (6)	Pb4—Cl9^{v}	2.879 (5)	C19—C20	1.511 (18)
Pb2B—Cl2A	2.874 (6)	Pb4—Cl9^{vi}	2.879 (5)	C20—C21	1.507 (17)

To analyze the degree of disorder of the crystal structure, a number of formal parameters are usually used, described in detail in section 3.1.3. Also, to analyze changes in the degree of disorder of the crystal lattice $(C_6)DAPbCl_4$ An important parameter is the volume of inorganic octahedra (V). Table 10 shows all the above parameters for the high- and low-temperature phases $(C_6)DAPbCl_4$.

Table 10. Parameters of disordered crystal lattice $(C_6)DAPbCl_4$.

The disordered parameter	The number of the octahedron in the unit cell	HT-$(C_6)DAPbCl_4$	LT-$(C_6)DAPbCl_4$
d_{av}, Å	1	2,8326	2.8757
	2	2,8711	2.8757
	3	2,8613	2.8757
	4	2,8519	2.8757
	5	2,8608	-
$\Delta d*10^{-3}$, Å	1	29,35	10.18
	2	36,06	10.18
	3	5,15	10.18
	4	3,14	10.18
	5	11,98	-
σ_{in}^2, ^{02}	1	180,775	33.1915
	2	394,6057	33.1915
	3	200,4606	33.1915
	4	317,2978	33.1915
	5	309,6877	-
V, Å^3	1	27,9893	31.2682
	2	25,9648	31.2682
	3	28,4878	31.2682
	4	26,4612	31.2682
	5	27,0892	-
φ_{av}, ^{0}		151.19	141,44

First of all, we note that the low-temperature phase is characterized by completely identical inorganic octahedra. There are four such octahedra in the unit cell, and they are characterized by the same disordered parameters. The transition to the high-temperature phase is accompanied by the fact that there are five octahedra in the unit cell and all of them have their own disordered parameters.

The high-temperature phase is characterized by a smaller average distance between lead and chlorine in the octahedron (d_{av}). If for the low-temperature phase the average distance is 2.8757 Å, then for the high-temperature phase the d_{av} lies in the range 2.8326-2.8711 Å. At the same time, this reduction in bond lengths is accompanied by a decrease in octahedron volumes from 31.2682 Å^3 for the low-temperature phase to 25.9648-28.4878 Å^3 for the high-temperature phase.

The situation is more complicated with the Δd parameter.The low-temperature phase is characterized by Δd = 10,18*10^{-3} Å. In the high-temperature phase, some of the octahedra (Nos. 3 and 4) are characterized by a lower value Δd (5,15*10^{-3} and 3,14*10^{-3} Å), part (№1 и 2) – large (29,35*10^{-3} and 36,06*10^{-3} Å), and the octahedron № 5 – about the same (11,98*10^{-3} Å).

In an ideal octahedron, the lead atom is located in the center and all angles of Cl-Pb-Cl (α) are 90^0. Accordingly, the parameter σ_{in}^2 characterizes the disorder of the crystal lattice associated with the displacement of the lead atom from the center of the octahedron. Table 10 shows that this type of disordered structure is also much more pronounced in the high-temperature phase. At the same time, there is no obvious correlation between the parameters Δd and σ_{in}^2.

In an ideal three-dimensional Perovskite, there is no inclination of the octahedra relative to each other, respectively, the angle Pb-Cl-Pb (φ_{av}) is 180^0. The smaller this angle, the more disordered the network of octahedra is relative to each other. Table 10 shows that the high-temperature phase has a large value of the angle φ_{av} (151.19^0) compared with the low-temperature one (141.44^0), which indicates a greater degree of structural perfection of the network of inorganic octahedra.

Thus, the high-temperature phase is characterized by a greater degree of distortion of the octahedra, but a more perfect structure of the network of octahedra, less inclined relative to each other. That is, we can say that the transition between phases is accompanied by a change in the type of disordered crystal lattice.

This once again confirms the competition found earlier in the analysis of the structure of all 15 hybrid crystals between two types of disorder of their crystal lattice: either the deformation of octahedra while maintaining the relative perfection of the connection of octahedra with each other; or the preservation of the relative perfection of the structure of individual octahedra with an increase in the degree of disorder of the octahedron network.

If the data of single-crystal X-ray diffraction make it possible to establish the structures of elementary cells of high- and low-temperature phases, then the dynamics

of the transition of a hybrid crystal between these phases can be observed using powder X-ray phase analysis (PXRD). Figure 74 shows the overview powder diffractograms of $(C_6)DAPbCl_4$ obtained in the "cooling" and "heating" modes, and in Figure 75 – the most characteristic area of diffractograms for LT- and HT-phases.

It can be seen that the transition from the high-temperature to the low-temperature phase during cooling occurs at 258 K (compare curves 2 and 3, Figure 74). When heated, the reverse transition is observed at high temperatures – in the region of 293 K (compare curves 15 and 16, Figure 74). Thus, according to powder diffraction data, it is also possible to talk about the existence of hysteresis in the transition between high- and low-temperature phases of perovskite $(C_6)DAPbCl_4$.

The powder X-ray diffraction data are in perfect agreement with the above DSC data: the phase transition from the high- to low-temperature phase corresponds to the exoeffect at 269 K on the cooling curve, and the transition from the low-to high-temperature phase corresponds to the endoeffect at 293 K on the heating curve. At the same time, the endoeffect at 229 K on the heating curve is not accompanied by a rearrangement of the crystal lattice.

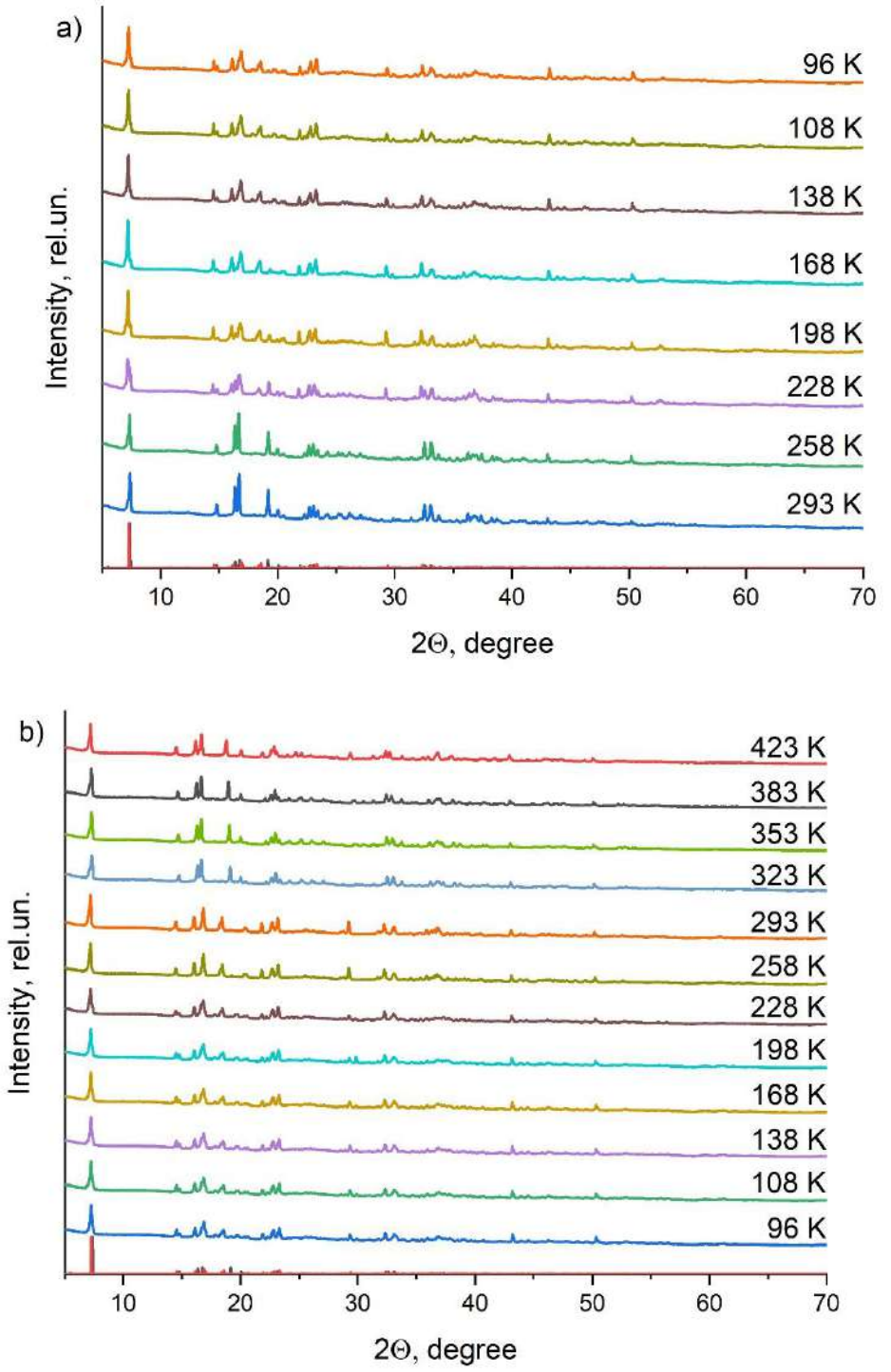

Figure 74. PXRD patterns $(C_6)DAPbCl_4$, obtained in the "cooling" (a) and "heating" (b) modes. The red and black bar charts in the lower parts of the figures correspond to the calculated low-temperature and high-temperature phases.

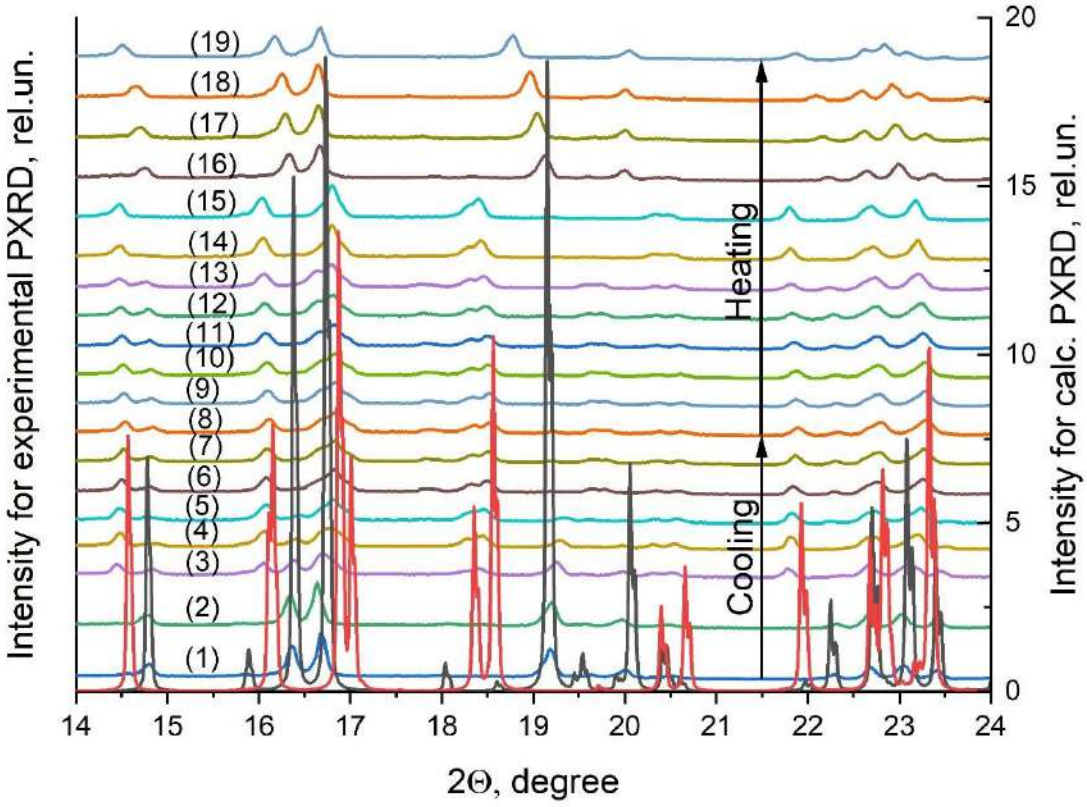

Figure 75. The characteristic area of PXRD patterns $(C_6)DAPbCl_4$ received in the "on cooling" and "on heating" mode. The red and black diffractograms in the lower part of the figure correspond to the calculated low-temperature and high-temperature phases. The numbers indicate experimental diffractograms obtained at temperatures: (1), (15) – 293 K, (2), (14) – 258 K, (3), (13) – 228 K, (4), (12) – 198 K, (5), (11) – 168 K, (6), (10) – 138 K, (7), (9) – 108 K, (8) – 96 K, (16) – 323 K, (17) – 353 K, (18) – 383 K, (19) – 423 K.

3.6.3 Investigation of phase transitions by luminescent methods

As shown earlier [56], This hybrid crystal at low temperatures demonstrates broadband luminescence in the range of 400-700 nm with a maximum in the region of 530 nm (Figure 76). The excitation spectrum has 2 bands: a narrow excitation band with a maximum at 330 nm and a wider band at 250-315 nm with a maximum at 300 nm. The red limit of luminescence excitation (3.76 eV) is close to the band gap of this

crystal, which, as previously established, is 3.79 eV. The wavelength of the luminescence excitation does not affect the position of the maximum emission wavelength. As noted above, broadband luminescence is characteristic of the luminescence of defect-trapped excitons (DLE), and a narrow luminescence excitation band at 330 nm, on the contrary, is characteristic of free excitons (FE).

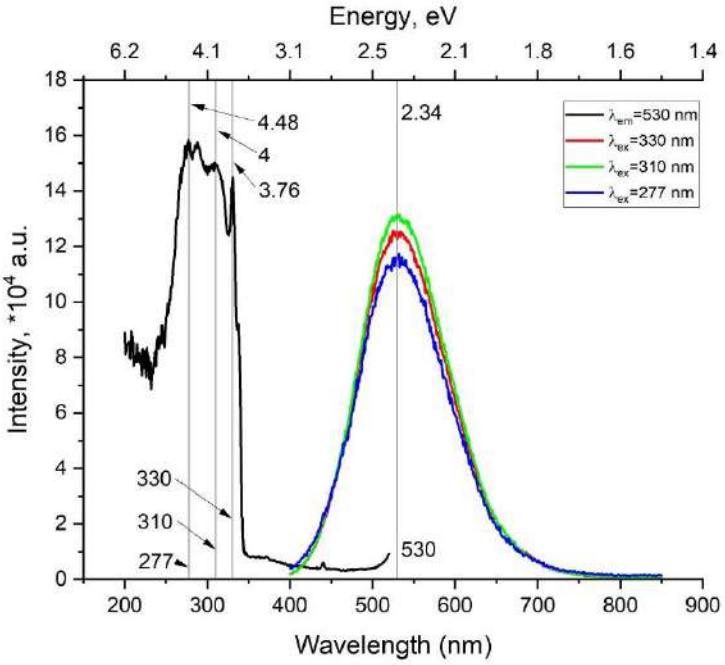

Figure 76. Typical low-temperature photoluminescence spectra and luminescence excitation spectrum for a hybrid crystal $C_6DAPbCl_4$.

With a change in temperature, the intensity of photoluminescence changes due to an increase in the nonradiative (phonon) recombination channel. Figure 77 shows how the luminescence intensity of the hybrid crystal under study changes with temperature changes. This experiment was conducted in two modes. In the first case, the test sample was cooled from room temperature to liquid nitrogen temperature ("on cooling" mode). In the second case, the same sample was heated to room temperature ("on heating" mode). It can be seen that in these two modes the sample behaves differently - temperature hysteresis of luminescence is observed.

Usually, the temperature dependence of the luminescence intensity can be described by the Mott-Seitz equation [57, 58]:

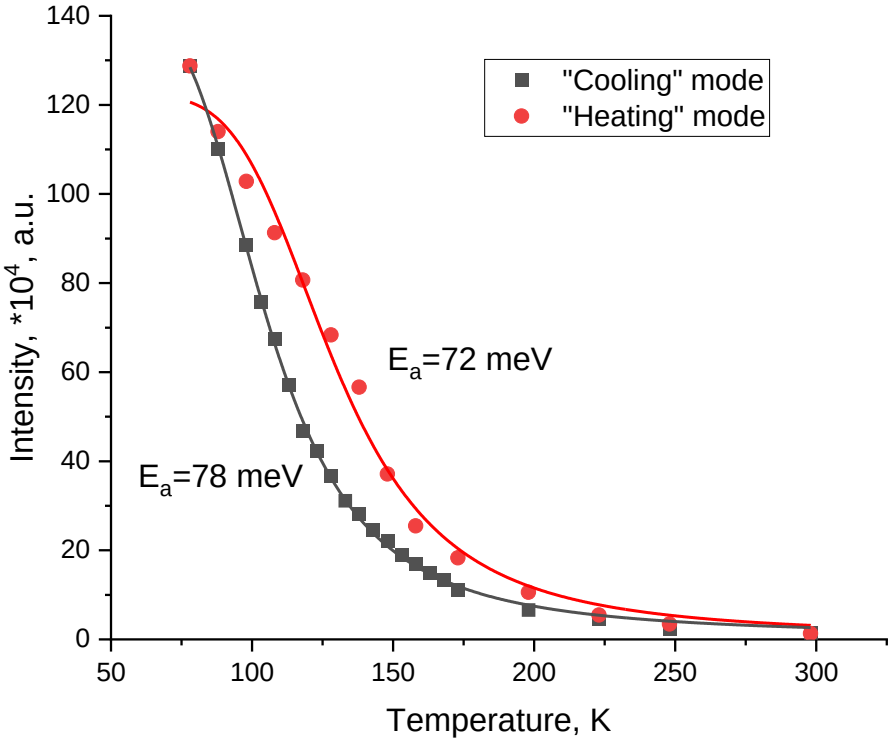

Figure 77. The temperature dependence of the photoluminescence intensity of the $C_6DAPbCl_4$ hybrid crystal obtained in different modes. Lines are the result of interpolation of experimental data (points) by the Mota-Seitz formula (explanations in the text).

$$I(T) = \frac{I_0}{1+Ae^{-E_a/kT}} \quad (1)$$

where I_0 - luminescence intensity at 0 K, E_a - activation energy of luminescence quenching, A - and a dimensionless coefficient associated with the probability of radiative recombination.

The application of formula (1) to the experimental data obtained makes it possible to determine the activation energies of luminescence quenching in the "cooling" mode ($E_a^{cooling} = 0.78$ эВ) and in the "on heating" mode ($E_a^{heating} = 0.72$ эВ).

To confirm that the observed results are precisely the temperature hysteresis of luminescence, an additional experiment was conducted with long-term temperature stabilization at 298 K, 148 K and 81 K in both modes. In this experiment, the sample was kept at a set temperature for 30 minutes before recording the luminescence spectrum. The results of this experiment are shown in Figure 78. It can be seen that at 148 K there is also a difference in luminescence intensity due to the mode ("heating"

or "cooling") in which the sample is located (Figure 78a), which is not observed at room temperature (Figure 78b).

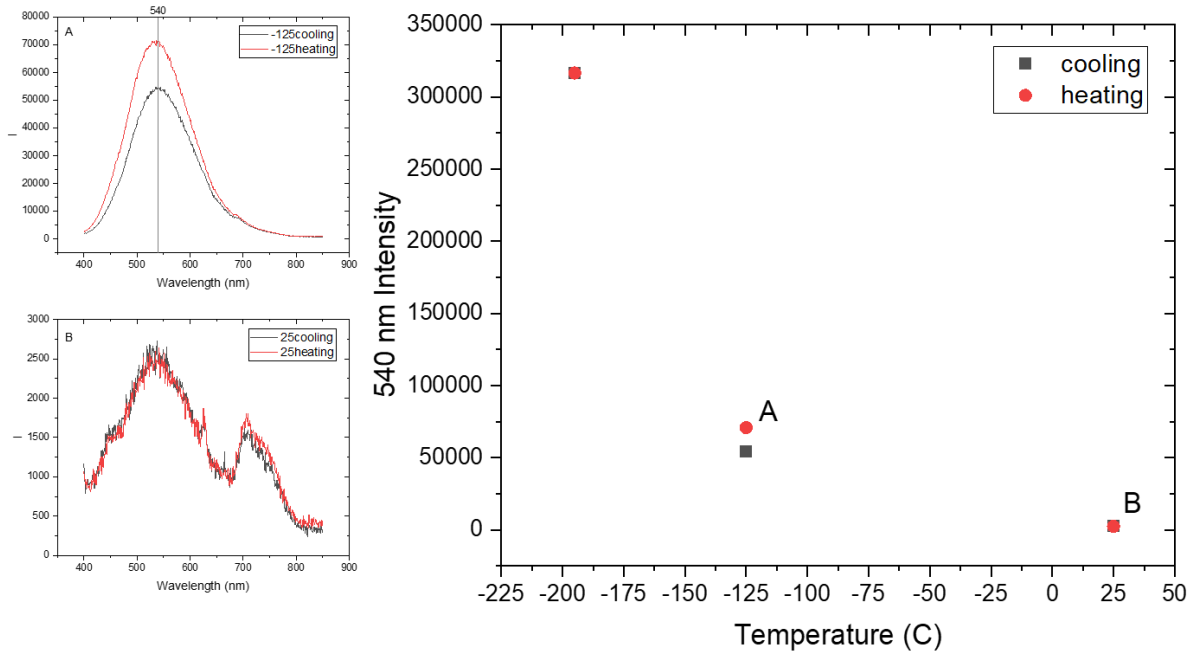

Figure 11. Luminescence intensity of C6DAPbCl4 perovskite at different temperatures and under different heating-cooling modes with long-term stabilization at 148 K.

Thus, it can be seen that the detected phase transition manifests itself not only in a change in structure, but also has its manifestations in luminescent properties.

Conclusions on the 3 chapter

The results obtained allow us to formulate the following main conclusions:

1) The crystal structure of new hybrid crystals based on lead chloride and pentanediamine-1,5, heptanediamine-1,7 and octanediamine-1,8, as well as lead bromide and pentanediamine-1,5, heptanediamine-1,7 was described for the first time.

2) For the first time, the manifestation of the parity effect of the carbon skeleton of an organic cation was discovered and analyzed in hybrid crystals with organic cations represented by saturated alkanediamines and an inorganic sublattice represented by lead halides.
3) For chloride and bromide crystals, the parity effect is manifested as follows: an even carbon skeleton in the structure of an organic cation promotes the formation of two-dimensional hybrid crystals with layers of inorganic octahedra located on top of each other, without displacement, whereas an odd carbon skeleton promotes the formation of two-dimensional hybrid crystals with layers of inorganic octahedra offset relative to each other by half the width octahedra.
4) For iodide crystals, the parity effect manifests itself differently: an even carbon skeleton in the structure of an organic cation contributes to the formation of two-dimensional hybrid crystals, whereas an odd carbon skeleton contributes to the formation of one-dimensional and zero-dimensional structures.
5) It has been established that two-dimensional hybrid crystals (all chloride and bromide, as well as iodide with an even carbon skeleton in the structure of an organic cation) are straight-band semiconductors, transitions from the valence band to the conduction band in which mainly occur at the point Γ of the Brillouin band.
6) It is shown that iodide hybrid crystals with an odd carbon skeleton in the structure of an organic cation, forming one-dimensional structures, are non-bandgap semiconductors.
7) It is shown that during the formation of hybrid crystals based on alkanediamines, two competing processes of disordering the inorganic sublattice are observed: internal, characterized by distortion of the shape of each octahedron or displacement of lead atoms in octahedra from a central position, and external, characterized by the preservation of the relative perfection of the octahedra themselves, but manifested in the inclination of the octahedra relative to each other when they are combined into network.

8) It is shown that all two-dimensional hybrid crystals based on lead halides and alkanediamines have luminescent properties.
9) Typical luminescence of hybrid crystals based on lead halides and alkanediamines may include narrow-band luminescence of self-trapped excitons, broadband luminescence of defect-trapped excitons, or both of these bands, which is determined by the cationic and anionic composition of the hybrid crystal:
    a. chloride hybrid crystals are characterized by the presence of only broadband luminescence of defect-trapped excitons;
    b. bromide and iodide crystals are characterized by the presence of both luminescence bands;
    c. for bromide crystals, the ratio of luminescence intensities of self-trapped excitons and defect-trapped excitons depends on the size of the organic cation and decreases as it grows.
10) The free excitons energy of self-trapping for bromide hybrid crystals lies in the range from 20 to 31 meV, for iodide crystals – from 11 to 31 meV.
11) Phase transitions have been established in hybrid crystals based on lead halides and a homologous series of diamines of the form $[H_3N\text{-}(CH_2)_n\text{-}NH_3]PbX_4$ (n=4-8, X=Cl, Br, I).

CONCLUSION

In this work, 15 hybrid compounds based on lead halides and a homologous series of limiting diamines of the type $[H_3N\text{-}(CH_2)_n\text{-}NH_3]PbX_4$ (n=4-8, X=Cl, Br, I) were studied and the influence of the structure of the organic cation and the type of anion on their structural, electronic and optical properties.

The structures of new hybrid crystals based on lead chloride and pentanediamine-1.5, heptanediamine-1,7, octanediamine-1,8, as well as lead bromide and pentanediamine-1,5, heptanediamine-1,7 were synthesized and described for the first time; the patterns of luminescent properties of hybrid crystals of the type $[H_3N\text{-}(CH_2)_n\text{-}NH_3]PbX_4$ were described and analyzed for the first time (n=4-8, X=Cl, Br, I) depending on their anionic and cationic composition; phase transitions in hybrid crystals of the form $[H_3N\text{-}(CH_2)_n\text{-}NH_3]PbX_4$ (n=4-8, X=Cl, Br, I) are described for the first time.

For the first time, the manifestation of the parity effect of the carbon skeleton of an organic cation represented by saturated alkanediamines in hybrid crystals was discovered and analyzed. For chloride and bromide crystals, the parity effect is manifested as follows: an even carbon skeleton in the structure of an organic cation promotes the formation of two-dimensional hybrid crystals with layers of inorganic octahedra arranged on top of each other without displacement, whereas an odd carbon skeleton promotes the formation of two-dimensional hybrid crystals with layers of inorganic octahedra offset relative to each other by half the width of the octahedron. For iodide crystals, the parity effect manifests itself differently: an even carbon skeleton in the structure of an organic cation contributes to the formation of two-dimensional hybrid crystals, whereas an odd carbon skeleton contributes to the formation of one-dimensional and zero-dimensional structures.

It has been established that two-dimensional hybrid crystals (all chloride and bromide, as well as iodide crystals with an even carbon skeleton in the structure of an

organic cation) are straight-band semiconductors, transitions from the valence band to the conduction band in which mainly occur at the point Γ of the Brillouin zone. It is shown that iodide hybrid crystals with an odd carbon skeleton in the structure of an organic cation forming a one-dimensional structure are non-direct band semiconductors.

It is shown that during the formation of hybrid crystals, two competing processes of disordering the inorganic sublattice are observed: the internal one, characterized by distortion of the shape of each octahedron or displacement of lead atoms in octahedra from a central position, and the external one, characterized by maintaining the relative perfection of the octahedra themselves, but manifested in the inclination of the octahedra relative to each other when they are combined into a network.

It is shown that all two-dimensional hybrid crystals exhibit luminescent properties. Typical luminescence of hybrid crystals based on lead halides and saturated alkanediamines may include narrow-band luminescence of self-trapped excitons, broadband luminescence of defect-trapped excitons, or both of these bands, which is determined by the cationic and anionic composition of the hybrid crystal: chloride hybrid crystals are characterized by the presence of only broadband luminescence of defect-trapped excitons; for bromide and iodide crystals, the presence of both luminescence bands is characteristic; for bromide crystals, the ratio of luminescence intensities of self-trapped excitons and defect-trapped excitons depends on the size of the organic cation and decreases as it grows. The energy of self-localization of free excitons for bromide hybrid crystals ranges from 20 to 31 meV, for iodide crystals – from 11 to 31 meV.

The results of the presented dissertation research are given in 3 publications in peer-reviewed journals, the list of which is given below:

1. **Balanov M.I.** Crystal structure and electronic properties of low-dimensional hexamethylenediaminium lead halide perovskites / M.I. Balanov, O.A. Brylev, V.V. Korochencev, R. Kevorkyants, A.V. Emeline, N.I. Selivanov, Y.V. Chizhov, A.V. Syuy, D.S. Shtarev // Dalton Transactions. – 2023. - Vol. 52. - p.

6388-6397.

DOI: 10.1039/D3DT00438D

2. Shtarev D.S. The effect of halogen on the structural, optoelectronic, and luminescent properties of hybrid (1,5-Pentanediamine)PbX_4 (X=Cl, Br, I) perovskites / D.S. Shtarev, **M.I. Balanov**, A.Ju. Mayor, A.V. Gerasimenko, R. Kevorkyants, D. Zharovov, K.M. Bulanin, D. Pankin, A.V. Rudakova, D.A. Chaplygina, N.I. Selivanov, A.V. Emeline // Journal of Materials Chemistry C. – 2024. – Vol. 12. – p. 262-275.

DOI: 10.1039/D3TC02767H

3. **Balanov M.I.** Influence of the even-odd effect on the crystal structure, band structure and optical properties of hybrid crystals of the $[H_3N\text{-}(CH_2)_n\text{-}NH_3]PbX_4$ (n=4-8, X=Cl, Br, I) type / M.I. Balanov, A.V. Emeline, D.S. Shtarev // Dalton Transactions. – 2024. - Accepted Manuscript.

DOI: 10.1039/D4DT01811G

ACKNOWLEDGMENTS

The author expresses gratitude to his supervisor D.S. Shtarev for guiding and stimulating research. The author is also grateful to Emelin A.V., Major A.Yu., Korochentsev V.V., Kevorkyants R.E. for their help in carrying out research and fruitful discussion of the results.

REFERENCES

1. M.A. Green, E.D. Dunlop. J. Hohl-Ebinger, M. Yoshita, N. Kopidakis, A.W.Y. Ho-Baillie, Solar cell efficiency tables (Version 55) // Prog. Photovolt. Res. Appl., 2020, Vol.28, p.3-15, DOI: 10.1002/pip.3228
2. H. Cho, S. Jeong, M. Park, Y. Kim, C. Wolf, C. Lee, J.H. Heo, A. Sadhanala, N. Myoung, S. Yoo, S. Im, R. Friend, T. Lee, Overcoming the electroluminescence efficiency limitations of perovskite light-emitting diodes // Science, 2015, Vol.350, p.222−1225, DOI: 10.1126/ science.aad1818
3. N. Wang, L. Cheng, R. Ge, S. Zhang, Y. Miao, W. Zou, C. Yi, Y. Sun, Y. Cao, R. Yang, Y. Wei, Q. Guo, Y. Ke, M. Yu, Y. Jin, Y. Liu, Q. Ding, D. Di, L. Yang, G. Xing, H. Tian, C. Jin, F. Gao, R.H. Friend, J. Wang, W. Huang, Perovskite light-emitting diodes based on solution-processed self-organized multiple quantum wells // Nat. Photonics, 2016, Vol.10, p.699−704, DOI: 10.1038/nphoton.2016.185
4. Z. Xiao, R.A. Kerner, L. Zhao, N.L. Tran, K.M. Lee, T.-W. Koh, G.D. Scholes, B.P. Rand, Efficient perovskite light-emitting diodes featuring nanometre-sized crystallites // Nat. Photonics, 2017, Vol.11, p.108−115, DOI: 10.1038/nphoton.2016.269
5. H. Zhu, Y. Fu, F. Meng, X. Wu, Z. Gong, Q. Ding, M.V. Gustafsson, M.T. Trinh, S. Jin, X.Y. Zhu, Lead halide perovskite nanowire lasers with low lasing thresholds and high quality factors // Nat. Mater., 2015, Vol.14, p.636-642, DOI: 10.1038/nmat4271
6. C. Bao, Z. Chen, Y. Fang, H. Wei, Y. Deng, X. Xiao, L. Li, J. Huang, Low-noise and large-linear-dynamic-range photodetectors based on hybrid-perovskite thin-single-crystals // Adv. Mater., 2017, Vol.29, 1703209, DOI: 10.1002/adma.201703209

7. H. Wei, Y. Fang, P. Mulligan, W. Chuirazzi, H.-H. Fang, C. Wang, B.R. Ecker, Y. Gao, M.A. Loi, L. Cao, J. Huang, Sensitive X-ray detectors made of methylammonium lead tribromide perovskite single crystals // Nat. Photonics, 2016, Vol.10, p.333−339, DOI: 10.1038/nphoton. 2016.41
8. A.E. Maughan, J.A. Kurzman, and J.R. Neilson, Hybrid inorganic–organic materials with an optoelectronically active aromatic cation: $(C_7H_7)_2SnI_6$ and $C_7H_7PbI_3$ // Inorg. Chem., 2015, Vol.54, p.370−378, DOI: 10.1021/ic5025795
9. R. Kevorkyants, A.V. Emeline, D.W. Bahnemann, Hybrid lead triiodide perovskites with unsaturated heterocyclic cations containing N, O, and S atoms: Ab initio study // J. Solid State Chem., 2020, Vol.282, p.121082, DOI: 10.1016/j.jssc.2019.121082
10. R. Kevorkyants, D.W. Bahnemann, A.V. Emeline, Modulating optoelectronic properties of organo-metal halide perovskites with unsaturated heterocyclic cations via ring substitution // J. Phys. Chem. Solids, 2019, Vol.135, Article 109078, DOI: 10.1016/j.jpcs.2019.109078
11. N.I. Selivanov, A.A. Murashkina, R. Kevorkyants, A.V. Emeline, D.W. Bahnemann, Pyridinium lead tribromide and pyridinium lead triiodide: quasi-one-dimensional perovskites with an optically active aromatic π-system // Dalton Trans., 2018, Vol.47, p.16313–16319, DOI: 10.1039/C8DT03041C
12. N.I. Selivanov, Yu.A. Rozhkova, R. Kevorkyants, A.V. Emeline, and D.W. Bahnemann, The effect of organic cations on the electronic, optical and luminescence properties of 1D piperidinium, pyridinium, and 3-hydroxypyridinium lead trihalides // Dalton Trans., 2020, Vol.49, p.4390-4403, DOI: 10.1039/C9DT04543K
13. David B. Mitzi, Templating and structural engineering in organic–inorganic perovskites // J. Chem. Soc., Dalton Trans., 2001, Issue 1, p.1-12, DOI: 10.1039/B007070J
14. Tony Dantes de Morais, Frederic Chaput, Khalid Lahlil, Jean-Pierre Boilot, Hybrid Organic–Inorganic Light-Emitting Diodes // Adv. Mater., 1999, Vol.11,

Issue 2, p. 107-112, DOI: 10.1002/(SICI)1521-4095(199902)11:2%3C107::AID-ADMA107%3E3.0.CO;2-J

15. K. Seham, A. Abdel, K.-O. Gudrun, I. Andrei, R. N. Mozhchil. Effect of organic chain length on structure, electronic composition, lattice potential energy, and optical properties of 2D hybrid perovskites $[(NH_3)(CH_2)_n(NH_3)]CuCl_4$, n = 2–9 // Appl. Phys. A, 2017, Vol.123, article number 531, DOI: 10.1007/s00339-017-1150-8
16. I. Spanopoulos, W. Ke, C.C. Stoumpos, E.C. Schueller, O.Y. Kontsevoi, R. Seshadri, M.G. Kanatzidis. Unraveling the Chemical Nature of the 3D "Hollow" Hybrid Halide Perovskites // Journal of American Chemical Society, 2018, Vol.140, p.5728−5742, DOI: 10.1021/jacs.8b01034
17. T. Zhang, M.I. Dar, G. Li, F. Xu, N. Guo, M. Grätzel, Y. Zhao. Bication lead iodide 2D perovskite component to stabilize inorganic a-$CsPbI_3$ perovskite phase for high-efficiency solar cells // Science Advances, 2017, Vol.3, Article ID e1700841, DOI: 10.1126/sciadv.1700841
18. M Taddei, J.A. Smith, B.M. Gallant, S. Zhou, R.J.E. Westbrook, Y. Shi, J. Wang, J.N. Drysdale, D.P. McCarthy, S. Barlow, S.R. Marder, H.J. Snaith, D.S. Ginger. Ethylenediamine Addition Improves Performance and Suppresses Phase Instabilities in Mixed-Halide Perovskites // ACS Energy Letters, 2022, Vol. 7, Issue 12, p.4265–4273, DOI: 10.1021/acsenergylett.2c01998
19. A. Glushkova, A. Arakcheeva, P. Pattison, M. Kollár, P. Andričević, B. Náfrádi, L. Forróa, E. Horváth. Influence of the organic cation disorder on photoconductivity in ethylenediammonium lead iodide, $NH_3CH_2CH_2NH_3PbI_4$ // Cryst.Eng.Comm., 2018, Vol. 20, p.3543–3549, DOI: 10.1039/C8CE00259B
20. M. Fazayeli, M. Khatamian, G. Cruciani, Anomalous inclusion of chloride ions in ethylenediammonium lead iodide turns 1D non-perovskite into a 2D perovskite structure // Cryst.Eng.Comm., 2020, Vol.22, p.8063-8071, DOI: 10.1039/D0CE00184H

21. L. Jiang, Y. Qiu, H. Zhang, L. Lin, F. Yan, D. Chen. Moisture-stable Perovskite Material with 1,3-Propanediaminium Cation for Solar Cell Application // Chemistry Letters, 2017, Vol.46, p.1227-1229, DOI: 10.1246/cl.170494
22. A.B. Corradi, A.M. Ferrari, G.C. Pellacani, A. Saccani, F. Sandrolini, P. Sgarabotto, Structural and Electrical Characterization of Polymeric Haloplumbate(II) Systems // Inorganic Chemistry, 1999, Vol.38, p.716-721, DOI: 10.1021/ic980893k
23. X. Zhang, L. Xu, M. Chen, Y. Kang, J. Lei, Q. Wu, C. Sun, Z. Lin, P. Wang, Z. Yang. Structural, electronic and optoelectronic properties of asymmetric organic ligands in Dion-Jacobson phase perovskites // Solid State Communications, 2022, Vol.350, Article 114761, DOI: 10.1016/j.ssc.2022.114761
24. C. Ma, D. Shen, T.-W. Ng, M.-F. Lo, C.-S. Lee, 2D Perovskites with Short Interlayer Distance for High-Performance Solar Cell Application // Advanced Materials, 2018, Vol.30, Article 1800710, DOI: 10.1002/adma.201800710
25. L. Mao, Y. Wu, C.C. Stoumpos, M.R. Wasielewski, M.G. Kanatzidis. White-Light Emission and Structural Distortion in New Corrugated Two-Dimensional Lead Bromide Perovskites // Journal of American Chemical Society, 2017, Vol.139, p.5210-5215, DOI: 10.1021/jacs.7b01312
26. Stoumpos C. C., Kanatzidis M. G., The Renaissance of Halide Perovskites and Their Evolution as Emerging Semiconductors // Acc.Chem.Res., 2015, Vol.48, p.2791-2802, DOI: 10.1021/acs.accounts.5b00229
27. Stoumpos C.C., Kanatzidis M.G., Halide Perovskites: Poor Man's High-Performance Semiconductors // Adv.Mater., 2016, Vol.28, p.5778-5793, DOI: 10.1002/adma.201600265
28. S. Wang, Y. Yao, J. Kong, S. Zhao, Z. Sun, Z. Wu, L. Li, J. Luo. Highly efficient white-light emission in a polar two-dimensional hybrid perovskite // Chem Commun., 2018, Vol.54, p.4053-4056, DOI: 10.1039/c8cc01663a
29. T. Niu, H. Ren, B. Wu, Y. Xia, X. Xie, Y. Yang, X. Gao, Y. Chen, W. Huang. Reduced-Dimensional Perovskite Enabled by Organic Diamine for Efficient

Photovoltaics // Journal of Physical Chemistry Letters, 2019, Vol.10, p.2349-2356, DOI: 10.1021/acs.jpclett.9b00750

30. Seham K. Abdel-Aal, A. Ouasri, Crystal structures, hhirshfeld surfaces analysis, Infrared and Raman studies of organic-inorganic hybrid perovskite salts $NH_3(CH_2)_nNH_3MnCl_4$ (n = 5, 6) // Journal of Solid State Chemistry, 2022, Vol.314, Article 123401, DOI: 10.1016/j.jssc.2022.123401
31. H. Fu, Ch. Jiang, Ch. Luo, H. Lin, H. Peng. A Quasi-Two-Dimensional Copper Based Organic-Inorganic Hybrid Perovskite with Reversible Thermochromism and Ferromagnetism // Europ.J.Inorg.Chem., 2021, Vol.2021, Issue 47, p.4984-4989, DOI: 10.1002/ejic.202100811
32. Z. Kang, H. Xiong, B. Wu, L. Jiang, B. Fan, A. Yang, B. Sa, J. Li, L. Lin, Y. Qiu. Stable copper-based 2D perovskite $(NH_3C_3H_6NH_3)CuBr_4$ thin film processed from green solvent for thermoelectric application // EcoMat., 2022, Vol.4, Article e12163, DOI: 10.1002/eom2.12163
33. M. Thierry. L es composites moléculaires bidimensionnels $[NH_3\text{-}(CH_2)_n\text{-}NH_3]MX_4$. Incidence structurale du paramètre n et de la nature du métal (M = Cd, Mn, Pb, Cu, Pd). THESE. L'UNIVERSITE BORDEAUX I. 1996, p. 252.
34. G.A. Mousdis, G.C. Papavassiliou, C.P. Raptopoulou, A. Terzis, Preparation and characterization of $[H_3N(CH_2)_6NH_3]PbI_4$ and similar compounds with a layered perovskite structure // J.Mater.Chem., 2000, Vol.10, p.515-518, DOI: 10.1039/A906161D
35. A. Lemmerer, D.G. Billing, Lead halide inorganic-organic hybrids incorporating diammonium cations // Cryst.Eng.Comm., 2012, Vol.14, p.1954-1966, DOI: 10.1039/C2CE06498G
36. D.G. Billing, A. Lemmerer. Bis(pentane-1,5-diammonium) decaiodotriplumbate(II) // Acta Crystallographica Section C, 2004, Vol.C60, p.m224-m226, DOI: 10.1107/S0108270104007553
37. C. Courseille, N.B. Chanh, Th. Maris, A. Daoud, Y. Abid, M. Laguer, Crystal Structure and Phase Transition in the Perovskite-Type Layer Molecular

Composite $NH_3(CH_2)_4NH_3PbCl_4$ // Physica Status Solidi A, 1994, Vol.143, p.203-214, DOI: 10.1002/pssa.2211430202

38. M. Safdari, P.H. Svensson, M.T. Hoang, I. Oh, L. Kloo, J.M. Gardner, Layered 2D alkyldiammonium lead iodideperovskites: synthesis, characterization, and use in solar cells // Journal of Materials Chemistry A, 2016, Vol.4, p.15638–15646, DOI: 10.1039/c6ta05055g
39. X. Li, J. Hoffman, W. Ke, M. Chen, H. Tsai, W. Nie, A.D. Mohite, M. Kepenekian, C. Katan, J. Even, M.R. Wasielewski, C.C. Stoumpos, M.G. Kanatzidis, Two-Dimensional Halide Perovskites Incorporating Straight Chain Symmetric Diammonium Ions, $(NH_3C_mH_{2m}NH_3)(CH_3NH_3)_{n-1}Pb_nI_{3n+1}$ (m=4−9; n=1−4) // Journal of Americal Chemical Society, 2018, Vol.140, p.12226-12238, DOI: 10.1021/jacs.8b07712
40. L. Li, X. Shang, S. Wang, N. Dong, C. Ji, X. Chen, S. Zhao, J. Wang, Z. Sun, M. Hong, J. Luo, Bilayered Hybrid Perovskite Ferroelectric with Giant Two-Photon Absorption // Journal of Americal Chemical Society, 2018, Vol.140, p.6806-6809, DOI: 10.1021/jacs.8b04014
41. X. Li, X. Lian, J. Pang, B. Luo, Y. Xiao, M.-D. Li, X.-C. Huang, J.Z. Zhang, Defect-Related Broadband Emission in Two Dimensional Lead Bromide Perovskite Microsheets // Journal of Physical Chemistry Letters, 2020, Vol.11, Issue 19, p.8157-8163, DOI: 10.1021/acs.jpclett.0c02355
42. M.D. Smith, A.Jaffe, E.R. Dohner, A.M. Lindenberg, H.I. Karunadasa, Structural Origins of Broadband Emission from Layered Pb–Br Hybrid Perovskites // Chemical Science, 2017, Vol.8, p.4497-4504, DOI: 10.1039/C7SC01590A
43. Bruker AXS TOPAS V4: General profile and structure analysis software for powder diffraction data. – User's Manual. Bruker AXS, Karlsruhe, Germany. 2008.
44. J.F. Moulder, W.F. Stickle, P.E. Sobol, K.D. Bomben, Handbook of X-Ray Photoelectron Spectroscopy, Perkin-Elmer Corp., Eden Prairie (MN), 1992, p.261.
45. http://www.crystallography.net/cod/

46. A. Baeyer, Ueber Regelmässigkeiten im Schmelzpunkt homologer Verbindungen // Berichte der deutschen chemischen Gesellschaft, 1877, Vol.10, Issue 2, p.1286-1288, DOI: 10.1002/cber.18770100204
47. K. Yang, Z. Cai, A. Jaiswal, M. Tyagi, J.S. Moore, Y. Zhang. Dynamic Odd–Even Effect in Liquid n-Alkanes near Their Melting Points // Angew. Chem. Int. Ed., 2016, Vol.55, p.14090-14095, DOI: 10.1002/anie.201607316
48. D. Cortecchia, J. Yin, A. Petrozza, C. Soci, White light emission in low-dimensional perovskites // J. Mater. Chem. C, 2019, Vol.7, p.4956-4969, DOI: 10.1039/c9tc01036j
49. C.C. Stoumpos, M.G. Kanatzidis, The renaissance of halide perovskites and their evolution as emerging semiconductors // Acc. Chem. Res., 2015, Vol.48, p.2791−2802, DOI: 10.1021/ acs.accounts.5b00229
50. D. Shtarev, M. Balanov et.al. The effect of halogen on the structural, optoelectronic, and luminescent properties of hybrid (1,5-Pentanediamine)PbX_4 (X=Cl, Br, I) perovskites // Journal of Materials Chemistry C, 2024, Vol.12, p.262-275, DOI: 10.1039/D3TC02767H
51. Xue H, Chen Z, Tao S, Brocks G. Defects in Halide Perovskites: Does It Help to Switch from 3D to 2D? // ACS Energy Lett., 2024, Vol.9, p.2343-2350, DOI: 10.1021/acsenergylett.4c00702
52. Ch.H. Don, H. Shiel, Th.D.C. Hobson, Ch.N. Savory, J.E.N. Swallow, M.J. Smiles, L.A.H. Jones, Th.J. Featherstone, P.K. Thakur, T-L. Lee, K. Durose, J.D. Major, V.R. Dhanak, D.O. Scanlon and T.D. Veal, Sb $5s^2$ lone pairs and band alignment of Sb_2Se_3: a photoemission and density functional theory study // J.Mater.Chem. C, 2020, Vol.8, p.12615-12622, DOI: 10.1039/D0TC03470C
53. V. Srikant, D. R. Clarke, On the optical band gap of zinc oxide // Journal of Applied Physics, 1998, Vol.83, p.5447, DOI: 10.1063/1.367375
54. M.V. Maevskaya, A.V. Rudakova, A.V. Koroleva, A.S. Sakhatskii, A.V. Emeline, D.W. Bahnemann, Effect of the Type of Heterostructures on Photostimulated Alteration of the Surface Hydrophilicity: $TiO_2/BiVO_4$ vs.

$ZnO/BiVO_4$ Planar Heterostructured Coatings // Catalysts, 2021, Vol.11, p.1424, DOI: 10.3390/catal11121424

55. D.O. Scanlon, C.W. Dunnill, J. Buckeridge, S.A. Shevlin, A.J. Logsdail, S.M. Woodley, A.A. Sokol, Band alignment of rutile and anatase TiO_2 // Nature Materials, 2013, Vol.12, p.798-801, DOI: 10.1038/nmat3697
56. M.I. Balanov, O.A. Brylev, V.V. Korochencev, R. Kevorkyants, A.V. Emeline, N.I. Selivanov, Y.V. Chizhov, A.V. Syuy, D.S. Shtarev. Crystal structure and electronic properties of low-dimensional hexamethylenediaminium lead halide perovskites // Dalton Transactions, 2023, Vol. 52, p.6388-6397, DOI: 10.1039/D3DT00438D
57. N.F. Mott and R.W. Gurney, Electronic Processes in Ionic Crystals, 2nd ed. / Oxford University Press, London, 1948, p.275
58. F. Seitz, Speculations on the Properties of the Silver Halide Crystals // Rev. Modern Phys., 1951, Vol.23, p.328-352, DOI: 10.1103/RevModPhys.23.328
59. M.I. Balanov, A.V. Emeline, D.S. Shtarev Influence of the even-odd effect on the crystal structure, band structure and optical properties of hybrid crystals of the $[H_3N\text{-}(CH_2)_n\text{-}NH_3]PbX_4$ (n=4-8, X=Cl, Br, I) type // Dalton Transactions, 2024, Vol. 53, p.13764-13781, DOI: 10.1039/D4DT01811G
60. A. R. Zanatta Revisiting the optical bandgap of semiconductors and the proposal of a unified methodology to its determination // Scientific Reports, 2019, Vol.9, Article 11225, DOI: 10.1038/s41598-019-47670-y